UC San Diego
UC San Diego Electronic Theses and Dissertations

Title
Conformational Dynamics of Membrane Proteins

Permalink
https://escholarship.org/uc/item/7q0337mm

Author
Kopcho, Noah Jordan

Publication Date
2020

Peer reviewed|Thesis/dissertation

UNIVERSITY OF CALIFORNIA SAN DIEGO

Conformational Dynamics of Membrane Proteins

A dissertation submitted in partial satisfaction of the

requirements for the degree Doctor of Philosophy

in

Chemistry

by

Noah Jordan Kopcho

Committee in charge:

Professor Geoffrey Chang, Chair
Professor Elizabeth Komives, Co-chair
Professor Itay Budin
Professor Kevin Corbett
Professor Dionicio Siegel
Professor Akif Tezcan

2020

The dissertation of Noah Jordan Kopcho is approved,

and it is acceptable in quality and form for publication on

microfilm and electronically:

_____

_____

_____

_____

_____
Co-chair

_____
Chair

University of California San Diego

2020

TABLE OF CONTENTS

LIST OF ABBREVIATIONS

β-DDM	n-dodecyl-β-D-maltopyranoside
2D	Two-dimensional
3D	Three-dimensional
Å	Angstrom
Ab	Antibody
ABC	ATP binding cassette
ADP	Adenosine diphosphate
ATP	Adenosine triphosphate
ANO	Anoctamin
At	Arabidopsis thaliana
BLI	Biolayer interferometry
BSA	Bovine serum albumin
Cryo	Cryogenic
CTF	Contrast transfer function
Da	Dalton
DO	Dissolved oxygen
GSFSC	Gold standard fourier shell correlation
EC	Extracellular
EM	Electron microscopy
ESI+	Electrospray ionization positive ion detection
FACS	Fluorescence activated cell sorting
FRET	Fluorescence resonance energy transfer

GEF	guanine-nucleotide exchange factor
GEM	guanine-nucleotide exchange modulator
GDI	guanine-nucleotide exchange dissociation inhibitor
GDP	Guanosine triphosphate
GFP	Green fluorescent protein
GPCR	G-protein couple receptor
GST	Glutathione-S-transferase
GTP	Guanosine triphosphate
HDX	Hydrogen-deuterium exchange
IPTG	isopropyl β-d-1-thiogalactopyranoside
ICH	Intracellular helix
K_D	Binding affinity
k_a	Association rate constant
k_d	Dissociation rate constant
kV	Kilovolt
LB	Lysogeny broth
LC	Liquid chromatography
NMR	Nuclear Magnetic Resonance
MD	Molecular dynamics
MH+	Monoisotopic mass
MS	Mass spectrometry
MS^E	Mobility ESI+
Nb	Nanobody

NBD	Nucleotide binding domain
Nh	Nectria hematococca
NSL	Nucleotide stabilizing linker
Os	Oryza sativa
PBS	Phosphate buffered saline
PDB	Protein Data Bank
PI	Propidium iodide
P-gp	P-glycoprotein
RRM	RNA-recognition motif
Q-TOF	Quadrapole Time-of- Flight
ScFv	Single chain variable fragment
SEC	Size exclusion chromatography
TC	Transporter classification
TCEP	tris-carboxyethylphosphine
TEV	Tobacco etch virus
TMH	Transmembrane helix
V_H	Heavy chain variable domain
V_{HH}	Antigen-binding variable domain
V_L	Light chain variable domain
VPP	Volta phase plate
WT	Wild-type

LIST OF FIGURES

LIST OF TABLES

ACKNOWLEDGEMENTS

VITA

2005 – 2008   US Army

2014   Bachelors of Science, Chemistry, University of Texas, Austin

2017   Masters of Science, Biochemistry, University of California San Diego

2020   Doctor of Philosophy, Biochemistry, University of California San Diego

PUBLICATIONS

Kopcho, N., Chang, G., Komives, E.A. (2019) "Dynamics of ABC transporter P-glycoprotein in three conformational states" *Sci. Rep.* **9**: 10592.

Maity, K., Heumann, J.M., McGrath, A.P., **Kopcho, N.J.**, Hsu, P.K., Lee, C.W., Mapes, J.H., Garza, D., Krishnan, S., Morgan, G.P., Hendargo, K.J., Klose, T., Rees, S.D., Mendrano-Soto, A., Saier, M.H., Pineros, M., Komives, E.A, Schroeder, J.I., Chang, G., Stowell, M.H.B. (2019) "Cryo-EM structure of OSCA1.2 from Oryza sativa elucidates the mechanical basis of potential membrane hyperosmolality gating" *PNAS*. **116**:14309-14318.

Kalogriopoulos, N., Rees, S.D., Ngo, T., **Kopcho, N.J.**, Ilatovskiy, A.V., Sun, N., Komives, E.A, Chang, G., Ghosh, P., Kufareva, I. (2019) "Structural basis for GPCR-independent activation of heterotrimeric Gi proteins" *PNAS*. **116**: 16394-16403.

FIELDS OF STUDY

Major Field: Biochemistry

Studies in Biochemistry and Biophysics

Professors Geoffrey Chang & Elizabeth A. Komives

HONORS AND AWARDS

2007   US Army Combat Action Badge

2007   US Army Commendation Medal

2017   Frontiers of Innovation Scholars Program

2017   UCSD Stem Cell Program Innovative Projects in Alzheimer's Award

2017 – 2018   Molecular Biophysics Training Grant

ABSTRACT OF THE DISSERTATION

Conformational Dynamics of Membrane Proteins

by

Noah Jordan Kopcho

Doctor of Philosophy in Chemistry

University of California San Diego, 2020

Professor Geoffrey Chang, Chair

Professor Elizabeth A. Komives, Co-chair

Membrane proteins reside along the barrier between intracellular and extracellular milieu. They regulate transport and transduce signal necessary to maintain life. Critical to these functions are dynamic motions capable of transmitting molecules or information. The method of HDX-MS is uniquely suited to studying such conformational dynamics, as the timescales of measurement refer to the broad motions associated with domain movement and catalysis. This work employs HDX-MS to study the dynamics of three unique membrane associated proteins. Kinetic analysis and the method of HDX-MS are extended to characterize *in vitro* generated monoclonal camelid antibody fragments.

Chapter I provides a general introduction to protein dynamics and HDX-MS. An overview of timescales of molecular motions is presented, followed by a summary of timescales measurable by common biophysical techniques. The advantages of HDX-MS used to study biologically relevant dynamic events are discussed, and an introduction to HDX-MS theory and methodology is presented.

Chapter II provides a cryo-EM structure of the Oryza sativa ion channel OSCA1.2. This transporter responds to hyperosmolality in the environment to regulate ion flux. Computational and experimental dynamics are studied and a mechanism of osmolarity sensing is presented.

Chapter III utilizes structural insight along with HDX-MS measurements of dynamics to probe non-canonical activation of the peripheral membrane G protein subunit Gαi. This work provides insight into how binding of guanosine exchange modulators stimulates GDP dissociation in Gαi subunits.

Chapter IV contains an extensive study of the ABC transporter P-gp dynamics in three distinct conformations. Very high sequence coverage permits a global overview of P-gp dynamics. Comparisons between the inward-facing, pre-hydrolytic and outward-facing conformations indicate structural rearrangements undergone by the transporter, and show that the pre-hydrolytic ATP-bound state occupies an occluded conformation.

In Chapter V, a rapid *in vitro* discovery platform is utilized to generate camelid antibody fragments specific for the P-gp molecule. This method generated a nM affinity anti-pgp Nb in a matter of days without the need for animal immunization. HDX-MS is employed to provide a map of the binding interaction, and BLI is utilized to measure binding kinetics.

Chapter I:

Introduction

A. Conformational Dynamics

A common phrase taught to students of biology is that structure follows function. An easy to grasp illustration of this expression is the physiology of a human hand. The function of the hand is the manipulation of objects, and the structure of the hand follows this function with fingers that enable digital manipulation. Similar logic applies on the scale of biological macromolecules. The folded structure of a protein determines the location and orientation of side chain and backbone atoms critical for carrying out biological processes. Just as the hand must undergo motion in order to grasp objects, biologically active proteins often require dynamic processes to carry out their unique functions.

Structures determined by conventional biophysical techniques are generally presented as static images. In reality, proteins are highly dynamic machines in constant motion. These conformational dynamics occur over an enormous range of time scales. At the most elemental level, chemical bonds vibrate and rotate on the order of femtoseconds (1). Amino acid side chains undergo motions at a thousandth of this pace on the picosecond timescale (2). While the peptide bonds that comprise a protein backbone rotate even more slowly on the order of nanoseconds (3).

Dynamics on the scale of folded proteins occur still more slowly over the broad range of microseconds to seconds (Fig. 1). This was shown to be the case for adenylate kinase, where the nucleotide binding domain was found to alternate in and out of catalytically competent states on the microsecond to millisecond regime (4). Similar timescales of domain movement were noted in P-glycoprotein where conformational processes associated with nucleotide hydrolysis were found to occur over milliseconds (5). Other proteins exhibit slower dynamics, such as heat shock protein 90 which undergoes conformational transitions over several minutes (6).
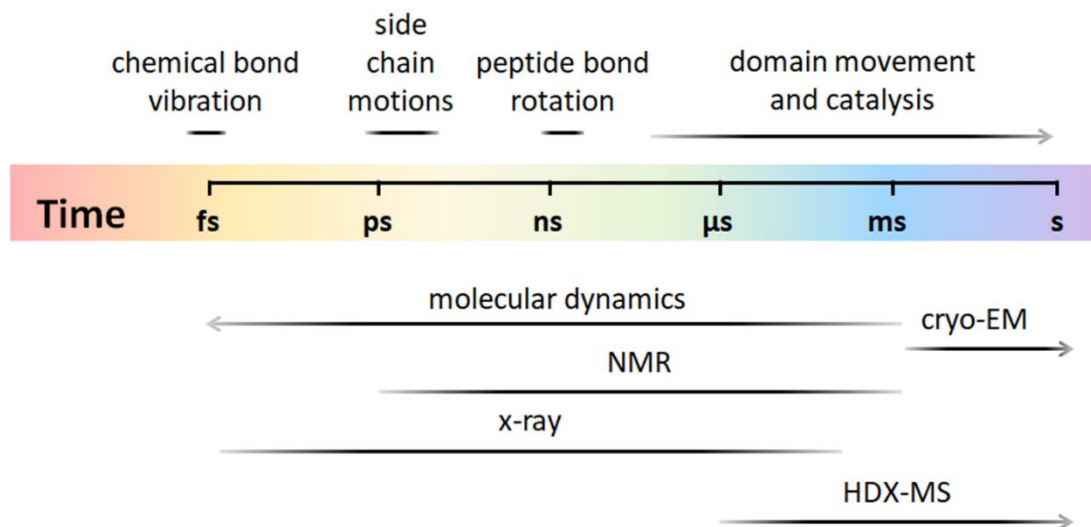
Figure 1.1. Timescales of dynamics. Timescales of fundamental dynamic processes and regimes accessible by common biophysical techniques are summarized. HDX-MS is uniquely suited to study dynamic motions associated with enzymatic functionality.

Nearly any measurable parameter that varies along with conformation may be taken as a measure of dynamics. A common approach is to study changes in spectroscopic properties as a molecule undergoes conformational changes (7). Fluorescent energy transfer is also commonly used to track conformational transitions due to its strict dependence on distance between fluorophores. This may involve native tryptophan residues (8) or strategically placed labels (9). Paramagnetic resonance spectroscopy can also provide a similar measure of intramolecular distance (10). All spectroscopic methods are advantageous in that experiments may be carried out over very long time-courses, enabling observation of slow dynamic processes. However, the data obtained reflect global conformational changes or the distance between two points and do not provide a rigorous depiction of molecular motions.

Time-resolved imaging techniques, on the other hand, can provide a direct view of conformational dynamics. There are many available modalities with individual benefits and drawbacks. X-ray imaging can be used to study the dynamics of proteins either in solution or in

the crystal phase (11). The lower limit of dynamic timescales accessible is limited by how quickly data can be acquired, and new x-ray sources are capable of delivering femtosecond pulses (12). Observations cannot extend beyond the millisecond range however, as prolonged exposure to x-ray radiation leads to protein degradation (13).

Cryogenic electron microscopy (cryo-EM) is an alternative capable of delivering structural data on par with x-ray imaging, though its usage is limited to macromolecules larger than ~50 kDa. Proteins studied using this method are flash frozen and deposited on grids before imaging, and the timescale of images is limited by the time necessary for sample handling. Currently the fastest fluidics handlers can achieve this in about 10 milliseconds, and any dynamic events occurring faster than this are inaccessible by cryo-EM (14). While there is no upper limit to dynamic timescales observable via cryo-EM, the microscopes are very costly and instrument time is a valuable commodity. Further, structural data is obtained through image averaging of well-populated conformations among the molecular ensemble. Sparsely occupied conformations will not be observed with cryo-EM.

Nuclear magnetic resonance (NMR) is another imaging technique that can provide structural data of proteins in solution (15). Dynamic events may be probed down to the picosecond range using NMR, but thetimescales of observed events generally do not extent beyond milliseconds as measurements are limited by the delay time between radio frequency pulses. (16). Data interpretation is further complicated with increasing molecular weight, resulting in a practical upper limit of ~75 kDa.

An *in silico* alternative to time-resolved imaging is the use of molecular dynamics (MD) simulations. Computational modeling has been widely used in the study of protein dynamics (17). Such simulations may be carried out using various degrees of granularity to limit the strain

on processing power and increase the duration of the simulation (18). Due to computational limitations, MD simulations do not surpass milliseconds in duration and therefore cannot depict slow dynamic processes associated with domain movement and catalysis.

B. Hydrogen-deuterium exchange mass spectrometry

Hydrogen-deuterium exchange mass spectrometry (HDX-MS) is an alternative technique for studying protein dynamics that is free from many limitations of other methods. Measurements are carried out in the native aqueous environment, and proteins of any size may be characterized. HDX-MS exploits the phenomenon of backbone amide hydrogen-deuterium exchange to probe changes in protein dynamics and solvent accessibility (19). When exposed to buffered D_2O, amide protons will exchange with deuterons in the same manner as they would react with protons from H_2O. Exchange occurs more rapidly for labile protons that are exposed to solvent than for those that are confined by structural elements (20). As a protein naturally undergoes conformational motions, additional protons will be rendered competent to exchange with deuterium. Thus, by measuring deuterium incorporation as a function of time, a picture of regional dynamics emerges.

The exchange rate of individual amide protons is affected by many factors in the chemical environment. Salt, pH, temperature and neighboring side chains all contribute to the rate at which backbone protons interchange with the deuterium nuclei. While these factors can cause individual exchange rate constants to vary over several orders of magnitude, experimentally determined exchange rates of amides in unstructured peptides have been found to occur on the order of milliseconds to seconds (21). Deuterium incorporation also requires an amide proton to be solvent exposed. In proteins, the dynamic processes which gradually expose amides to exchange involve large scale domain movement and generally occur over

5

microseconds to minutes. Smaller conformational fluctuations occur more quickly than

deuterium exchange and do not interfere with measurements (17). HDX-MS therefore provides

an excellent readout of large-scale conformational dynamics.

In a typical HDX-MS experiment, the protein of interest is first added to deuterated

buffer and allowed to exchange for some desired amount of time (Fig. 2). Timepoints are often

chosen such that uptake profiles will distinguish between fast exchanging amide protons in

unstructured regions, moderately exchanging protons in folded labile regions and slowly

exchanging protons in well-folded or occluded regions. Before measurement of deuterium
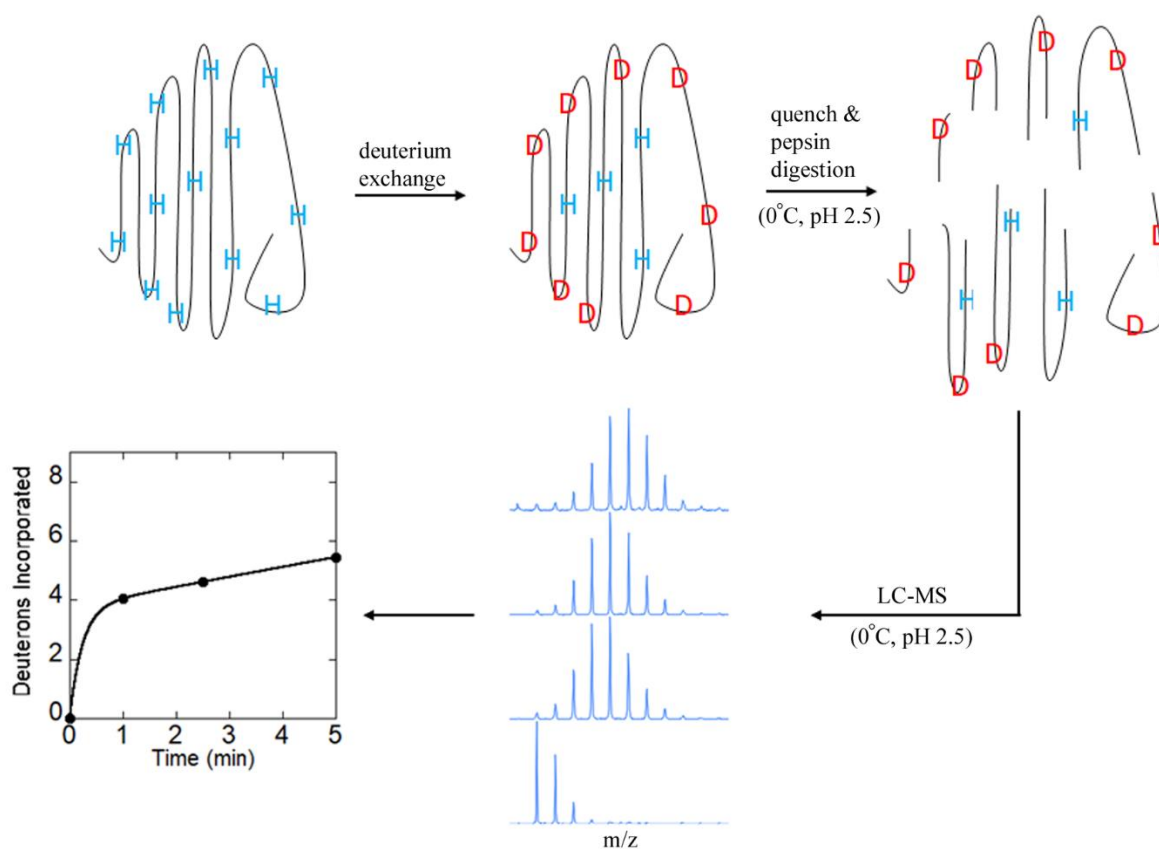
Figure 1.2. HDX-MS workflow. A typical HDX-MS experiment begins with
deuterium labeling in D_2O buffer. The exchange reaction is then quenched at low
temperature and pH 2.5 and deuterium incorporation is quantified via LC-MS.

6

uptake, samples are quenched at 0˚C and pH 2.5, and denaturant is added to aid protease

digestion.

Deuterium exchange is highly dependent on temperature and pH. Quenching by bringing

the sample to 0˚C and pH 2.5 takes advantage of this dependence to inhibit the exchange reaction

. Deuterium exchange can occur by either an acid-catalyzed or base-catalyzed mechanism. The

observed exchange rate for an individual amide proton is the sum of the rates of these two

mechanisms (Fig. 3). Because the base-catalyzed pathway occurs several orders of magnitude

more quickly than the acid-catalyzed mechanism, the slowest observed rate occurs at the low pH

range between 2.5 and 3 (21). Conveniently, side chain protons back-exchange readily within

this pH range and do not interfere with measurements (22). Lowering the pH to the exchange

rate minimum of pH 2.5 (Fig. 3) in the quench step minimizes the exchange of the deuteriums

back to hydrogen during chromatographic separation and analysis.

After quenching, the sample is digested by an acid-stable protease and the resulting

peptides are separated using a liquid chromatography (LC) system maintained at low
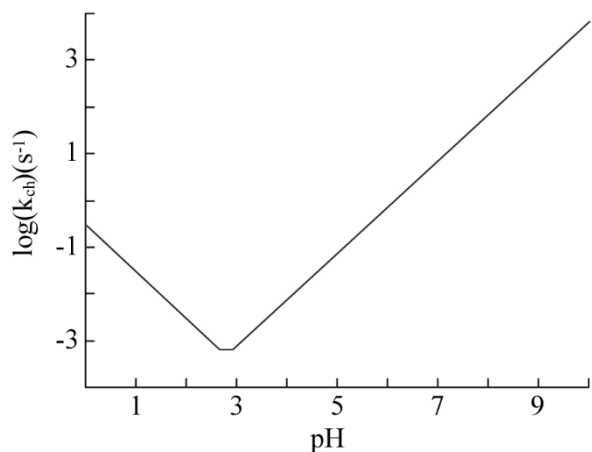
Figure 1.3. Exchange rate pH dependence. Example of observed
deuterium exchange rate as a function of pH for a single amide proton.

temperature. Deuterium incorporation is then quantified via MS analysis. This provides a very rich dataset. The LC retention time of each peptide is unique and may be used to validate peptide assignments during data analysis, and the shape of mass spectra also give an indication of protein dynamics.

To be rendered competent for exchange, an amide proton must first be exposed to solvent and free of intramolecular hydrogen bonds. Conformational dynamics are required for this to occur, with the exception of highly disordered regions. Just as localized regions may unfold and expose protons to solvent, refolding processes also occur. This relationship may be described by the following chemical equation:

$$F_H \underset{k_{-1}}{\overset{k_1}{\rightleftharpoons}} U_H \xrightarrow[\text{D}_2\text{O}]{k_2} U_D \underset{k_1}{\overset{k_{-1}}{\rightleftharpoons}} F_D$$
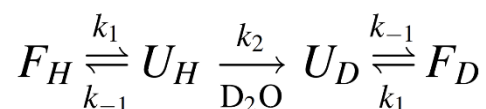
Where F and U refer to folded and unfolded states for a region bearing a specific amide proton, and subscripts H and D denote the protonated and deuterated states, respectively.

The fragment ions observed following an HDX-MS experiment usually appear as a single peak increasing in mass over time as more deuterium nuclei are incorporated (Fig. 4A). This happens when the refolding process which occludes an amide proton from solvent occurs much more quickly than the exchange reaction. In mathematical terms, this situation arises when $k_{-1} \gg k_2$ and is referred to as EX2 kinetic exchange.

A less common situation arises in the opposite scenario when $k_{-1} \ll k_2$ and is known as EX1 kinetic exchange. When the folding and unfolding processes which expose amides to solvent are much slower than the exchange reaction, distinct populations of deuterated and protonated amides may be observed if there are enough amides undergoing the exchange to produce a separate population of deuterated amides (23). These species are indicated by bimodal

peaks the mass spectra (Fig. 4B). EX1 kinetics are associated with cooperative folding events. Thus, in addition to generating information related to solvent accessibility, HDX-MS also provides a readout of conformational dynamics.

In summary, HDX-MS provides highly sensitive local probes of internal protein dynamics that are rich in information regarding the internal motions of a protein as they occur in solution. While it is difficult to interpret the amide exchange in terms of specific dynamic events, comparisons of different states of a protein such as with and without a bound ligand can reveal interpretable differences such as ligand binding sites (24) and long range allostery (25).
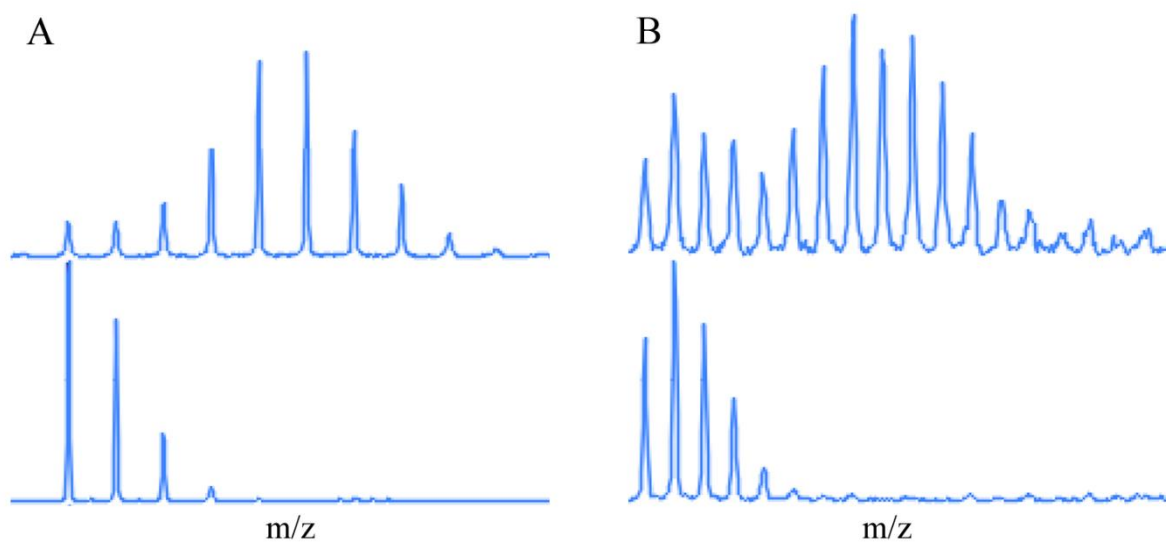
Figure 1.4. EX2 and EX1 kinetics. Peptides displaying EX2 **(A)** and EX1 **(B)** kinetics are shown. Deuterium exchange was measured after 0 min (bottom) and 5 min (top).

C. References

1.   Dantus M, Bowman RM, & Zewail AH (1990) Femtosecond laser observations of molecular vibration and rotation. *Nature* 343:737-739.

2.   Nakamura H, Mashimo S, & Wada A (1981) Observation of the side-chain motion of polypeptides in solution by measurement of picosecond dialectric relaxation. *Macromolecules* 14:1698-1711.

3.   Thompson PA, Munoz V, Jas GS, Henry ER, Eaton WA, & Hofrichter J (2000) The helix-coil kinetics of a heptapeptide. *J. Phys. Chem. B* 104:378-389.

4.   Henzler-Wildman KA, Lei M, Thai V, Kerns SJ, Karplus M, & Kern D (2007) A hierarchy of timescales in protein dynamics is linked to enzyme catalysis. *Nature* 450:913-916.

5.   Zoghbi ME, Cooper RS, & Altenberg GA (2016) The lipid bilayer modulates the structure and function of an ATP-binding cassette exporter. *J. Biol. Chem.* 291:4453-4461.

6.   Ye W, Gotz M, Celiksoy S, Tuting L, Ratzke C, Prasad J, Ricken J, Wegner SV, Guzman RA, Hugel T, & Sonnichsen C (2018) Conformational dynamics of a single protein monitored for 24 h at video rate. *Nano Lett.* 18:6633-6637.

7.   Lu HP (2005) Probing single-molecule protein conformational dynamics. *Acc. Chem. Res.* 38:557-565.

8.   Yang H, Luo G, Karnchanaphanurach P, Louie TM, Rech I, Cova S, Xun L, & Xie XS (2003) Protein conformational dynamics probed by single-molecule electron transfer. *Science* 302:262-266.

9.   Wang S, Vafabakhsh R, Borschel WF, Ha T, & Nichols CG (2016) Structural dynamics of potassium-channel gating revealed by single-molecule FRET. *23* (31-37).

10.   Verhalen B, Dastvan R, Thangapandian S, Peskova T, Koteiche HA, Nakamoto RK, Tajkhorshid E, & Mchaourab HS (2017) Energy transduction and alternating access of the mammalian ABC transporter P-glycoprotein. *Nature* 543:738-742.

11.   Westenhoff S, Nazarenko E, Malmberg E, Davidsson J, Katona G, & Neutze R (2009) Time-resolved studies of protein reaction dynamics: a smorgasboard of X-ray approaches. *Acta Cryst. A* 66:207-219.

12.   Srajer V & Schmidt M (2017) Watching proteins function with time-resolved x-ray crystallography. *J. Phys. D Appl. Phys* 50:373001-373025.

13. Carugo O & Karugo KD (2005) When x-rays modify the protein structure: radiation damage at work. *Trends Biochem. Sci.* 30:213-219.

14. Frank J (2017) Time-resolved cryo-electron microscopy: recent progress. *J. Struct. Biol.* 200:303-306.

15. Grutsch S, Bruschweiler S, & Tollinger M (2016) NMR methods to study dynamic allostery. *PLoS Comput. Biol.* 12:e1004620.

16. Toyama Y, Osawa M, Yokogawa M, & Shimada I (2016) NMR method for characterizing microsecond-to-millisecond chemical exchanges utilizing differential multiple-quantum relaxation in high molecular weight proteins. *J. Am. Chem. Soc.* 138:2302-2311.

17. Munoz V (2007) Conformational dynamics and ensembles in protein folding. *Annu. Rev. Biophys. Biomol. Struct.* 36:395-412.

18. Shi Q, Izvekov S, & Voth GA (2006) Mixed atomistic and coarse-grained molecular dynamics: simulation of a membrane-bound ion channel. *J. Phys. Chem. B* 110:15045-15048.

19. Wales TE & Engen JR (2006) Hydrogen exchange mass spectrometry for the study of proteins. *Mass Spec. Rev.* 25:158-170.

20. Cao J, Burke JE, & Dennis EA (2013) Using Hydrogen/Deuterium Exchange Mass Spectrometry to Define the Specific Interactions of the Phospholipase A2 Superfamily with Lipid Substrates, Inhibitors, and Membranes. *J. Biol. chem.* 288:1806-1813.

21. Bai Y, Milne JS, Mayne L, & Englander WS (1993) Primary Structure Effects on Peptide Group Hydrogen Exchange. *Proteins: Struc., Funct., Genet.* 17:75-86.

22. Zhang Z & Smith DL (1993) Determination of amide hydrogen exchange by mass spectrometry: A new tool for protein structure elucidation. *Protein Sci.* 2:522-531.

23. Hoofnagle A, Resing KA, & Ahn NG (2003) Protein analysis by hydrogen exchange mass spectrometry. *Annu. Rev. Biophys. Biomol. Struct.* 32:1-25.

24. Mandell JG, Falick AM, & Komives EA (1998) Identification of protein–protein interfaces by decreased amide proton solvent accessibility. *PNAS* 95:14705-14710.

25. Ramsey KM, Dembinski HE, Chen W, Ricci CG, & Komives EA (2017) DNA and IκBα both induce long-range conformational changes in NFκB. *J. Mol. Biol.* 429:999-1008.

Chapter II:

Structure and Dynamics of Hyperosmolality Gated Ion Channel OSCA1.2

A. Introduction

Hyperosmolarity and osmotic stress are among the first physiological responses to changes in salinity and drought. Hyperosmolality triggers increases in cytosolic free Ca^{2+} concentration and thereby initiates an osmotic stress-induced signal transduction cascade in plants (1-4). Salinity and drought stress trigger diverse protective mechanisms in plants enabling enhanced drought tolerance and reduction of water loss in leaves. Ion channels have long been hypothesized as sensors of osmotic stress. A candidate membrane protein named OSCA was isolated in a genetic screen for mutants that impair the rapid osmotic stress-induced Ca^{2+} elevation in plants (1). Arabidopsis thaliana OSCA1 (AtOSCA1) encodes a multispanning membrane protein that was reported to function in osmotic/mechanical stress-induced activation of ion currents. However, the underlying mechanisms and whether AtOSCA1 homologs include an ion-conducting Ca^{2+}-permeable pore require further analysis. AtOSCA1 is a member of a larger gene family in Arabidopsis with 15 members (5), and with many homologs encoded in other plants and fungal genomes. Furthermore, evolutionary analyses have revealed that OSCA is distantly related to the anoctamin (ANO) superfamily, which includes the TMEM16 family of calcium dependent ion channels and lipid scramblases (6).

B. Materials and Methods

1. Expression and purification of OsOSCA1.2

We cloned OsOSCA1.2 (GenBank KJ920372.1) and made (tobacco etch virus) TEV protease-cleavable green fluorescent protein (GFP) fusions into the pPICZc vector, and then tested expression in *P. pastoris*. Expression vectors were linearized using PmeI and electroporated into competent *P. pastoris* KM71H cells (Life Technology). The resulting transformants were cultured and induced in small scale to screen for target expression based on

the intrinsic GFP fluorescence of cells and also from an anti-His Western blot of whole-cell lysate. OsOSCA1.2 was found to show both high levels of expression and desirable properties during purification (described below), and was therefore chosen for further characterization. Yeast clones selected for their high expression of OsOSCA1.2 were grown in minimal glycerol (4%) media, supplemented with 0.4% phosphoric acid and 0.024% trace metals at 28 °C in a New Brunswick BioFlo 415 system (Eppendorf). The pH of the media was titrated to pH 5 before inoculation and adjusted during the vegetative growth phase using 50% ammonium hydroxide. The dissolved oxygen (DO) was maintained at 10% minimally through cascaded agitation until a DO spike occurred. The fermentation culture was then induced at pH 5 by slow methanol addition for 16–18 h.

Cells were harvested and resuspended in cold lysis buffer [20 mM Tris·HCl (pH 8.0), 100 mM NaCl, 15% glycerol, 23.4 mM leupeptin, 7 mM E-64, 4 mM chymostatin, 14.5 mM pepstatin A, 1 mM phenylmethylsulfonyl fluoride, 25 mM benzamidine], and they were lysed by a single passage through a cell disruptor (TS-Series; Constant Systems, Inc.) at 40,000 psi. Cellular debris was removed by centrifugation (12,500 × g, 20 min, 4 °C), and the supernatant was continued onto a 38,400 × g spin for 4 h to fractionate the plasma membrane. The membrane fraction was resuspended in lysis buffer and frozen at −80 °C.

Membranes were solubilized with 1% n-dodecyl-β-D-maltopyranoside (β-DDM) and 0.1% sodium cholate for ~90 min at 4 °C. Insoluble material was removed by centrifugation (38,400 × g, 60 min, 4 °C), and 15 mM imidazole was added to the supernatant before batch binding to Ni- NTA agarose resin (Qiagen). The bounded resin was sequentially applied to a gravity column housing and washed with buffer A [20 mM Hepes (pH 8.0), 150 mM NaCl, 0.03% β-DDM, 0.003% cholesteryl hemisuccinate], and an imidazole gradient was applied.

15

Bound target protein was eluted with buffer A containing 300 mM imidazole, concentrated to ~8 mL, desalted (HiPrep 26/10; GE Healthcare), and subjected to TEV protease digestion for 12 h at 4 °C. The TEV-digested sample was reapplied to Ni-agarose (Qiagen) to rebind the TEV protease and the C-terminal His-GFP tag. The collected OsOSCA1.2 was then concentrated to ~1 mL and ultraspun at 95,000 rpm (TLA120.1 rotor) for 15 min at 4 °C. The sample was then applied to a Superdex 200 increase size-exclusion column (GE Healthcare) preequilibrated with 20 mM Hepes (pH 8.0), 150 mM NaCl, 0.06% n-undecyl-β-D-maltopyranoside, 0.2 mM Tris(2-carboxyethyl)phosphine, and 0.01% cholesteryl hemisuccinate, and run at 4 °C. Peak fractions off the SEC column were checked using sodium dodecyl sulfate/polyacrylamide gel electrophoresis and directly snap-frozen at a concentration of ~3 mg/mL.

2. Electron microscopy (EM) data collection

Quantifoil 1.2/1.3 Au (Quantifoil Micro Tools GmbH) or CFlat 1.2/1.3 300 (Protochips) mesh grids were glow-discharged for 30 s at 30 mA (Emitech). Four microliters of OSCA1.2 at a concentration of 1.8 mg/mL was applied to the grids, blotted for 2.5 s at a relative humidity of 100%, and plunge-frozen in liquid ethane using an FEI Vitrobot Mark 2 system (FEI Company). Two image sets were collected. The first dataset was collected using defocus phase contrast on an FEI Tecnai F30 microscope (FEI Company) operating at 300 kV with a K2 Summit camera (Gatan, Inc.) at a nominal magnification of 31,000× in superresolution mode with a pixel size of 0.636 Å using SerialEM software (Mastronarde Group). A total of 40 frames at 200 ms per frame were recorded for each image at a camera dose rate of 8 electrons per pixel per second. A total of 342,910 particles covering a defocus range from −0.8 to −2.8 μM were used to determine an initial 6.0-Å resolution map that allowed a polyalanine model to be built (Table 2.1). A higher resolution dataset was collected using an FEI Titan Krios equipped with a Volta phase plate

16

(VPP), GatanEnergy filter, and K2 Summit camera (Gatan, Inc.). Data were collected at a

nominal magnification of 105,000× in superresolution mode, and a total of 64,096 individual

particle images at a fixed target defocus of −0.5 μm were used to determine the structure at a

resolution of 4.9 Å (Table 2.1).

Table 2.1. Cryo-EM data collection, 3D reconstruction and model building

Data Collection and Processing		
Microscope	FEI Tecnai F30	FEI Titan Krios
Voltage (kV)	300	300
Camera (mode)	Gatan K2 Summit (40 frame super-res movies)	Gatan K2 Summit (40 frame super-res movies)
Target Defocus (μm)	-0.8 to -2.8	-0.5 Volta Phase Plate
Pixel size (Å)	0.6355	0.6920
Imposed symmetry	C2	C2
Electron dose (e-/ Å ^{2})	45.5	40.8
Initial particle images	499,157	169,655
Final particle images	342,910	64,096
Map resolution (Å) FSC 0.143	6.0 Å	4.9 Å
Max local resolution (Å)	4.8 Å	4.5 Å
Model Building and Refinement		
Map sharpening B factor (Å^2)	-800	-400
Protein residues (expected)	1388 (1424)*	1388 (1424)
R.M.S. Z score		
Bond Lengths (# Z>2)		0.30 (2)
Bond Angles (# Z>2)		0.44 (6)
Validation		
MolProbity score		1.98
Clashscore		7.99
EMRinger score		0.82
Poor rotamers (%)		0.00
Ramachandran plot		
Favored (%)		90.1
Outliers (%)		0.0

3. EM data processing

The Tecnai F30 dataset, consisting of a total of 9,691 micrographs in 3 groups, was selected for initial processing after motion correction using MotionCor2 and contrast transfer function (CTF) estimation with Gctf. Non–dose-weighted micrographs were used for CTF estimation, and dose-weighted micrographs were used for all other processing. Approximately 1,000 manually picked particles from each group were used to generate 2× binned templates (2.542-Å pixel size), which were used for autopicking in RELION. Autopicked particles were manually screened, and 499,167 particles were extracted for further processing in cryoSPARC. 2-dimensional (2D) classification and selection yielded 342,910 particles that were then used for initial model construction and auto-refinement. Auto-refinement and masking with C2 symmetry yielded a map with a resolution of 6.0 Å by gold standard Fourier shell correlation (GSFSC) corrected for the effects of masking. Local resolution estimation in cryoSPARC indicated that the core regions have resolutions ranging from 4.5 to 6.0 Å.

The Titan Krios dataset consisted of a total of 2,408 micrographs that were motion-corrected using MotionCor2, and CTFs were estimated using Gctf. Results were imported into RELION 2.1. A total of 1,126 corrected micrographs were selected for further processing after screening for excessive motion and poor or poorly estimated CTFs. A total of 1,134 particles were manually picked and classified in 2 dimensions, and the selected templates were used to auto-pick 372,278 particles. Further screening resulted in the selection of 650 micrographs containing 169,655 particles for additional processing. The 2× binned (2.76-Å pixel size) particles were extracted and processed through 2 rounds of 2D classification and selection, resulting in 64,096 remaining particles. 3-dimensional (3D) auto-refinement with C2 symmetry using these particles and an initial model from the previous defocus contrast refinement yielded a

model with a resolution of 7.4 Å. Re-extraction with unbinned pixels and subsequent refinement led to no improvement in resolution at this stage. 3D classification into 10 classes and subset selection yielded 5 subsets (best single class, best 2 classes, best 5 classes, and all classes) that were used for another round of re-extraction and auto-refinement. The best resolution resulted from using all 64,096 particles and was unchanged at 7.4 Å. Masking and post-processing resulted in an estimated resolution of 6 Å. At this point, the 64,096 extracted particles were transferred to cryoSPARC, and subsequent processing was performed in cryoSPARC. 3D auto-refinement with C2 symmetry using all 64,096 particles and an initial model constructed using a subset of 16,438 selected particles resulted in a GSFSC estimated resolution of 4.9 Å. The auto-refined, unsharpened map was further sharpened with a B-factors ranging from −350 to −600 out to a cutoff of 3.5 Å for modeling, and a map with a B-factor of −530 was used for subsequent model building and refinement.

4. Model building and refinement

An initial polyalanine model was built using the 6.0-Å resolution map with multiple rounds of real-space refinement in Phenix/Coot (7, 8). To determine the absolute hand at this resolution, the initial and inverted models were utilized for molecular replacement using an X-ray diffraction dataset that extended to 9 Å in resolution. Only one model provided a solution to the molecular replacement search. Subsequent use of this initial model and the observation of the helical hand in the 4.9-Å resolution map further confirmed the correctness of the assigned hand. The full atomic model was built into the higher resolution map using multiple rounds of building and real-space refinement in Coot and Phenix. The density maps within the transmembrane (TM) region were of sufficient quality to readily identify large aromatic side chains and helped to confirm the correct sequence registration. Comparison with the recently determined structures of

AtOSCA1.2 (9-11) further confirmed the correctness of our model despite the lower calculated overall resolution of our map.

5. Image processing

Motion-corrected projections with a pixel size of 1.271 Å (F30) and 1.384 Å (Titan Krios), with and without dose weighting, were constructed using MotionCor2 (12) with 2× binning and grouping. The CTF estimation was performed using Gctf (13), followed by manual selection to remove micrographs with poor or incorrectly fit CTF, poor astigmatism, and contamination. Manual and semiautomated particle picking was done using RELION 2.1 (14), followed by sorting and another round of manual overreading to remove low-quality micrographs. Subsequent refinements were carried out in RELION or cryoSPARC (15). Local resolution estimation was performed using cryoSPARC or ResMap (16).

6. Hydrogen-deuterium exchange mass spectrometry of OsOSCA1.2

Hydrogen-deuterium exchange mass spectrometry (HDX-MS) measurements were made using a Synapt G2Si system (Waters Corporation). Deuterium exchange reactions were carried out by a Leap HDX PAL autosampler (Leap Technologies). The deuterated buffer was prepared by lyophilizing 10 mL of 20 mM Hepes (pH 8.0) and 150 mM NaCl. The lyophilized buffer was resuspended in 10 mL of 99.96% D_2O immediately before use, to which was added powdered n-undecyl-β-D-maltopyranoside to a final concentration of 0.06% and cholesterol hemisuccinate to a final concentration of 0.01%. Each deuterium exchange time point (0 min, 1 min, 2.5 min, and 5 min) was measured in triplicate. For each measurement, 4 μL of protein at a concentration of 5 μM was mixed with 36 μL of D_2O buffer at 25 °C. Deuterium exchange was quenched by combining 35 μL of the deuterated sample with 65 μL of 0.1% formic acid and 3 M guanidinium-HCl for 1 min at 1 °C. The quenched sample was then injected in a 50-μL sample

20

loop and digested by an in-line pepsin column (Pierce, Inc.) at 15 °C. The resulting peptides were captured on a BEH C4 Vanguard precolumn at a flow rate of 400 μL·s−1, separated by analytical chromatography (Acquity UPLC BEH C4, 1.7 μM, 1.0 × 50 mm; Waters Corporation) using 7–85% acetonitrile in 0.1% formic acid over 7.5 min, and analyzed in a Waters Synapt G2Si quadrupole time-of-flight mass spectrometer following electrospray injection.

Data were collected in Mobility [Electrospray ionization positive ion detection (ESI+) mode, mass acquisition range of 200–2,000 mass-to-charge ratio (m/z), scan time of 0.4 s]. Continuous lock mass correction was performed using the infusion of leu-enkephalin (m/z = 56.277) every 30 s (mass accuracy of 1 ppm for calibration standard). For peptide identification, data were collected in MS^E (mobility ESI+) mode. Peptide masses were identified following triplicate analysis of 10 μM OsOSCA1.2, and the data were analyzed using PLGS 2.5 (Waters Corporation). Peptide masses were identified using a minimal number of 250 ion counts for low-energy peptides and 50 ion counts for their fragment ions. The following parameters were used to filter peptide sequence matches: minimum products per amino acid of 0.2, a minimum score of 7, maximum monoisotopic mass (MH+) error of 5 ppm, and a retention time relative standard deviation of 5%, and the peptides had to be present in 2 of the 3 peptide identification runs collected. After identification in PLGS, peptides were analyzed in DynamX 3.0 (Waters Corporation). Deuterium uptake for each peptide was calculated by comparing the centroids of the mass envelopes of the deuterated samples with the undeuterated controls. To account for back-exchange and systematic autosampler sample handling differences, the uptake values measured at the 1-min time point were divided by 0.79. The longer 2.5-min and 5-min deuteration time point deuteration values were divided by 0.75. Data were plotted as a number of deuterons incorporated vs. time. The y-axis limit for each plot reflects the total number of amides

21

within the peptide that can possibly exchange. Each plot includes the peptide MH+ value, sequence, and sequential residue numbering.

C. Results

As we were interested in determining whether and how osmolality caused OSCA proteins to respond to osmotic stress in crop plants, we screened 5 such putative OSCA channels from rice, overexpressing them as TEV protease cleavable GFP fusions in Pichia pastoris. The Oryza sativa gene (annotated as OsOSCA1.2, GenBank KJ920372.1) was found to have both high levels of protein expression and desirable properties during purification, and was therefore chosen for further characterization.

1. Structure of OsOSCA1.2

We determined a molecular structure of OsOSCA1.2 by single-particle cryogenic-electron microscopy (cryo-EM) to an overall resolution of 4.9 Å and local resolution in the membrane of 4.5 Å, revealing a dimer of C2 symmetry-related subunits. The overall dimensions of the protein are 140 Å $\times$ 55 Å $\times$ 85 Å. Each protomer is composed of 11 TM spanning segments, associated extracellular and intracellular loops, and an intracellular soluble domain (Fig. 2.1A). All 11 TM helices and the soluble domain are well resolved in our cryo-EM maps, and large side chains provided suitable markers for ensuring proper sequence registration during atomic model building. The final atomic model comprises 1,388 of the expected 1,424 residues with good geometry and an EMRinger (17) score of 0. 89.
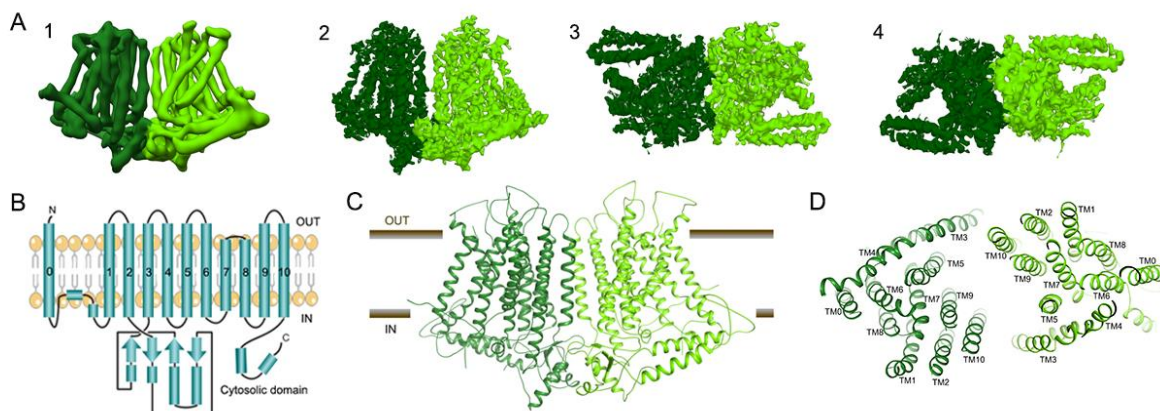
Figure 2.1. Cryo-EM structure of the OsOSCA1.2 ion channel. (A) From left to right, (1) Parallel to membrane plane view of unsharpened cryoEM density map used for initial chain tracing, (2-4) sharpened 4.9 Å map used for model building and refinement: (2) membrane plane view, (3) extracellular view, and (4) intracellular view. **(B)** Protein topology of OsOSCA1.2. View of OsOSCA1.2 model from **(C)** the plane of the cell membrane and **(D)** from the extracellular side.

According to the Transporter Classification (TC) Database (18), OsOSCA1.2 belongs to what is annotated as the calcium-permeable stress-gated cation channel family (TC accession no. 1.A.17.5) within the ANO superfamily (TC accession no. 1.A.17). This classification indicates that OsOSCA1.2 is distantly related to members of the ANO family (TC accession no. 1.A.17.1) for which high-resolution 3-dimensional structures are available (19, 20). Following a recently published bioinformatics approach (6), we had further predicted that OsOSCA1.2 had 11 TMs and the eighth hydrophobicity peak is composed of 2 TMs (Fig. 2.1B) based on hydropathy analysis and comparison of regions with the fungal homolog Nectria hematococca TMEM16 (NhTMEM16) (19). For convenience, we have kept the numbering convention of TMs consistent with NhTMEM16, and we thus refer to OsOSCA1.2's additional N-terminal TM as TM0 (Fig. 2.1C-D). Despite a relatively low degree of sequence similarity, we later confirmed that OsOSCA1.2 shares significant structural homology to the TMEM proteins with respect to 10 of

23

the 11 TM regions, corresponding to TM1–TM10 in the mouse TMEM16A (mTMEM16A) structures (20).

TM0 threads from the extracellular N-terminal end of the protein through the membrane, linking to TM1 via an ~50-residue strand that is likely conformationally flexible. This portion of the protein is the only region not fully resolved in our density maps (Fig. 2.1B–D). A short helix on the cytoplasmic side then precedes TM1, and the C-terminal end of TM2 leads into the soluble cytosolic region of ~170 residues. The remaining helices represent the ANO domain, encapsulating the predicted TM transport pathway. TM3 and TM4 are located on the outer edge of the TM region and are tilted with respect to the membrane. TM7 and TM8 are shorter in length and are the only TMs that do not span the entire length of the membrane, with the connecting loop (residues 578–583) being embedded in the membrane and consisting of hydrophobic residues.

The soluble domain is located on the intracellular side of the protein joining TM2 and TM3, and makes important structural contacts with the C terminus (Fig. 2.1B–D). A core globular domain comprises a 4-stranded β-sheet buttressed by 2 short helices that interestingly forms a canonical RNA recognition motif (RRM) fold (21). Unlike true RNA binding RRM proteins, OsOSCA1.2 includes a fusion of a distinct 70-residue appendage between β-strands 2 and 3. These long extended helical arms protrude out from the RRM domain and are located proximal to and in the plane of what would be the inner-leaflet side of the plasma membrane.

2. OsOSCA1.2 experimental dynamics

To further understand and probe local conformational dynamics of OsOSCA1.2, we used HDX-MS. HDX-MS measurements using detergent-solubilized OsOSCA1.2 protein resulted in the identification of 32 peptides, which constitute 34.5% coverage of the molecule, including the helical arms that were predicted to dynamically couple to the presumed gating helix TM6 and most likely to be responsible for sensing lateral tension in the membrane (Fig. 2.2A).
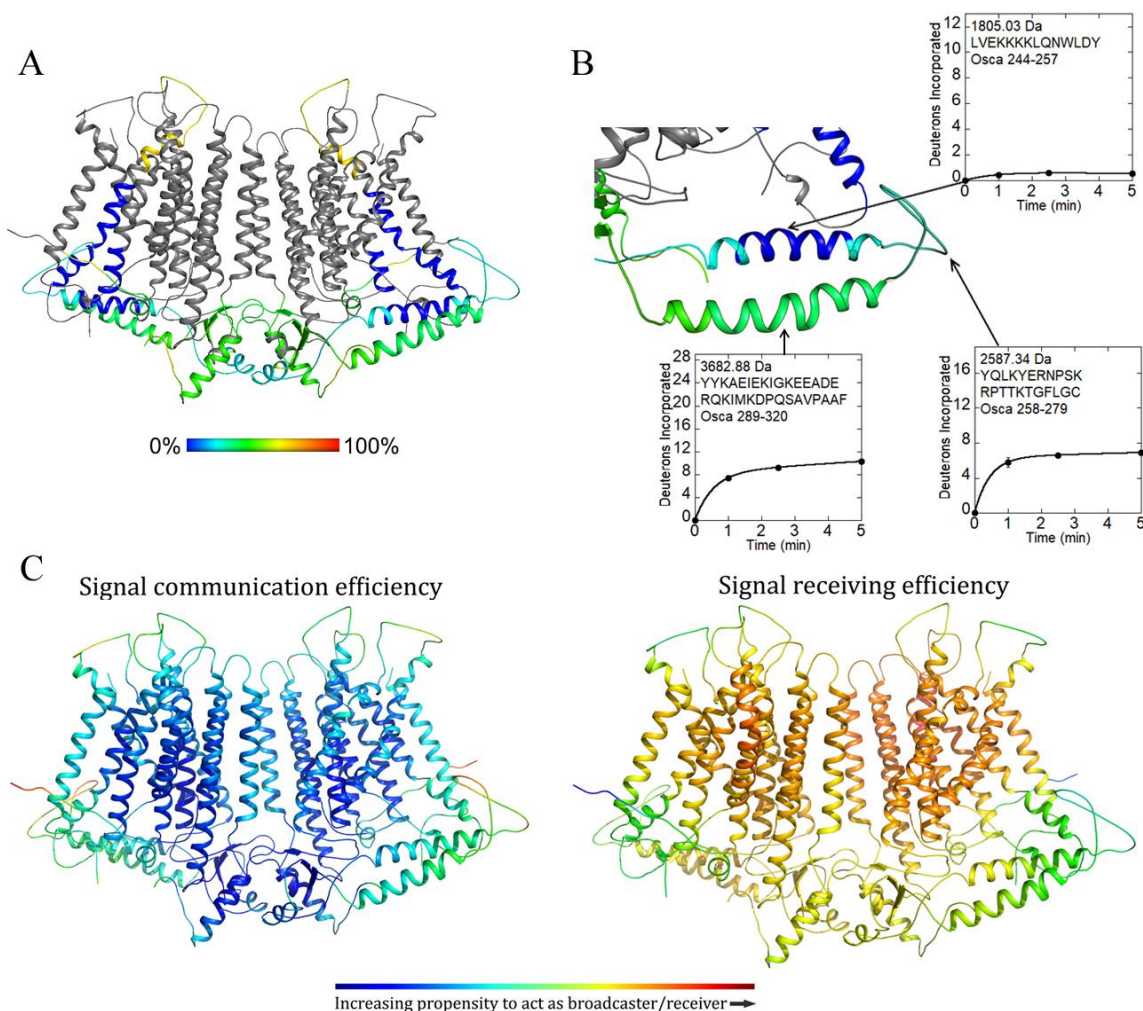
Figure 2.2. Computational and experimental dynamics of OsOSCA1.2. (**A**) Relative uptake after 5 minutes of exchange. Regions colored gray yielded no detectable peptide fragments. (**B**) Close-up view of the extended and gating helix. Uptake plots for selected peptides are shown. (**C**) Results of the Dynomics suite. Panels show a color-coded map showing signal communication (left) and receiving (right) efficiency. Regions colored red are more active while those blue inactive with regards to molecular dynamics prediction.

The helix closest to the inner leaflet side of the membrane was covered by 2 peptides (corresponding to residues 244–257 and 245–257). Deuterium incorporation profiles revealed that this region was tightly protected from the exchange, indicative of rigid dynamics or association with a nearby surface (Fig. 2.2B). The following segment was also covered by 2 peptides (residues 258–279 and 258–286), which correspond to the C-terminal end of the protected helix and a nearby loop in our structure. This region was ~25% saturated with deuterium nuclei at the earliest measured time point of 1 min, indicating rapid exchange associated with conformational flexibility. The remainder of this segment increased deuterium content by ~5% over 5 min, suggesting conformational motions that gradually increased exposure to solvent. The helix farther from the membrane was covered by 3 peptides (residues 287–320, 289–320, and 305–320) and similarly displayed rapidly exchanging amides and ongoing deuterium exchange.

Mass spectra from peptides corresponding to the unstructured loop and helix farther from the membrane all displayed bimodal deuterium uptake, which was more prominent among peptides corresponding to the loop (Fig. 2.3). The ongoing dynamics stand in sharp contrast to the rigidity of the helix (residues 241–266) closer to the membrane. Despite being spatially and sequentially near each other, these 2 intracellular helices have very different dynamic properties.

3. OsOSCA1.2 computational dynamics

The DynOmics suite allows prediction and identification of candidate functional sites, signal transduction, and potentially allosteric communication mechanisms, leveraging rapidly growing structural proteomics data (22). The suite integrates 2 widely used elastic network models while taking account of the molecular environment like the lipid bilayer providing

26

collective dynamics of structural resolved systems. We used DynOmics to do molecular dynamic

simulations on our OsOSCA1.2 dimer model after embedding in the membrane, looking for

regions that could potentially serve as functionally important sensors, broadcasters, and receivers

(Fig. 2.2C). Our results revealed that the extended intracellular helical arms could communicate

conformational perturbations, having the propensity to act as a broadcaster/receiver, extending to

the central core sheet structure of the soluble domain and, more interestingly, TM6, which is

proposed to be the transport pathway gating helix in related structures (9-11, 19, 20).
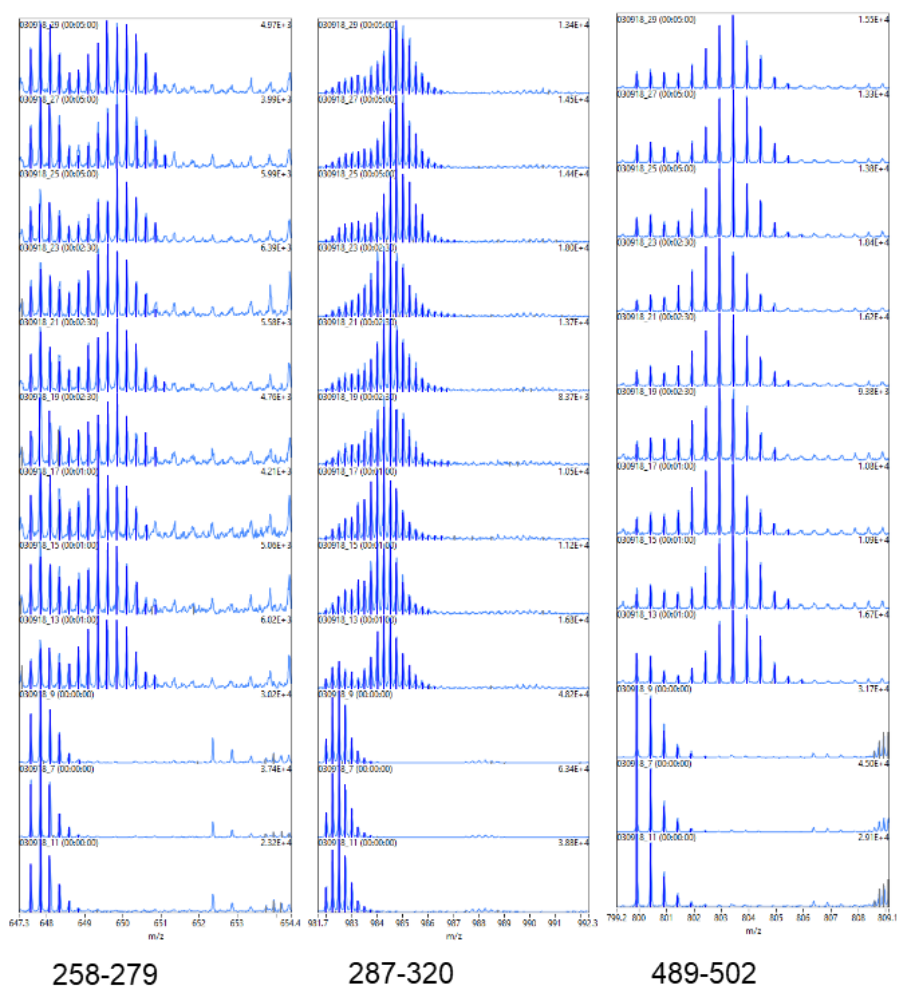
Figure 2.3. Bimodal exchange in OsOSCA1.2. Representative
mass spectra displaying bimodal deuterium uptake. Spectra are
shown in triplicate following 0 sec, 30 sec, 1 min and 5 min of
exchange.

D. Discussion

OsOSCA1.2 shares overall protein fold and topology with other recently determined homologous structures from A. thaliana (9-11). A superposition of these structures with OsOSCA1.2 showed a significant difference (root-mean-square deviation of ~3–4 Å) for the transport pathway-lining helices (TM3–TM7), along with TM0 and TM8 (Fig. 2.4A). When comparing intracellular soluble domains, the extended helical arms of OsOSCA1.2 had noticeable differences compared with those of AtOSCA1 (Fig. 2.4A). These differences are likely due to a combination of conformational flexibility inherent in the detergent-solubilized protein and structural difference between species.

OsOSCA1.2 also shares structural homology to a Ca^{2+}- activated chloride channel (mTMEM16A) and a phospholipid scramblase (NhTMEM16) of the TMEM family when comparing monomeric TM domain regions. However, they differ significantly in the regions of extracellular and intracellular loops and domains, as well as in the intermolecular packing arrangement of the respective dimers. The dimer interface of mTMEM16A buries less surface area (~2%) compared with OsOSCA1.2, and most of the interactions are mediated through the TMs. The intracellular domains of mTMEM16A and NhTMEM16, which are formed by the N and C termini of the molecule, do not contribute to the formation of the dimer (Fig. 2.4B). In contrast, OsOSCA1.2 dimerizes mostly through interactions formed between the opposing intracellular soluble domains. This distinct dimeric packing resulted in a more pronounced offset between protomers that is ~20 Å wider for OsOSCA1.2 compared with NhTMEM16 or mTMEM16A. In our OsOSCA1.2 structure, the extended helical arm in the intracellular soluble domain makes hydrophobic contacts with the loop connecting the gating helix TM6 (Fig. 2.4C), suggesting a possible role for the helical "arms" in sensing the membrane tension and, in turn,

28

transmitting these conformational/mechanical changes to gate transport activity (Fig. 2.4D). This feature is missing in TMEM16 chloride channels, possibly as Ca2+ ions control gating.

Experimental and computational dynamic studies using our OsOSCA1.2 model provide a potential molecular structural basis of how OsOSCA1.2 couples osmotic stress to induce transport gating in the membrane-spanning region. Taken together, both studies predict and support a model in which the extended helical arms (residues 241–266) have the mechanical rigidity and propensity to act as a broadcaster/receiver, ransmitting conformational changes caused by lateral tension in the membrane to TM6 (Figs. 2.2 and 2.4F), which is linked to the predicted gating structure. In addition, information from HDX-MS revealed the presence of bimodal deuterium exchange throughout the OsOSCA1.2, most prominently within the helical arms (residues 258–320) and some extracellular loops (residues 489–511). The bimodal exchange is indicative of multiple correlated unfolding processes occurring in the observed regions (23). Interestingly, in each peptide where bimodal peaks were observed, the 2 peaks remained equal in intensity over the entire course of the experiment, suggesting at least 2 distinct conformational states occupied by the molecular ensemble at equilibrium in the resting state.

Several important questions remain regarding these OSCA proteins and their role in plants. For example, the putative permeant substrates, including calcium and other possible substrates transported by OsOSCA1.2 or by other members within their greater family, are still unknown. It will certainly be a challenge to assign function to all of these proteins individually as these proteins are members of large gene families. Although we present a structure of OsOSCA1.2 along with computational and experimental dynamics, the detailed functional mechanism(s) coupling lateral tension in the membrane by OsOSCA1.2 to gating remains to be addressed in future studies. Furthermore, upstream regulatory proteins, the nature of the

permeant substrate species, and how they are coupled to downstream signaling events remain to

be determined.
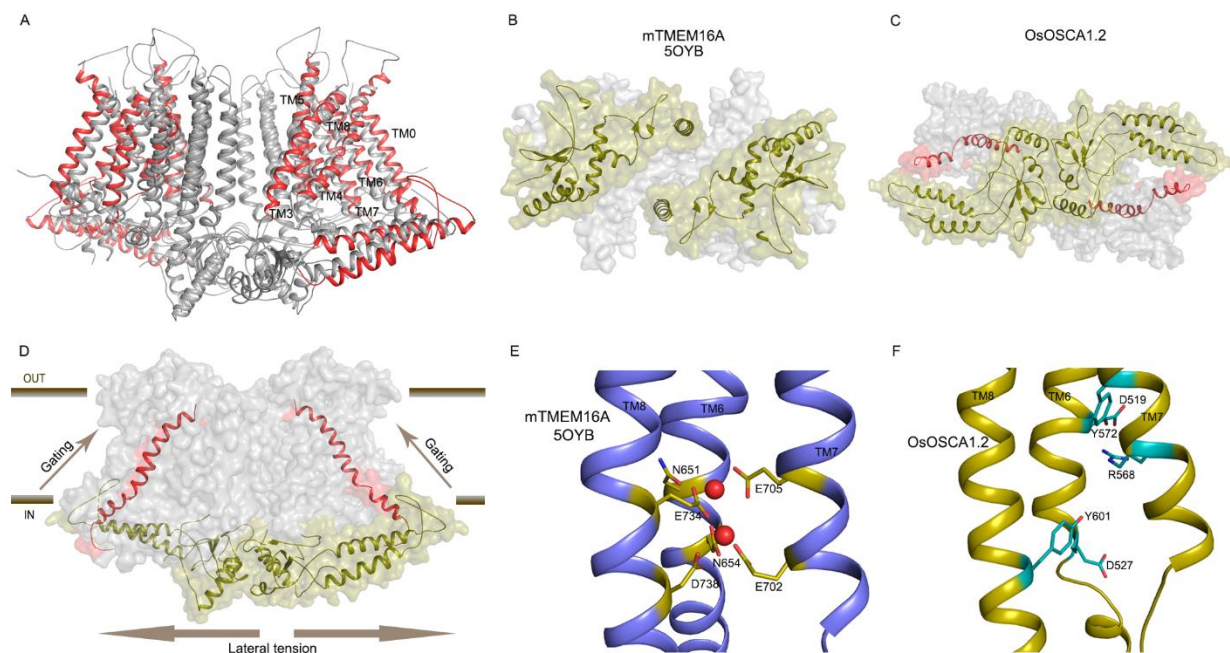
Figure 2.4. Structural comparisons of OsOSCA1.2 with other TMEM and OSCA structures. (A) Superposition of OsOSCA1.2 and AtOSCA1 (PDB: PYD1). TMs 1, 2, 9, and 10 (shown in gray) close to lipid-filled cleft are nearly superimposable and have little relative movement. Pore-lining helices (TMs 3-7) showed significant movement along with TM0 and TM8 (shown in red). **(B)** The mTMEM16A soluble domains from the intercellular side are separated. **(C)** OsOSCA1.2 intracellular soluble domains are together and communicate with channel gating helix TM6. **(D)** The general mechanism of OsOSCA1.2 shown in the plane of the lipid membrane. Lateral tension on the inner leaflet side of the lipid bilayer causes a conformational change in the extended helices of the soluble domain, which is coupled to the gating helix TM6 opening pore. **(E)** Calcium binding site residues of mTMEM16A. Calcium ions are shown as red spheres. **(F)** The corresponding region of OsOSCA1.2 with charged and polar residues are shown in cyan.

Chapter II, in part, is a reprint that the dissertation author significantly contributed to as both a researcher and an author. The material appears in the *Proceedings of the National Academy of Sciences in the United States of America.* (Maity, K., Heumann, J.M., McGrath, A.P., **Kopcho, N.J.**, Hsu, P.K., Lee, C.W., Mapes, J.H., Garza, D., Krishnan, S., Morgan, G.P., Hendargo, K.J., Klose, T., Rees, S.D., Mendrano-Soto, A., Saier, M.H., Pineros, M., Komives, E.A, Schroeder, J.I., Chang, G., Stowell, M.H.B. (2019) "Cryo-EM structure of OSCA1.2 from Oryza sativa elucidates the mechanical basis of potential membrane hyperosmolality gating" *PNAS*. **116**:14309-14318.)

E. References

1.   Yuan F, Yang H, Xue Y, Kong D, Ye R, Li C, Zhang J, Theprungsirikul L, Shrift T, Krichilsky B, Johnson DM, Swift GB, He Y, Siedow JN, & Pei ZM (2014) OSCA1 mediates osmotic-stress-evoked Ca2+ increases vital for osmosensing in Arabidopsis. *Nature* 514:367-371.

2.   Knight H, Trewavas AJ, & Knight MR (1997) Calcium signalling in Arabidopsis thaliana responding to drought and salinity. *Plant J.* 12:1067-1078.

3.   Stephan AB, Kunz HH, Yang E, & Schroeder JI (2016) Rapid hyperosmotic-induced Ca2+ responses in Arabidopsis thaliana exhibit sensory potentiation and involvement of plastidial KEA transporters. *PNAS* 113:E5242-E5249.

4.   Choi WG, Toyota M, Kim SH, Hilleary R, & Gilroy S (2014) Salt stress-induced Ca2+ waves are associated with rapid, long-distance root-to-shoot signaling in plants. *PNAS* 111:6497-6502.

5.   Murthy SE, Dubin AE, Whitwam T, Jojoa-Cruz S, Cahalan SM, Mosavi SAR, Ward AB, & Patapoutian A (2018) OSCA/TMEM63 are an evolutionarily conserved family of mechanically activated ion channels. *eLife* 7:e41844.

6.   Medrano-Soto A, Moreno-Hagelsieb G, McLaughlin D, Ye ZS, Hendargo KJ, & Saier MH (2018) Bioinformatic characterization of the Anoctamin Superfamily of Ca2+-activated ion channels and lipid scramblases. *PLoS One* 13:e0192851.

7.   Adams PD, Afonine PV, Bunkoczi G, Chen VB, Davis IW, Echols N, Headd JJ, Hung LW, Kapral GJ, Grosse-Kunstleve RW, McCoy AJ, Moriarty NW, Oeffner R, Read RJ,

Richardson DC, Richardson JS, Terwilliger TC, & Zwart PH (2010) PHENIX: A comprehensive python-based system for macromolecular structure solution. *Acta Crystallogr. D Biol. Crystallogr.* 66:213-221.

8. Emsley P, Lohkamp B, Scott WG, & Cowtan K (2010) Features and development of Coot. *Acta Crystallogr. D Biol. Crystallogr.* 66:486-501.

9. Jojoa-Cruz S, Saotome K, Murthy SE, Tsui CCA, Sansom MSP, Patapoutian A, & Ward AB (2018) Cryo-EM structure of the mechanically activated ion channel OSCA1.2. *eLife* 7:e41845.

10. Zhang M, Wang D, Kang Y, Wu JX, Yao F, Pan C, Yan Z, Song C, & Chen L (2018) Structure of the mechanosensitive OSCA channels. *Nat. Struct. Mol. Biol.* 25:850-858.

11. Liu X, Wang J, & Sun L (2018) Structure of the hyperosmolality-gated calcium-permeable channel OSCA1.2. *Nat. Commun.* 9:5060.

12. Chen Q, She J, Zeng W, Guo J, Xu H, Bai XC, & Jiang Y (2017) Structure of mammalian endolysosomal TRPML1 channel in nanodiscs. *Nature* 550:415-418.

13. Zhang K (2016) Gctf: Real-time CTF determination and correction. *J. Struct. Biol.* 193:1-12.

14. Scheres SH (2012) A Bayesian view on cryo-EM structure determination. *J. Mol. Biol.* 415:406-418.

15. Punjani A, Rubinstein JL, Fleet DJ, & Brubaker MA (2017) cryoSPARC: Algorithms for rapid unsupervised cryo-EM structure determination. *Nat. Methods* 14:290-296.

16. Kucukelbir A, Sigworth FJ, & Tagare HD (2014) Quantifying the local resolution of cryo-EM density maps. *Nat. Methods* 11:63-65.

17. Barad BA, Echols N, Wang RYR, Cheng Y, DiMaio F, Adams PD, & Fraser JS (2015) EMRinger: Side chain-directed model and map validation for 3D cryo-electron microscopy. *Nat. Methods* 12:943-946.

18. Saier MH, Reddy VS, Tsu BV, Ahmed MS, Li C, & Moreno-Hagelsieb G (2016) The Transporter Classification Database (TCDB): Recent advances. *Nucleic Acids Res.* 44:D372-D379.

19. Brunner JD, Lim NK, Schenck S, Duerst A, & Dutzler R (2014) X-ray structure of a calcium-activated TMEM16 lipid scramblase. *Nature* 516:207-212.

20. Dang S, Feng S, Tien J, Peters CJ, Bulkley D, Lolicato M, Zhao J, Zuberbuhler K, Ye W, Qi L, Chen T, Craik CS, Jan YN, Minor DL, Cheng Y, & Jan LY (2017) Cryo-EM structures of the TMEM16A calcium-activated chloride channel. *Nature* 552:426-429.

32

21. Rai A, Suprasanna P, D'Souza SF, & Kumar V (2012) Membrane topology and predicted RNA-binding function of the 'early responsive to dehydration (ERD4)' plant protein. *PLoS One* 7:e32658.

22. Li H, Chang YY, Lee JY, Bahar I, & Yang LW (2017) DynOmics: Dynamics of structural proteome and beyond. *Nucleic Acids Res.* 45:W374-W380.

23. Li MJ, Guttman M, & Atkins WM (2018) Conformational dynamics of P-glycoprotein in lipid nanodiscs and detergent micelles reveal complex motions on a wide time scale. *J. Biol. Chem.* 293:6297-6307.

Chapter III:

Structural and Dynamic Basis for GPCR-Independent Activation of Heterotrimeric Gi Proteins

A. Introduction

Heterotrimeric G proteins act as molecular switches that gate the flow of information from extracellular cues to intracellular effectors that control cell behavior(1). Canonically, heterotrimeric G protein signaling is initiated exclusively at the plasma membrane where agonist-activated G-Protein Coupled Receptors (GPCRs) activate Gαβγ trimers by promoting the exchange of GDP for GTP on the Gα subunit (1). Heterotrimeric G proteins are expressed in virtually all cell and tissue types in the body and are involved in most physiologic, and many pathologic, processes; thus, the molecular mechanism and structural determinants of G protein activation and action has been a top priority in the field, yielding over 70 publicly available structures in various conformations and complex composition. The structural basis for GPCR-dependent G protein activation had challenged the field for decades, but in the past 8 years, breakthrough structural studies have demonstrated that GPCR-dependent G protein activation occurs via direct disruption the hydrophobic core of the Gα GTPase domain by removal of the C-terminal α5 helix and insertion of the GPCR's intracellular loop 2 (5-8).

In contrast, GPCR-independent activation of heterotrimeric G proteins can occur downstream of non-GPCRs via a novel family of Guanine-nucleotide Exchange Modulators (GEMs) (9, 10). Members of the GEM family are cytosolic proteins that are defined by their unique ability to act as Guanine-nucleotide Exchange Factors (GEFs) to activate Gαi and to act as Guanine-nucleotide Dissociation Inhibitors (GDIs) to inhibit Gαs using the same evolutionarily conserved GEM motif (11, 12), identified based on its homology to the synthetic peptide KB752 (a peptide that can bind and activate Gαi) (13). GEMs activate heterotrimeric G proteins downstream diverse classes of receptors, resulting in spatio-temporal signaling that is distinct from GPCR-driven G protein signaling. Furthermore, GEM-dependent G protein

35

activation has been shown to play a pivotal role in pathophysiology (14), including cancer, organ fibrosis, and diabetes. A structural understanding of the mechanism of GEM-dependent G protein activation would be invaluable towards pharmacologic targeting of GEMs to treat these diseases. Despite vast progress in understanding GEM biology and demonstrable translational relevance of dysregulated GEM signaling in disease, structural mechanistic insights into GEM-dependent G protein activation is lacking. This study fills this void, providing high resolution insight into GPCR-independent, GEM-driven G protein activation

B. Materials and Methods

1. Plasmid Constructs and Mutagenesis

All restriction endonucleases and *Escherichia coli* strain DH5α were purchased from New England Biolabs (Ipswich, MA). For crystallization, biochemical experiments, and HDXMS, rat Gαi3 (Uniprot P08753-1) was cloned into a pET28b vector using NdeI and XhoI restriction sites, resulting in an N-terminal 6xHis tag separated from the Gαi3 protein by the sequence SSGLVPRGSHM. The nucleotide sequences encoding for the tag and the linker was: ATGGGCAGCAGCCATCATCATCATCATCACAGCAGCGGCCTGGTGCCGCGCGGCAG CCAT- followed by the start ATG codon of wild-type (WT) Gαi3; this construct is referred to 6xHis-Gαi3. In the construct used for crystallization, the N-terminal 25 amino acids of Gαi3 were removed to facilitate crystallization as previously done (13); this construct will be referred to as 6xHis-ΔN25-Gαi3. For GST pull down assays, full length Gαi3 was cloned into a pGEX vector with an N-terminal GST-tag, resulting in a GST-Gαi3. All site-directed mutagenesis (Gai3 Q204A, R208Q, K209M, K210M, W211A, H213F, F215A, and V218A, were carried out using QuikChange II site-directed mutagenesis kit (Agilent Technologies; Santa Clara, CA; Ca#200524) as per the manufacturer's protocol. In the main text, all three constructs (6xHis-

36

Gαi3, 6xHis-ΔN25-Gαi3, and GST-Gαi3) are referred to as Gαi; in the methods below, specific

constructs used in each experiment are detailed.

2. Peptides

Peptides were synthesized by three companies independently [LifeTein (Somerset, NJ),

Chempeptide (Shanghai, China), and AbClonal (Woburn, MA)] and all displayed comparable

effects in assays. Peptides were synthesized with L-amino acids at >95% purity and kept frozen

at -80 °C as 10 mM stocks in DMSO.

KB-752 peptide sequence: 1-NH2-SRVTWYDFLMEDTKSR-COOH-16

GIV-WT GEM-motif peptide sequence: 1671-NH2-

KTGSPGSEVVTLQQFLEESNKLTSVQIKSSS-COOH-1701

GIV-Q1683A GEM-motif peptide sequence: 1671-NH2-

KTGSPGSEVVTLAQFLEESNKLTSVQIKSSS –COOH-1701

3. Expression and Purification of Gαi3

6xHis-tagged Gαi3 constructs (6xHis-Gαi3, 6xHis-ΔN25-Gαi3, or single-point mutants

of thereof) were transformed into *E. coli* BL21 (DE3; Invitrogen) cells. Cells were grown in 1 L

flasks at 37 °C until OD reached 0.8-1.0, then induced overnight at 25 °C with 1 mM isopropyl

β-d-1-thiogalactopyranoside (IPTG). Cells were harvested via centrifugation and lysed at 15,000

PSI by a single pass through a cell disruptor (TS-Series; Constant Systems, Inc) in Running

Buffer (RB; 50 mM NaH_2PO_4 pH 7.4, 300 mM NaCl, and 0.5 mM EDTA) supplemented with 2x

Protease Inhibitors (Roche Life Science) and 10 mM imidazole. Cell debris was removed by

ultracentrifugation at 45,000 ×g for 40 min, and the supernatant was loaded on a Ni–NTA His60

Superflow resin (Qiagen) affinity column via fast protein liquid chromatography (AKTA, GE

Life Sciences). The resin was washed with RB+60 mM imidazole, and eluted with RB+300 mM

imidazole. The eluted protein was concentrated at 1500 ×g (Amicon Ultra-15 30 MWCO centrifugal filter; Millipore) and subjected to size exclusion chromatography via Superdex 200 resin (GE Healthcare) equilibrated with storage buffer (20 mM Tris-HCl pH 7.4, 20 mM NaCl, 1 mM MgCl$_2$, and 5% glycerol). Fractions from major peak were pooled, resulting in usually ~1-5 mg/mL Gαi protein. Protein was then aliquoted, flash frozen, and stored at −80 °C. Protein concentration and purity were checked throughout purification via SDS-PAGE and comparison to known amounts of Bovine Serum Albumin (BSA).

GST-alone and GST-tagged Gαi3 constructs (wild type and mutant proteins) were expressed and purified from *Escherichia coli* strain BL21 (DE3; Invitrogen) as described previously. Briefly, cells were grown in 1 L flasks at 37 °C until OD reached 0.8-1.0, then induced overnight at 25 °C with 1 mM IPTG. A bacterial pellet from 1 L of culture was resuspended in 10 ml of GST-lysis buffer (25 mM Tris-HCl, pH 7.5, 20 mM NaCl, 1 mM EDTA, 20% [vol/vol] glycerol, 1% [vol/vol] Triton X-100, 2× protease inhibitor cocktail [Complete EDTA-free; Roche Diagnostics]). Cell lysates were sonicated (4 × 20 s, 1 min between cycles) and then centrifuged at 12,000 × *g* at 4 °C for 20 min. Solubilized proteins were affinity purified on glutathione-Sepharose 4B beads (GE Healthcare) by incubation for 4 hrs at 4 °C. Beads were washed 3 x with 50mM Tris pH 8 and then eluted with GST elution buffer (50 mM Tris pH 8, 10 mM reduced glutathione). Eluted proteins were dialyzed overnight at 4 °C against phosphate-buffered saline (PBS), and stored at −80 °C in aliquots.

4. Hydrogen-deuterium exchange mass spectrometry (HDX-MS) of Gαi3

HDX-MS measurements were made using a Synapt G2Si system (Waters Corporation). Deuterium exchange reactions were carried out by a Leap HDX PAL autosampler (Leap Technologies, Carrboro, NC). Deuterated buffer was prepared by lyophilizing 10 mL of 20 mM

Tris-HCl pH 7.4, 20 mM NaCl, 5 μM GDP and 5% glycerol and resuspending it in 10 mL

99.96% D_2O immediately before use. Each deuterium exchange time point (0 min, 1 min, 2.5

min, 5 min) was measured in triplicate. For each measurement, 5 μL of 100 μM 6xHis-Gαi3

protein [in storage buffer (20 mM Tris-HCl pH 7.4, 20 mM NaCl, 1 mM $MgCl_2$, and 5%

glycerol) was mixed with 55 μL of D_2O buffer at 25 °C. Deuterium exchange was quenched by

combining 50 μL of the deuterated sample with 50 μL of 0.1% formic acid and 3 M guanidinum-

HCl for 1 min at 1 °C. The quenched sample was then injected in a 50 μL sample loop and

digested by an inline pepsin column (Pierce, Inc.) at 15 °C. The resulting peptides were captured

on a BEH C18 Vanguard precolumn, separated by analytical chromatography (Acquity UPLC

BEH C18, 1.7 μm, 1.0 × 50 mm, Waters Corporation) using 7−85% acetonitrile in 0.1% formic

acid over 7.5 min, and analyzed in a Waters Synapt G2Si quadrupole time-of-flight mass

spectrometer following electrospray injection.

Data were collected in Mobility, ESI+ mode, mass acquisition range of 200−2000 (m/z),

scan time 0.4 sec. Continuous lock mass correction was performed using infusion of leu-

enkephalin (m/z = 556.277) every 30 sec (mass accuracy of 1 ppm for calibration standard). For

peptide identification, data were instead collected in MS^E (mobility ESI+) mode. Peptides

masses were identified following triplicate analysis of 10 μM Gαi3, and were analyzed using

PLGS 2.5 (Waters Corporation). Peptides masses were identified using a minimum number of

250 ion counts for low energy peptides and 50 ion counts for their fragment ions; with the

additional constraint that peptide size was greater than 1500 Da. The following parameters were

used to filter peptide sequence matches: minimum products per amino acid of 0.2, minimum

score of 7, maximum MH+ error of 5 ppm, and a retention time RSD of 5%, and the peptides had

to be present in two of the three ID runs collected. After identification in PLGS, peptides were

analyzed in DynamX 3.0 (Waters Corporation). Deuterium uptake for each peptide was calculated by comparing the centroids of the mass envelopes of the deuterated samples with the undeuterated controls. To account for back-exchange and systematic autosampler sample handling differences between the shorter 1 min and longer 2.5 min and 5 min deuteration times, the uptake and standard deviation values were divided by 0.79 and 0.75, respectively. Data were plotted as number of deuterons incorporated vs time. The Y-axis limit for each plot reflects the total number of amides within the peptide that could possibly have exchanged. Each plot includes the peptide MH+ value, sequence, and sequential residue numbering.

5. Co-crystallization of Gαi3 with KB752 and GIV-GEM

Purified 3 mg/mL 6xHis-ΔN25-Gαi3 (either freshly prepped or freeze-thawed once) was incubated overnight in storage buffer (20 mM Tris-HCl pH 7.4, 20 mM NaCl, 1 mM $MgCl_2$, and 5% glycerol) at a 3:1 (peptide:Gαi3) molar ratio at 4°C, then concentrated to ~15 mg/mL and set on 288-well Intelli-Plate trays (Art Robbins Instruments) in 1:1, 1.5:1, and 2:1 volume ratios with mother liquor (12-16% PEG 3350, 0.2 M NH_4Cl) at room temperature. Crystals appeared after 1-2 days and grew to full size in 5-7 days. Crystals were cryoprotected by soaking in mother liquor supplemented with 10% glycerol and flash-frozen with liquid nitrogen.

6. X-ray data collection and structure determination of gαi3 peptide co-crystal Structures

X-ray diffraction data were collected at 100 K at the Lawrence Berkeley National Laboratory Advanced Light Source (8.2.2) and Stanford Synchrotron Radiation Lightsource (9-2) at a single wavelength. All diffraction data were indexed and integrated with MOSFLM, processed with AIMLESS, and truncated with CTRUNCATE within the CCP4 suite of programs (2, 15, 16). Phases were estimated via molecular replacement in Phaser (17), using a previously

published model of human Gαi1 (PDB 1Y3A, for Gαi3·GDP with KB-752) or human Gαi3

(PDB 4G5R, for Gαi3·GDP with GIV-GEM) as a search model. Models underwent rigid-body

and restrained positional refinement using PHENIX.REFINE in the PHENIX software suite (18)

against a maximum likelihood target function, alternated with manual inspection against electron

density maps in Coot (19). Peptides were manually modeled in Coot and refined in the final

rounds of refinement, which also included the application of hydrogens to their riding positions

and simulated annealing. The resulting refinement statistics for each model are included in

Table3.1. Figures displaying crystal packing were prepared using PyMOL

(http://www.pymol.org), and atomic coordinates and structure factors were deposited in the

Protein Data Bank (accession codes 6MHE and 6MHF for KB752 and GIV-GEM co-crystal

structures, respectively).

Table 3.1: X-ray crystallography data collection and refinement statistics.

Data Collection	Gαi3+GIV-GEM (PDB 6MHF)	Gαi3+KB752 (PDB 6MHE)
Space group	$P4_32_12$	$P4_32_12$
Cell dimensions		
a,b,c **(Å)**	83.78, 83.78, 141.37	83.24, 83.24, 133.83
α,β,ɣ (°)	90, 90, 90	90, 90, 90
Beamline	ALS-8.2.2	ALS-8.2.2
Wavelength	0.99997	0.99999
Resolution (Å)	72.08-2.00	66.91-2.20
Rmerge (%)	2.3 (95.7)[1]	5.0 (84.9)[1]
Rpim (%)	1.7 (79.6)[1]	3.3 (60.3)[1]
I/σ (I)	29.5 (1.4)[1]	15.1 (1.6)[1]
CC1/2	0.999 (0.446)[1]	0.994 (0.131)[1]
Completeness (%)	93.9 (99.7)[1]	94.0 (99.7)[1]
Redundancy	4.0 (4.4)[1]	3.7 (3.7)[1]
Observed reflections	147287	100669
Unique reflections	34165	24419
Refinement		
Resolution (Å)	72.08-2.00 (2.05-2.00)[1]	66.91-2.20 (2.27-2.20)[1]
Reflections (working set)	34765	24594
Reflections (test set)	1738	1229
Rwork/Rfree	0.20/0.24	0.23/0.26
R.m.s deviations		
Bond lengths (Å)	0.002	0.002
Bond angles (°)	0.515	0.504
Ramachandran statistics		
Outliers %	0.29	0.29
Favored %	98.84	98.82
Rotamer Outliers %	1.61	1.66
Cβ Deviations	0	0

[1]Values in parentheses are for the highest-resolution shells.

7. Cell culture

Cells were cultured according to American Type Culture Collection (ATCC) guidelines. Briefly, HeLa cells were grown in high glucose DMEM (Sigma; Ca#D5796) supplemented with 10% (vol/vol) FBS (HyClone; Ca#SH30071.03) and penicillin-streptomycin-glutamine (Gibco; Ca#10378-016). For cell lysates, HeLa cells were grown on 10 cm plates and harvested by scraping into 0.5 mL of lysis buffer [20 mM HEPES pH 7.4, 5 mM Mg-acetate, 125 mM K-acetate, 0.4% Triton X-100, 1 mM DTT, 1× Complete Protease Inhibitor Mixture (Roche; Ca#11873580001), and 1× Phosphatase Inhibitor Mixtures 2 and 3 (Sigma; Ca#P5726 and P0044, respectively)] on ice. Cell lysates were incubated for 10 min at 4 °C and were centrifuged at 12,000 ×g for 10 min. Clarified cell lysates were subsequently used in glutathione-S-transferase (GST) pulldown assays.

8. *In vitro* GST pulldown assays

Purified GST-Gαi3 or GST-alone (5 µg) were immobilized on glutathione-Sepharose beads and incubated with binding buffer [50 mM Tris-HCl (pH 7.4), 100 mM NaCl, 0.4% (vol/vol) Nonidet P-40, 10 mM $MgCl_2$, 5 mM EDTA, 30 µM GDP, 2 mM DTT, 1× Complete Protease Inhibitor Mixture (Roche; Ca#11873580001)] for 90 min at room temperature as described before (20-23). Lysates (~250 µg protein) of HeLa cells were added to each tube, and binding reactions were carried out for 4 hr at 4 ºC with constant tumbling in binding buffer [50 mM Tris-HCl (pH 7.4), 100 mM NaCl, 0.4% (vol/vol) Nonidet P-40, 10 mM $MgCl_2$, 5 mM EDTA, 30 µM GDP, 2 mM DTT]. Beads were washed (4X) with 1 mL of wash buffer [4.3 mM Na_2HPO_4, 1.4 mM KH_2PO_4 (pH 7.4), 137 mM NaCl, 2.7 mM KCl, 0.1% (vol/vol) Tween-20, 10 mM $MgCl_2$, 5 mM EDTA, 30 µM GDP, 2 mM DTT] and boiled in Laemmli's sample buffer for 10 min. For immunoblotting, rabbit anti-Gβ primary antibody (M-14; Ca#sc-261) and anti-

GIV-CT primary antibody (T-13; Ca#sc-133371) were obtained from Santa Cruz Biotechnology (Dallas, TX). IRDye 680RD goat anti-rabbit secondary antibody (Ca#926-68071) and IRDye 800 goat anti-mouse secondary antibody (Ca#926-32210) were from Li-Cor Biosciences (Lincoln, NE). Protein samples were separated by SDS-PAGE and transferred to PVDF membranes (Millipore). Membranes were blocked with PBS supplemented with 5% nonfat milk before incubation with primary antibodies (1:500 dilutions overnight at 4 ºC). Blots were washed 3 times in PBS-T [4.3 mM Na_2HPO_4, 1.4 mM KH_2PO_4 (pH 7.4), 137 mM NaCl, 2.7 mM KCl, 0.1% (vol/vol) Tween-20] and incubated with secondary antibodies (1:20,000 dilutions at room temperature for 1 hr). Blots were then washed 3 times in PBS-T and once with PBS before infrared imaging following the manufacturer's protocols using an Odyssey imaging system (Li-Cor Biosciences).

9. Molecular modeling

Models of Gαi•GDP with (pS1674)GIV-GEM, Gαi•GDP with Daple-GEM, and Gαi•GDP with NUCB1-GEM were constructed by homology with the structure of Gαi•GDP with GIV-GEM using ICM versions 3.8-6 to 3.8-7a (Molsoft LLC, San Diego, CA).

The GEM motif peptides from (pS1674)GIV (1671-KTG-pS1674-PGSEVVTLQQFLEESNK-1691) and Daple (1663-ASPSSEMVTLEEFLEESNR-1681) were built *ab initio*; the GEM motif peptide from NUCB1 (305-DTNQDRLVTLEEFLASTQRKEF-326) was extracted from the NMR structure of NUCB1 (PDB 1SNL). The backbone atoms of the peptides were confined to the crystallographic coordinates of the corresponding atoms of GIV-GEM (residues 1676-GSEVVTLQQFLEES-1689 only) via a set of harmonic distance restraints (tethers); the peptide flanks and side-chains were kept unrestrained. Full-atom conformational sampling of the peptides (backbone, side-chains, and positional variables) and the surrounding

side-chains of Gαi was performed using 5×10^6 steps of biased probability Monte Carlo optimization (24) as implemented in ICM, with the repulsive part of the Van der Waals potential capped at 20 kJ/mol. The top scoring pose of each peptide was selected for analysis.

10. Gαi3-limited proteolysis assay

6xHis-Gαi3 or 6xHis-ΔN25-Gαi3 (0.25 mg/ml) was incubated for 150 min at 30 °C in buffer (20 mM HEPES pH 8, 100 mM NaCl, 1 mM EDTA, 10 mM $MgCl_2$, and 1 mM DTT) supplemented with GDP (30 µM) or GTPγS (30 µM). After incubation trypsin was added to the tubes (final concentration 6.25 µg/ml) and samples were incubated for 10 min at 30 °C. Samples were rapidly transferred to ice, reactions were stopped by the addition of Laemmli sample buffer, after which the samples were boiled for 10 min. Proteins were separated by SDS–PAGE and stained with Coomassie blue.

11. MANT-GTPγS incorporation assays

For Gαi3 incorporation assays in the presence of peptide, peptide was pre-bound to Gαi3 prior to running the assay. To equilibrate and pre-bind peptide to Gαi3, 111 nM His-Gαi3 WT or mutants were first incubated in reaction buffer (20 mM HEPES pH 8, 100 mM NaCl, 1 mM EDTA, 10 mM $MgCl_2$, and 1 mM DTT) in 30 °C water bath for 30 min with or without varying concentrations of peptide in a final incubation volume of 250 µL. After equilibration, 72 µL protein-peptide complexes were transferred to a pre-warmed 384-well black flat-bottom plate (in triplicates). The reaction was initiated by injecting 8 µL of 250 nM MANT-GTPγS (Abcam, Cambridge, MA) in each well for a final reaction volume of 80 µL and final concentrations of 100 nM Gαi3, 25 nM MANT-GTPγS and the indicated concentrations of the peptide. MANT-GTPγS incorporation into Gαi3 was quantified, either by FRET [excitation (ex) = 280; emission (em) = 440] or by direct MANT excitation (ex = 350; em = 440), using a microplate fluorescence

45

reader (TECAN Spark 20M). Fluorescence was measured every 30 sec starting immediately after injection of MANT-GTPgS. Raw fluorescence was plotted over time and observed rates (k_{obs}) were determined by fitting a one-phase association curve to the data (GraphPad Prism 7).

12. Differential scanning fluorimetry (Thermal shift assays)

6xHis-Gαi3 WT and mutants (5 μM) were taken in their native state (as purified) or loaded with GDP by incubating it for 150 min at 30 °C in buffer (20 mM HEPES, pH 8, 100 mM NaCl, 1 mM EDTA, 10 mM MgCl2, and 1 mM DTT) supplemented with GDP (1 mM). After loading, 45 μL of 5 μM His-Gαi3 was pipetted into PCR tubes (in triplicates) and 5 μL 200X SYPRO Orange solution freshly made in the same buffer from 5000X stock (Life Technologies S-6650) was added to the protein. A buffer + dye only (no protein) control was also included. Thermal shift assays were run on an Applied Biosystems StepOnePlus Real-Time PCR machine. Mixed protein and dye samples were subjected to increasing temperatures from 25 to 95 °C in half degree increments, holding each temperature for 30 sec and measuring SYPRO fluorescence (using filter 3 for TAMRA^{TM} and NED^{TM} dyes) at each temperature. Melting temperatures were defined as the temperature at which the maximum value for the derivative of signal fluorescence (dF/dt) is achieved (GraphPad Prism 7).

13. Statistical analysis

Each experiment presented in the figures is representative of at least three independent repeats (with at least two technical repeats for each condition within each repeat). Statistical significance between the differences of means was calculated using multiple comparisons in one-way nonparametric ANOVA. All statistics and graphical data presented were prepared using GraphPad Prism. Histograms of MD simulation data were generated in R.

C. Results

1. GIV-GEM binds and stabilizes Switch-II of Gαi

To understand structurally the mechanism of GEM-dependent heterotrimeric G protein activation, the 31-amino acid (aa) GEM motif of GIV/Girdin (aa 1671-KTGSPGSEVVTLQQFLEESNKLTSVQIKSSS-1701) was co-crystallized with GDP-bound rat Gαi3 (henceforth Gαi•GDP) (Table 3.1). In the crystallization construct, the flexible 25-aa long N-terminal helix of Gαi was deleted as done previously (13), and replaced by a His-tag followed by a short linker (SSGLVPRGSHM). The structure was solved to 2.1 Å resolution (Fig. 3.1A-B).

The structure demonstrated that GIV-GEM binds at the typical effector binding interface: the hydrophobic pocket between Sw-II and the α3-helix of Gαi. By forming a short anti-parallel β-sheet with Sw-II residues 204-208, the peptide stabilizes Sw-II in a previously unseen elevated conformation. Key polar contacts at the interface include hydrogen-bonding of GIV E1678 and E1688 to Gαi R208, around which the peptide folds in a loop-helix conformation, and a hydrogen bond from GIV Q1683 with Gαi Q204, a residue known for its role in GTP-hydrolysis (25). The interface also features hydrophobic packing of GIV's F1685 against W211, I212, F215, and W258 of Gαi. Residues L1682-N1690 of GIV form an α-helix that packs favorably across the α3-helix of Gαi (Fig. 3.1B-C). Many, but not all, Gαi residues engaged by GIV-GEM are shared by Gβγ and GoLoco GDIs (Fig. 3.1C-F, Fig. 3.2A), explaining the ability of GIV to dissociate Gαi from both (11, 26).

The basis for the previously described phosphoregulation of GEM activity of GIV (27, 28) is evident from the structure and molecular modeling. A phosphate on the N-terminal S1674 of GIV-GEM is predicted to improve binding by creating an additional polar contact with Gαi R208 (Fig. 3.2A-B). By contrast, a phosphate on the C-terminal S1689 of GIV-GEM would

disrupt a key hydrogen bond that this residue forms with W258 of Gαi (Fig. 3.2C). These findings explain the opposing roles of the two phosphoevents: the former enhances and the latter abrogates the ability of GIV to bind and activate Gαi (27, 28).
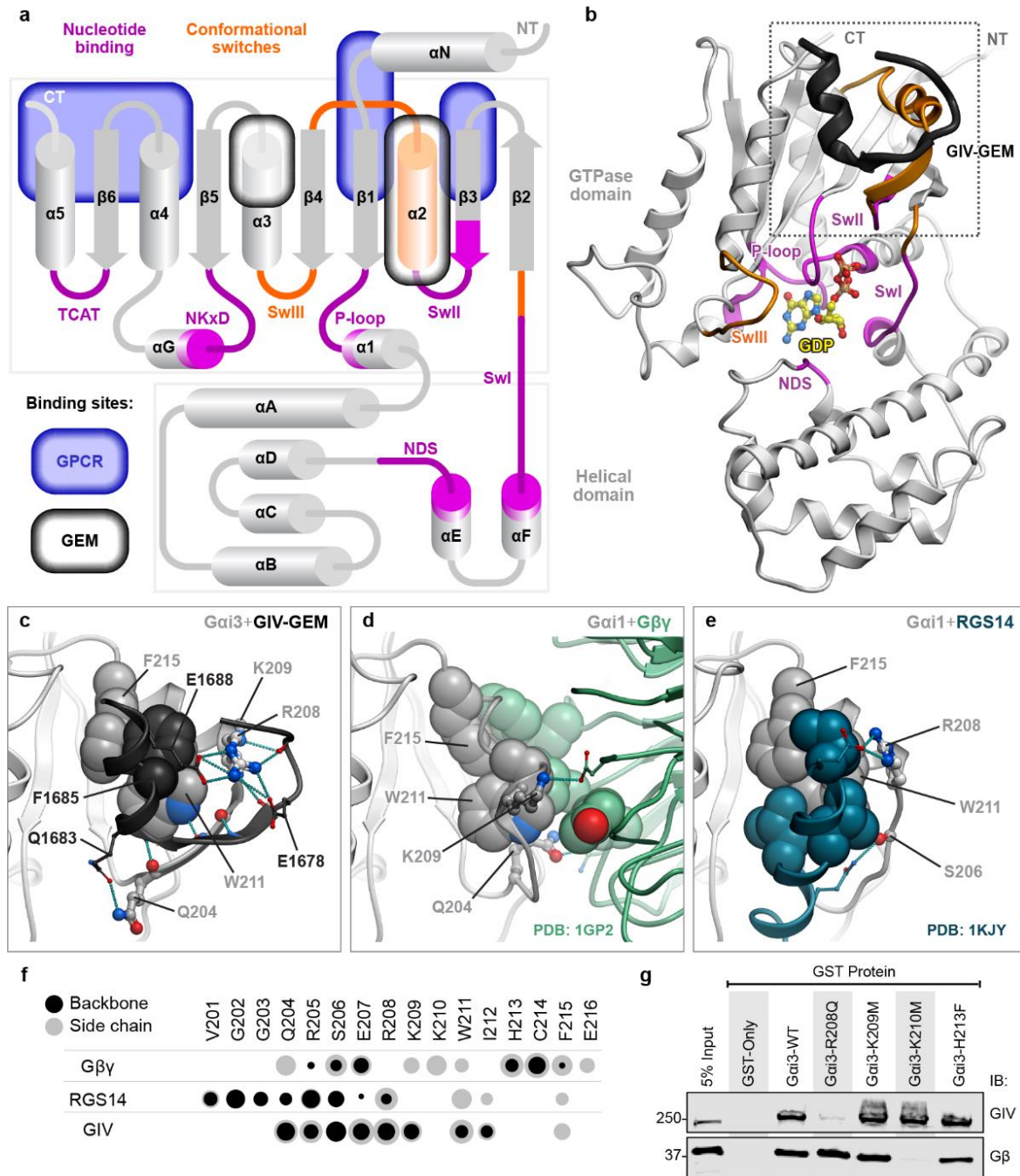
Figure 3.1. GIV-GEM binds Sw-II of Gαi. (A) Topology of Gαi with conformational switches and key binding sites marked. **(B)** Crystal structure of Gαi with GIV-GEM bound at Sw-II. **(C)** A close-up view of the interface between Gαi and GIV-GEM. **(D-E)** Close-up views of Gαi Sw-II bound to Gβγ [(D) PDB 1GP2] or GoLoco-motif GDI RGS14 [(E) PDB 1KJY]. Key Sw-II residues shared by GIV and Gβγ or RGS14 are shown as spheres (aromatic/aliphatic) or sticks (polar). **(F)** Bubble plot displaying the strength and the nature of contacts that Gαi Sw-II residues make with GIV-GEM, Gβγ or RGS14. Dot size is proportional to contact strength. **(G)** Western blot of GST pull-down assay of WT and mutant GST-tagged Gαi with GIV and Gβγ from HeLa lysate.

49
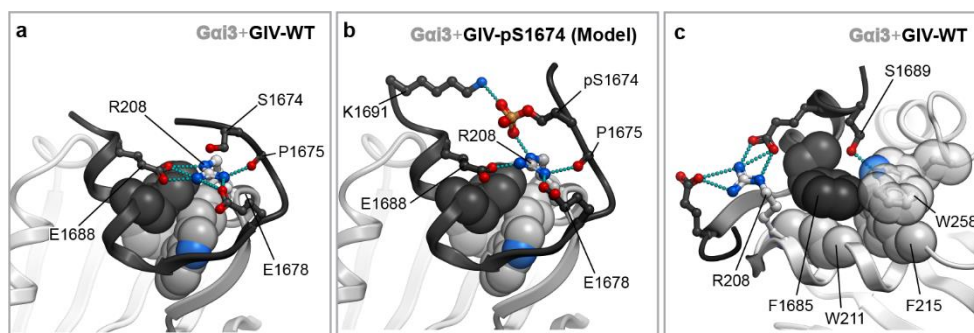
Figure 3.2. Structural basis for phosphoregulation of GIV binding and activity towards Gαi. (A) Structure of WT GIV-GEM, highlighting unphosphorylated S1674 and the various contacts of R208 of Gαi. **(B)** Model of (pS1674)GIV-GEM highlighting the formation of an additional direct contact with R208. **(C)** Structure of WT GIV-GEM, highlighting a polar contact that unphosphorylated S1689 makes with W258 of Gαi.
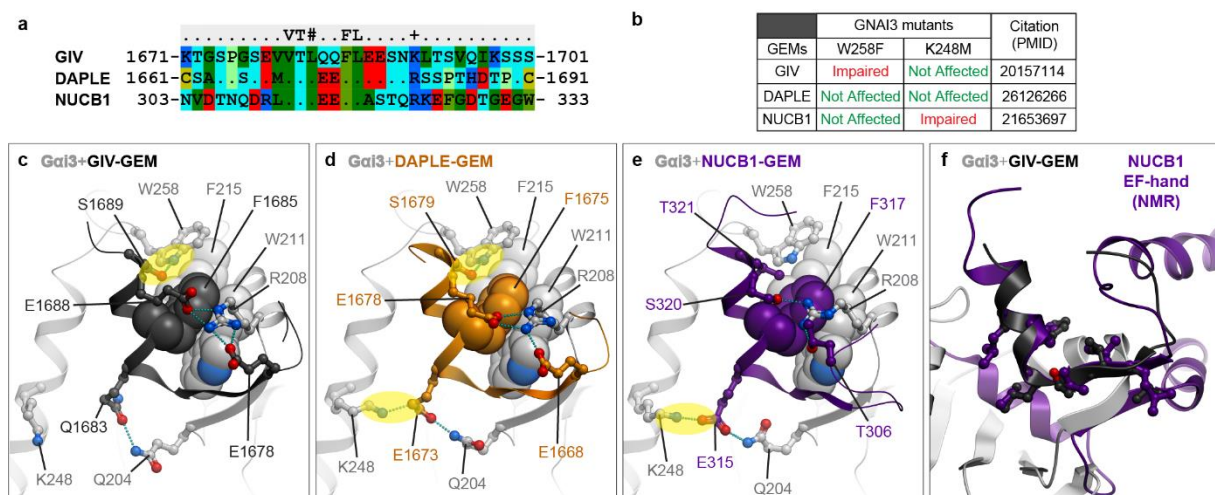
Figure 3.3. Homology models of Gαi•GDP bound to members of the GEM family suggest a conserved mechanism of binding and action. (A) Sequence alignment of the GEM motifs within human GIV, Daple, and NUCB1 (Calnuc) sequences. **(B)** Table summarizing previous mutagenesis studies. **(C)** Crystal structure of GIV-GEM bound to Gαi. **(D-E)**, Homology models of (E) Daple and (E) NUCB1 bound to Gαi created using the GIV-GEM-bound structure as template. Hydrogen bonds explaining the mutagenesis in B are highlighted. **(F)** Overlay of our GIV-GEM-bound Gαi structure with the EF-hand motif of NUCB1, previously determined by NMR (PDB 1SNL).

50

Homology modeling of other GEM family members, Daple and NUCB1, suggested a conserved mode of binding with a few subtle differences that corroborate prior mutagenesis findings (Fig. 3.3A-E) (26, 29, 30). Interestingly, the GEM motif of NUCB1 maps onto one of the EF-hand motifs of this protein (31); modeling suggests not only full compatibility of the EF-hand topology with Gαi Sw-II binding, but also structural mimicry between such binding and the canonical EF-hand-mediated molecular fold (Fig. 3.3F).

In our structure, the N-terminal linker of each Gαi molecule binds to its symmetry neighbor, positioning the linker Arg and surrounding residues across the nucleotide cleft in a manner similar to GoLoco GDIs (Fig. 3.4A-C) (32). Because this interaction was predicted to stabilize the bound GDP, we henceforth refer to the N-terminal linker as the nucleotide-stabilizing linker (NSL). Removal of the NSL (M. Garcia-Marcos, personal correspondence) or changing its position (this work) produced no crystals, suggesting that the linker trapped an otherwise transient and likely non-crystallizable GEF-induced conformation of Gαi•GDP. To determine whether the NSL has confounded structural observations at the GIV-GEM interface with Gαi, we solved the structure of the NSL-containing Gαi•GDP with KB752 (Fig. 3.4D-E) and compared it to a previously published complex *without* the NSL (13). No discernible differences were noted in the Gαi-KB752 interface (Fig. 3.4F), suggesting that the observed features at the Gαi-GIV-GEM interface are also representative of the native interactions.
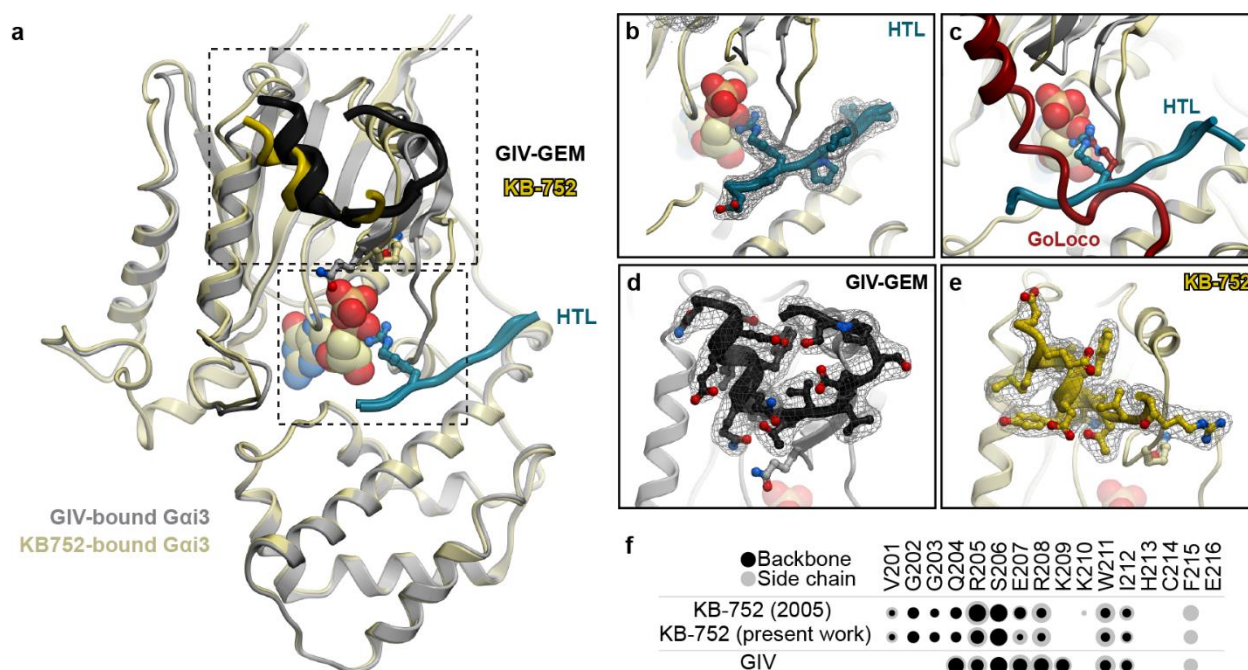
Figure 3.4: Structures of KB752-bound and GIV-GEM-bound Gαi•GDP. (A)
Overlay of our solved KB752-bound and GIV-GEM-bound Gαi•GDP structures.
Boxed regions are highlighted in B-E. **(B)** Fo-Fc electron density map around the
HTL in the Gαi•GDP structure with GIV-GEM is contoured at 3σ. **(C)** Overlay of the
HTL with the GoLoco motif of GDI RGS14 (PDB 1KJY). **(D-E)** Fo-Fc electron
density maps around the GIV-GEM peptide (D) or KB752 (E) are contoured at 3σ.
(F) Bubble plot of the contacts between Sw-II residues of Gαi and the GIV peptide or
the KB752 peptide, as seen in the previously published KB752-bound structure
without the HTL and our solved structures *with* the HTL. The size of the dot is
directly proportional to the strength of the contact (2, 3).

2. GIV-GEM binding disfavors the high-GDP affinity conformations of Gαi SwII and Q204

Upon binding, GIV-GEM accelerates the basal nucleotide exchange of monomeric Gαi

(11). To understand the structural basis for this phenomenon, we compared the newly solved

structure with all previously crystallized GDP-bound complexes of Gαi. The complexes were

organized in order of decreasing GDP affinity, from GoLoco GDI-bound and Gβγ-bound (high

GDP affinity), through GDP-only (basal affinity) to KB752- and GIV-bound (low GDP affinity).

52

A clear trend emerged in the position of Sw-I and the molecular contacts of Q204 in Sw-II. In high-GDP-affinity states, Q204 appears to stabilize Sw-I in an outward position, away from the nucleotide-binding pocket (Fig. 3.5A-B). By contrast, in the KB752-bound Gαi structure, Q204 is displaced away from Sw-I allowing the latter to "collapse" towards the bound nucleotide (Fig. 3.5D). GIV-GEM produces a similar but more exacerbated effect: it stabilizes an elevated conformation of Sw-II, hydrogen-bonds to Gαi Q204 via Q1683 and pulls it ~11 Å away from Sw-I, leading to an even greater contraction of the GDP binding site that also involves a displacement of the β2-strand (Fig. 3.5E-F). Despite this collapse, the N-terminal part of Sw-I is found in the outward position, likely due to the presence of the NSL (Fig. 3.5E).

These observations prompted us to probe the role of Gαi Q204 in GIV-GEM-mediated GDP-release. A Q204A mutant was generated and tested in a kinetic assay where GDP released from Gαi is replaced by MANT-GTPγS, a non-hydrolyzable fluorescent GTP analogue (33, 34). Because GDP release is the rate-limiting step of nucleotide exchange, increases in MANT-GTPγS incorporation rate by Gαi reflect the acceleration of GDP release (35). Compared to WT, Gαi-Q204A displayed a small but consistent increase in the basal nucleotide exchange rate (1.28-fold; Fig. 3.5G-H); however, it was significantly more sensitive to activation by GIV-GEM (3.25-fold compared to 1.84-fold for WT Gαi; Fig. 3.5G-H). These findings suggest that Q204 indeed negatively regulates nucleotide exchange, likely by stabilizing Sw-I in the high-GDP-affinity state. Interestingly, the direct contact between GIV Q1683 and Gαi Q204 appears unnecessary for accelerated nucleotide exchange because a GIV-Q1683A mutant fully retained its GEF function.
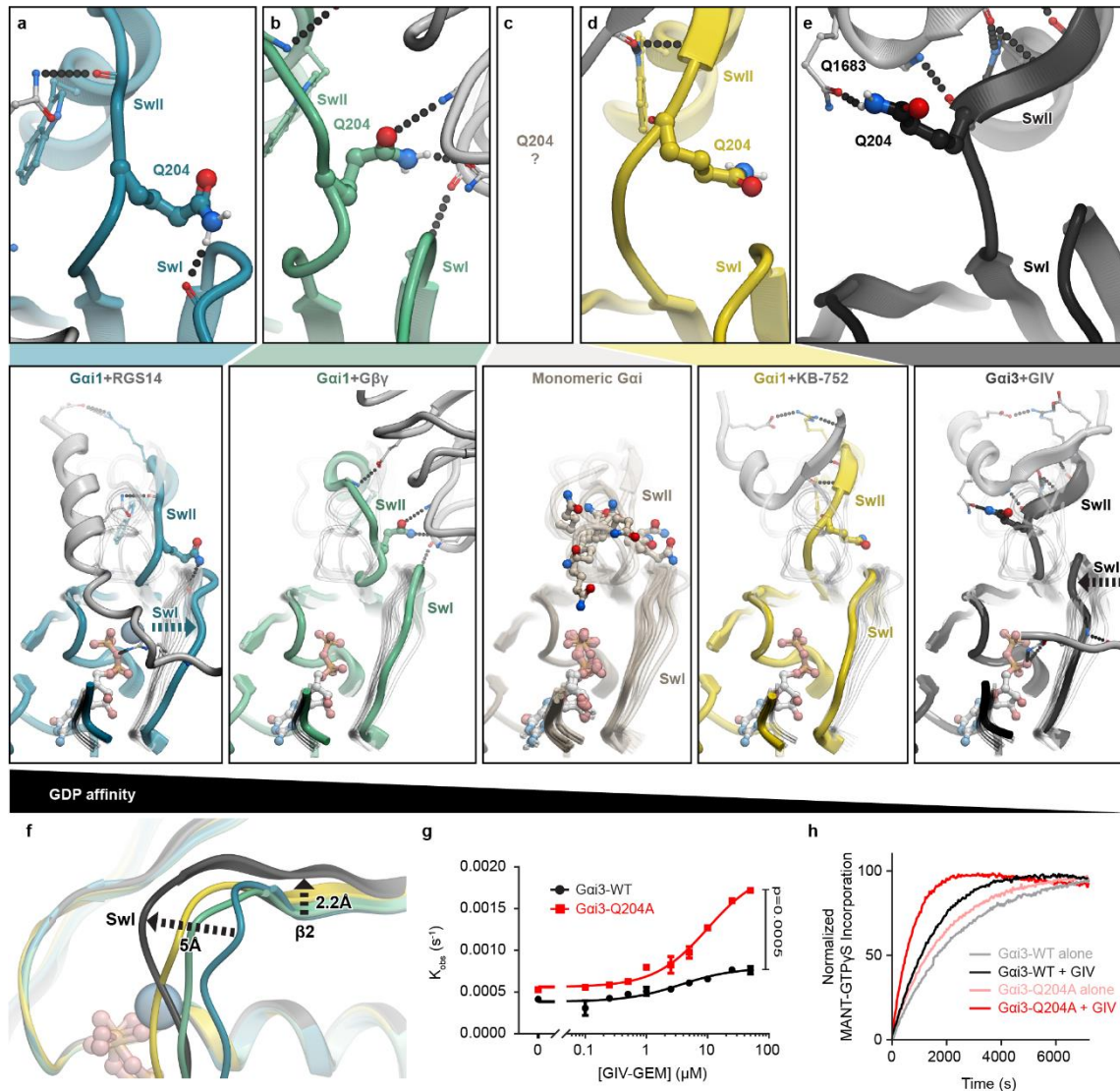
Figure 3.5. GIV binding to Sw-II of Gαi disrupts GDP-stabilizing interactions between Sw-II and Sw-I and induces a low-GDP-affinity conformation of Gαi. (A-E) Comparison of Sw-I, Sw-II, and Q204 in GDP-bound structures, arranged from high (left) to low (right) GDP-affinity. **(F)** Overlay of structures shown in (A-E), highlighting differences in Sw-I and the β2-strand. **(G)** MANT-GTPγS incorporation into WT and Q204A Gαi proteins was assessed in the presence of varying concentrations of WT GIV-GEM peptide. Findings are displayed as a line graph showing observed rates (k_{obs}, s^{-1}) for nucleotide incorporation. Data shown is triplicates from a representative experiment; $n = 3$. **(H)** Same data as in (G) presented as a line graph showing average nucleotide incorporation over time in the presence or absence of 50 μM WT GIV-GEM peptide. Statistical significance between means was calculated using multiple comparisons in one-way nonparametric ANOVA.

3. Binding of GIV-GEM to Gαi overcomes the allosteric GDP-stabilizing role of hydrophobic residues in SwII

Besides Q204, GIV-GEM also directly engages the aromatic residues W211 and F215 in Sw-II of Gαi; these residues were previously proven critical for GIV-GEM binding (11). We hypothesized that the packing of these bulky hydrophobic residues against the β-barrel of the GTPase domain may stabilize GDP in the basal state (Fig. 3.6A). If so, binding of GIV-GEM to Sw-II may neutralize such GDP-stabilizing effects to stimulate GDP release. Alanine substitutions, W211A or F215A, resulted in substantial increases in the basal nucleotide exchange rate of Gαi in MANT-GTPγS incorporation assays (2.48- and 1.84-fold increases, respectively; Fig. 3.6B-C). Mutation of a hydrophobic residue on Sw-II that is not necessary for GIV-GEM binding, V218A, showed a small decrease in nucleotide exchange rate (Fig. 3.6B-C). Consistent results were obtained in thermal stability assays where the two fast-exchanging Gαi mutants, W211A and F215A, displayed lower melting temperatures in both native and GDP-bound state compared to WT and V218A Gαi (Fig. 3.7). These results suggest that W211 and F215 on Sw-II contribute to stabilization of the bound GDP, an effect that is neutralized by GIV-GEM binding.

To understand the global allosteric changes in Gαi caused by the loss of bulky hydrophobics in Sw-II, we subjected WT and mutant Gαi to hydrogen-deuterium exchange mass spectrometry (HDX-MS): a sensitive technique that uses deuterium labeling of protein backbone amides (36) to probe conformational dynamics and mutation-induced allostery (37, 38). The V218A mutant showed no measurable difference in deuterium uptake compared to WT Gαi (Fig. 3.6D). By contrast, the fast-exchanging W211A mutant exhibited regions of higher deuterium uptake indicative of increased dynamics. The fragment spanning Sw-I and the β2-strand

(residues 176-191) showed the highest increase in deuterium uptake in the W211A mutant compared to the WT protein (7.20% increase; Fig. 3.6E). Other regions with increased deuterium uptake in the mutant include the C-terminal end of the α4-helix through the β6-strand (residues 311-323 and 308-323, 5.23% increase) and the αD-αE (NDS) loop (residues 140-154, 4.24% increase) (Fig. 3.6E). Although it is impossible to state whether these changes are a trigger or a consequence of GDP release, the findings are consistent with the role of W211 on Sw-II as an allosteric stabilizer of Sw-I and the β2-strand of Gαi, and thus, of the overall high-GDP-affinity state of the protein.
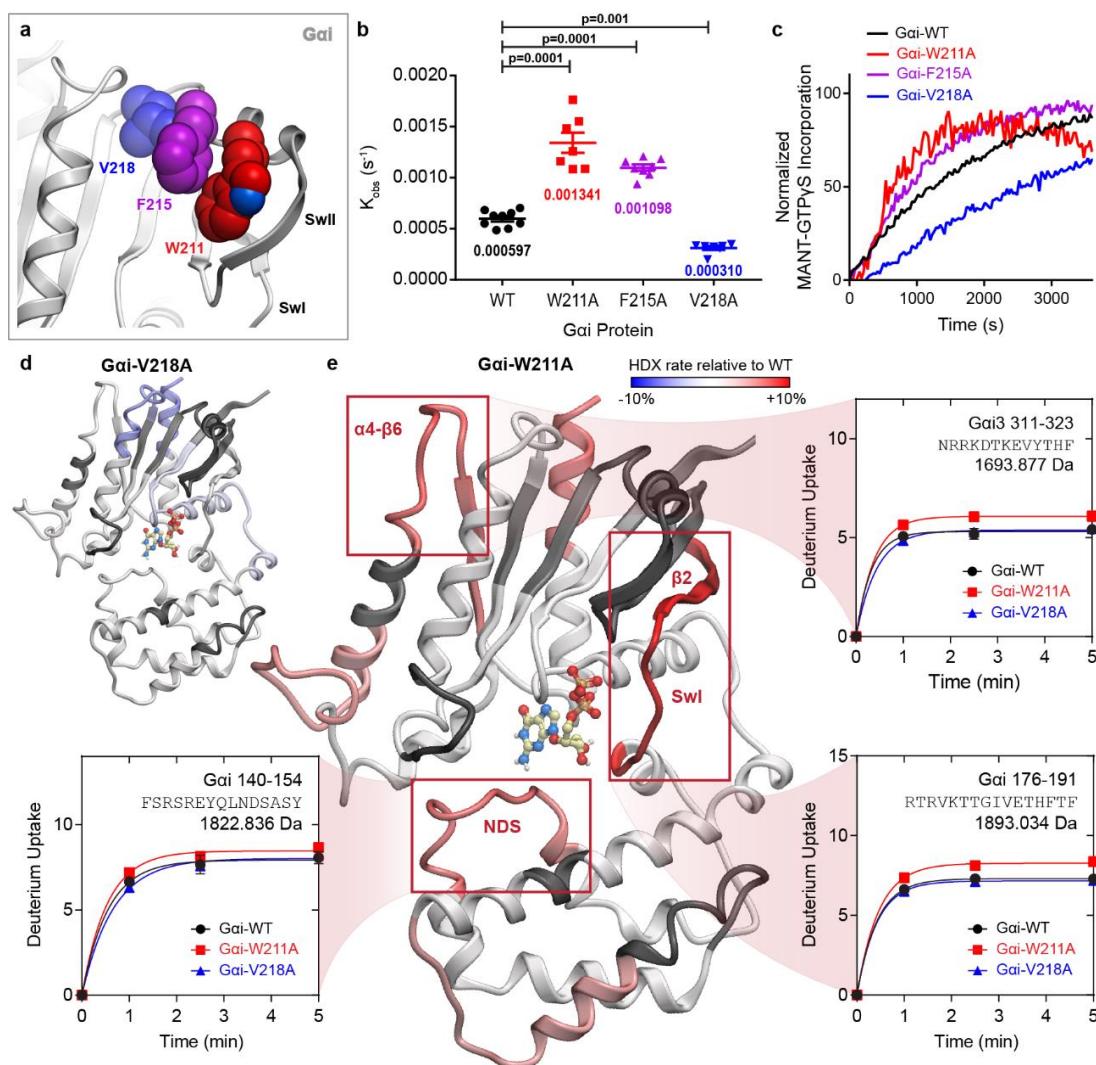
Figure 3.6. Hydrophobic residues in Sw-II of Gαi engaged by GIV stabilize GDP and influence the dynamics of Sw-I and the β2-strand. (A) Structure showing hydrophobic residues in Sw-II of Gαi that were subjected to mutagenesis. **(B-C)** MANT-GTPγS incorporation into WT, W211A, F215A, and V218A Gαi. Findings are displayed as a dot plot (B) showing the observed nucleotide incorporation rates (k_{obs}, s^{-1}) and as line graphs (C) showing average nucleotide incorporation over time. Data shown is from three independent experiments; n = 9, 7, 8 and 7 for WT, W211A, F215A, and V218A, respectively. **(D-E)**, Differences in relative deuterium uptake between V218A and WT Gαi (D) and between W211A and WT Gαi (E) at 5 min, as determined by triplicate HDX-MS assays. Blue and red coloring corresponds to -10% and +10% change, respectively, black indicates regions that were not mapped. Regions exhibiting increased uptake in the W211A mutant are highlighted and the corresponding deuterium uptake plots shown (standard deviation error bars are within the symbols). Statistical significance between means was calculated using multiple comparisons in one-way nonparametric ANOVA.
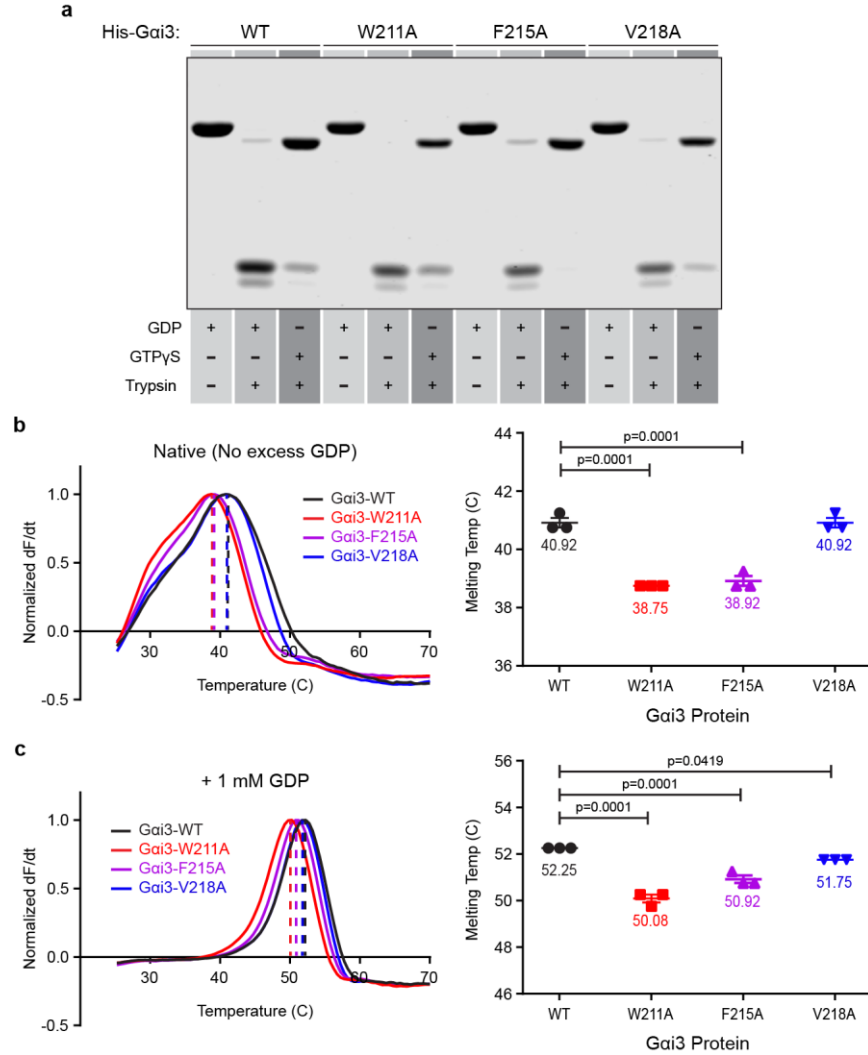
Figure 3.7. Trypsin proteolysis and thermal shift assays support the GDP-stabilizing role of Sw-II residues W211 and F215. (A) Coomassie stain of a trypsin proteolysis assay performed on WT and Sw-II mutant Gαi proteins loaded with GDP or GTPγS. **(B)** WT and Sw-II mutant Gαi proteins were subjected to increasing temperatures in differential scanning fluorimetry (thermal shift) assay. Findings are displayed as a line graph (left) showing average normalized dF/dt curves of *Native* (no excess GDP added) or as dot plot (right) showing the melting temperatures of *Native* WT and Sw-II mutant Gαi proteins. Peaks of the curves (left) represent protein melting temperatures. Data shown are triplicates from a representative experiment; n = 3. **(C)** Same as in (B) except 1 mM GDP was added.

D. Discussion

Overall, this work provides the first atomic level structure of a naturally occurring GEM bound to Gαi. The structure provides mechanistic insights into key aspects of GEM biology, including the ability of GEMs to dissociate Gαi complexes with Gβγ (thereby initiating Gβγ signaling) and GoLoco-containing proteins (thereby antagonizing the GDI action of such proteins) (11, 20). The structure also explains the basis for phosphoregulation of GIV-GEM.

Furthermore, this study elucidates the mechanism by which GEMs accelerate GDP release from Gαi. HDX-MS and nucleotide exchange experiments reveal a previously unknown role of Gαi Sw-II in nucleotide affinity. Stabilization of the elevated Sw-II conformation by GIV-GEM releases conformational constraints on Sw-I and β2-β3 strands of Gαi, allowing for inward collapse of the former and higher mobility of the latter. This perturbation propagates to the hydrophobic core in the center of the GTPase domain that was previously shown to contribute to both basal and GPCR-accelerated nucleotide exchange in Gαi (39, 40). Furthermore, structures of GPCR-bound G proteins demonstrate that GPCRs directly disrupt this core by inserting into it a hydrophobic residue from the intracellular loop 2 (5-8). Thus, our findings suggest that despite binding at non-overlapping interfaces on Gαi, GEMs and GPCRs share a part of their allosteric mechanism for acceleration of GDP release by both disrupting the hydrophobic core of the GTPase domain of Gαi (Fig. 3.6). These similarities escaped detection in earlier studies employing molecular modeling (11) and NMR (41).

Because nucleotide exchange is an inherently dynamic process, our serendipitously identified NSL has likely facilitated the crystallization of an otherwise unstable and transient complex, much like the intentionally introduced conformation-specific nanobodies in other GEF-bound structures of G proteins (5). While the insights from the structure alone may be limited by

its static nature and possibly the presence of the NSL, the complementary computational,

biophysical, and biochemical experiments provide a holistic understanding of the diverse

mechanisms for allosteric regulation of Gαi.

Chapter III, in part, is a reprint that the dissertation author significantly contributed to as

both a researcher and an author. The material appears in the *Proceedings of the National

Academy of Sciences in the United States of America*. (Kalogriopoulos, N., Rees, S.D., Ngo, T.,

Kopcho, N.J., Ilatovskiy, A.V., Sun, N., Komives, E.A, Chang, G., Ghosh, P., Kufareva, I.

(2019) "Structural basis for GPCR-independent activation of heterotrimeric Gi proteins" *PNAS*.

116: 16394-16403.)

E. References
1.	Gilman AG (1987) G proteins: transducers of receptor-generated signals. *Annu. Rev. Biochem.* 56:615-649.

2.	Wall MA, Coleman DE, Lee E, Iniguez-Lluhi JA, Posner BA, Gilman AG, & Sprang SR (1995) The structure of the G protein heterotrimer Gi alpha 1 beta 1 gamma 2. *Cell* 83(6):1047-1058.

3.	Battye TG, Kontogiannis L, Johnson O, Powell HR, & Leslie AG (2011) iMOSFLM: a new graphical interface for diffraction-image processing with MOSFLM. *Acta Crystallogr. D Biol Crystallogr.* 67:271-281.

4.	Morris AJ & Malbon CC (1999) Physiological regulation of G protein-linked signaling. *Physiol. Rev.* 79:1373-1430.

5.	Rasmussen SG, DeVree BT, Zou Y, Kruse AC, Chung KY, Kobilka TS, Thian FS, Char PS, Pardon E, Calinski D, Mathiesen JM, Shah ST, Lyons JA, Caffrey M, Gellman SH, Steyaert J, Skiniotis G, Weis WI, Sunahara RK, & Kobilka BK (2011) Crystal structure of the β2 adrenergic receptor–Gs protein complex. *Nature* 477:549-555.

6.	Koehl A, Hu H, Maeda S, Zhang Y, Qu Q, Paggi JM, Latorraca NR, Hilger D, Dawson R, Matile H, Schertler GFX, Granier S, Weis WI, Dror RO, Manglik A, Skiniotis G, & Kobilka BK (2018) Structure of the micro-opioid receptor-Gi protein complex. *Nature* 558:547-552.

7.   Carpenter B, Nehme R, Warne T, Leslie AG, & Tate CG (2016) Structure of the adenosine A(2A) receptor bound to an engineered G protein. *Nature* 536:104-107.

8.   Draper-Joyce CJ, Khoshouei M, Thal DM, Liang Y, Nguyen ATN, Furness SGB, Venugopal H, Baltos J, Plitzko JM, Danev R, Baumeister W, May LT, Wootten D, Sexton PM, Glukhova A, & Christopoulos A (2018) Structure of the adenosine-bound human adenosine A1 receptor-Gi complex. *Nature* 558:559-563.

9.   Aznar N, Kalogriopoulos N, Midde KK, & Ghosh P (2016) Heterotrimeric G protein signaling via GIV/Girdin: Breaking the rules of engagement, space, and time. *Bioassays* 38:379-393.

10.   Ghosh P, Rangamani P, & Kufareva I (2017) The GAPs, GEFs, GDIs and...now, GEMs: New kids on the heterotrimeric G protein signaling block. *Cell Cycle* 16:607-612.

11.   Garcia-Marcos M, Ghosh P, & Farquhar MG (2009) GIV is a nonreceptor GEF for G alpha i with a unique motif that regulates Akt signaling. *PNAS* 106:3178-3183.

12.   Gupta V, Bhandari D, Leyme A, Aznar N, Midde KK, Lo IC, Ear J, Niesman I., Lopez-Sanchez I, Blanco-Canosa JB, von Zastrow M, Garcia-Marcos M, Farquhar MG, & Ghosh P (2016) GIV/Girdin activates Galphai and inhibits Galphas via the same motif. *PNAS* 113:E5721-5730.

13.   Johnston CA, Willard FS, Jezyk MR, Fredericks Z, Bodor ET, Jones MB, Blaesius R, Watts VJ, Harden TK, Sondek J, Ramer JK, & Siderovski DP (2005) Structure of Galpha(i1) bound to a GDP-selective peptide provides insight into guanine nucleotide exchange. *Structure* 13:1069-1080.

14.   Ghosh P (2015) Heterotrimeric G proteins as emerging targets for network based therapy in cancer: End of a long futile campaign striking heads of a Hydra. *Aging* 7:469-474.

15.   Evans P (2006) Scaling and assessment of data quality. *Acta Crystallogr. D Biol Crystallogr.* 62:72-82.

16.   Winn MD, Ballard CC, Cowtan KD, Dodson EJ, Emsley P, Evans PR, Keegan RM, Krissinel EB, Leslie AG, McCoy A, McNicholas SJ, Murshudov GN, Pannu NS, Potterton EA, Powell HR, Read RJ, Vagin A, & Wilson KS (2011) Overview of the CCP4 suite and current developments. *Acta Crystallogr. D Biol Crystallogr.* 67:235-242.

17.   McCoy AJ, Grosse-Kunstleve RW, Adams PD, Winn MD, Storoni LC, & Read RJ (2007) Phaser crystallographic software. *J. Appl. Crystallogr.* 40:658-674.

18.   Adams PD, Afonine PV, Bunkoczi G, Chen VB, Davis IW, Echols N, Headd JJ, Hung LW, Kapral GJ, Grosse-Kunstleve RW, McCoy AJ, Moriarty NW, Offner R, Read RJ, Richardson DC, Richardson JS, Terwilliger TC, & Zwart PH (2010) PHENIX: a

comprehensive Python-based system for macromolecular structure solution. *Acta Crystallogr. D Biol Crystallogr.* 66:213-221.

19.   Emsley P, Lohkamp B, Scott WG, & Cowtan K (2010) Features and development of Coot. *Acta Crystallogr. D Biol Crystallogr.* 66:486-501.

20.   Garcia-Marcos M, Ear J, Farquhar MG, & Ghosh P (2011) A GDI (AGS3) and a GEF (GIV) regulate autophagy by balancing G protein activity and growth factor signals. *Mol. Biol. Cell* 22:673-686.

21.   Ghosh P, Beas AO, Bornheimer SJ, Garcia-Marcos M, Forry EP, Johannson C, Ear J, Jung BH, Cabrera B, Carethers JM, & Farquhar MG (2010) A G{alpha}i-GIV molecular complex binds epidermal growth factor receptor and determines whether cells migrate or proliferate. *Mol. Biol. Cell* 21:2338-2354.

22.   Ghosh P, Garcia-Marcos M, Bornheimer SJ, & Farquhar MG (2008) Activation of Galphai3 triggers cell migration via regulation of GIV. *J. Cell Biol.* 182:381-383.

23.   Lin C, Ear J, Pavlova Y, Mittal Y, Kufareva I, Ghassemian M, Abagyan R, Garcia-Marcos M, & Ghosh P (2011) Tyrosine phosphorylation of the Galpha-interacting protein GIV promotes activation of phosphoinositide 3-kinase during cell migration. *Sci. Signal* 4:ra64.

24.   Abagyan R & Totrov M (1994) Biased probability Monte Carlo conformational searches and electrostatic calculations for peptides and proteins. *J. Mol. Biol.* 235:983-1002.

25.   Sprang SR (2015) Invited review: Activation of G proteins by GTP and the mechanism of Galpha-catalyzed GTP hydrolysis. *Biopolymers* 105:449-462.

26.   Garcia-Marcos M, Kietrsunthorn PS, Wang H, Ghosh P, & Farquhar MG (2011) G Protein binding sites on Calnuc (nucleobindin 1) and NUCB2 (nucleobindin 2) define a new class of G(alpha)i-regulatory motifs. *J. Biol. Chem.* 286:28138-28149.

27.   Bhandari D, Lopez-Sanchez I, To A, Lo IC, Aznar N, Leyme A, Gupta V, Niesman I, Maddox AL, Garcia-Marcos M, Farquhar MG, & Ghosh P (2015) Cyclin-dependent kinase 5 activates guanine nucleotide exchange factor GIV/Girdin to orchestrate migration-proliferation dichotomy. *PNAS* 112:E4874-4883.

28.   Lopez-Sanchez I, Garcia-Marcos M, Mittal Y, Aznar N, Farquhar MG, & Ghosh P (2013) Protein kinase C-theta (PKCtheta) phosphorylates and inhibits the guanine exchange factor, GIV/Girdin. *PNAS* 110:5510-5515.

29.   Garcia-Marcos M, Ghosh P, Ear J, & Farquhar MG (2010) A structural determinant that renders G alpha(i) sensitive to activation by GIV/girdin is required to promote cell migration. *J. Biol. Chem.* 285:12765-12777.

30.   Aznar N, Midde KK, Dunkel Y, Lopez-Sanchez I, Pavlova Y, Marivin A, Barbazan J, Murray F, Nitsche U, Janssen K, Willert K, Goel A, Abal M, Garcia-Marcos M, & Ghosh P (2015) Daple is a novel non-receptor GEF required for trimeric G protein activation in Wnt signaling. *Elife* 4:e07091.

31.   de Alba E & Tjandra N (2004) Structural studies on the Ca2+-binding domain of human nucleobindin (calnuc). *Biochemistry* 43:10039-10049.

32.   Kimple RJ, Kimple ME, Betts L, Sondek J, & Siderovski DP (2002) Structural determinants for GoLoco-induced inhibition of nucleotide release by Galpha subunits. *Nature* 416:878-881.

33.   Remmers AE (1998) Detection and quantitation of heterotrimeric G proteins by fluorescence resonance energy transfer. *Anal. Biochem.* 257:89-94.

34.   Goricanec D, Stehle R, Egloff P, Grigoriu S, Pluckthun A, Wagner G, & Hagn F (2016) Conformational dynamics of a G-protein alpha subunit is tightly regulated by nucleotide binding. *PNAS* 113:E3629-3638.

35.   Ferguson KM, Higashijima T, Smigel MD, & Gilman AG (1986) The influence of bound GDP on the kinetics of guanine nucleotide binding to G proteins. *J. Biol. Chem.* 261(7393-7399).

36.   Wales TE & Engen JR (2006) Hydrogen exchange mass spectrometry for the analysis of protein dynamics. *Mass Spectrom. Rev.* 25:158-170.

37.   Peacock RB, Davis JR, Markwick PRL, & Komives EA (2018) Dynamic consequences of mutation of tryptophan 215 in thrombin. *Biochemistry* 57:2694-2703.

38.   Kant R, Zeng B, Thomas CJ, Bothner B, & Sprang SR (2016) Ric-8A, a G protein chaperone with nucleotide exchange activity induces long-range secondary structure changes in Galpha. *Elife* 5:e19238.

39.   Kaya AI, Lokits AD, Gilbert JA, Iverson TM, Meiler J, & Hamm HE (2016) A Conserved Hydrophobic Core in Galphai1 Regulates G Protein Activation and Release from Activated Receptor. *J. Biol. Chem.* 291:19674-19686.

40.   Kaya AI, Lokits AD, Gilbert JA, Iverson TM, Meiler J, & Hamm HE (2014) A conserved phenylalanine as a relay between the alpha5 helix and the GDP binding region of heterotrimeric Gi protein alpha subunit. *J. Biol. Chem.* 289:24475-24487.

41.   de Opakua AI, Parag-Sharma K, DiGiacomo V, Merino N, Leyme A, Marivin A, Villate M, Nguyen LT, de la Cruz-Morcillo MA, Blanco-Canosa JB, Ramachandran S, Baillie GS, Cerione RA, Blanco FJ, & Garcia-Marcos M (2017) Molecular mechanism of Galphai activation by non-GPCR proteins with a Galpha-Binding and Activating motif. *Nat. Commun.* 8:15163.

Chapter IV:

Dynamics of ABC Transporter P-glycoprotein

in Three Conformational States

A. Introduction

ATP Binding Cassette (ABC) transporters comprise one of the largest families of membrane proteins. These proteins utilize ATP hydrolysis to drive substrate transport across a cell membrane. The first identified mammalian ABC transporter, P-glycoprotein, transports a diverse pool of substrate molecules unidirectionally out of cells (1), extruding metabolites and preventing the entry of toxic molecules. P-gp has also been directly linked to numerous disease pathologies, such as tumor multidrug resistance (2) and the progression of cerebral amyloidosis (3).

Structurally, P-gp is well established and consists of two homologous segments connected by a flexible linker on a single polypeptide chain (Fig. 4.1A). Each half of the molecule contains six transmembrane helices and one cytosolic nucleotide binding domain (NBD). Like many other ABC transporters, P-gp is believed to alternate between two distinct conformational states during the transport cycle: an inward-facing conformation capable of binding intracellular transport substrates, and an outward-facing conformation oriented to eject substrates across the membrane (4). The first crystal structure of P-gp was observed in the inward-facing conformation, with the two NBDs separated from one another and a large substrate binding pocket exposed to the cytosol and inner membrane leaflet (5). Numerous structures of inward-facing P-gp have been determined since then (6-8).

During transport, P-gp binds to two ATP molecules and the NBDs dimerize in a head-to-tail arrangement, occluding the binding pocket from the intracellular environment. Dimerization is accompanied by ATP hydrolysis at the NBDs and the outward movement of extracellular (EC) helices on the opposite end of the transporter, resulting in a post-transport outward-facing conformation (Fig. 4.1B). These rearrangements open the binding pocket to the EC environment

65
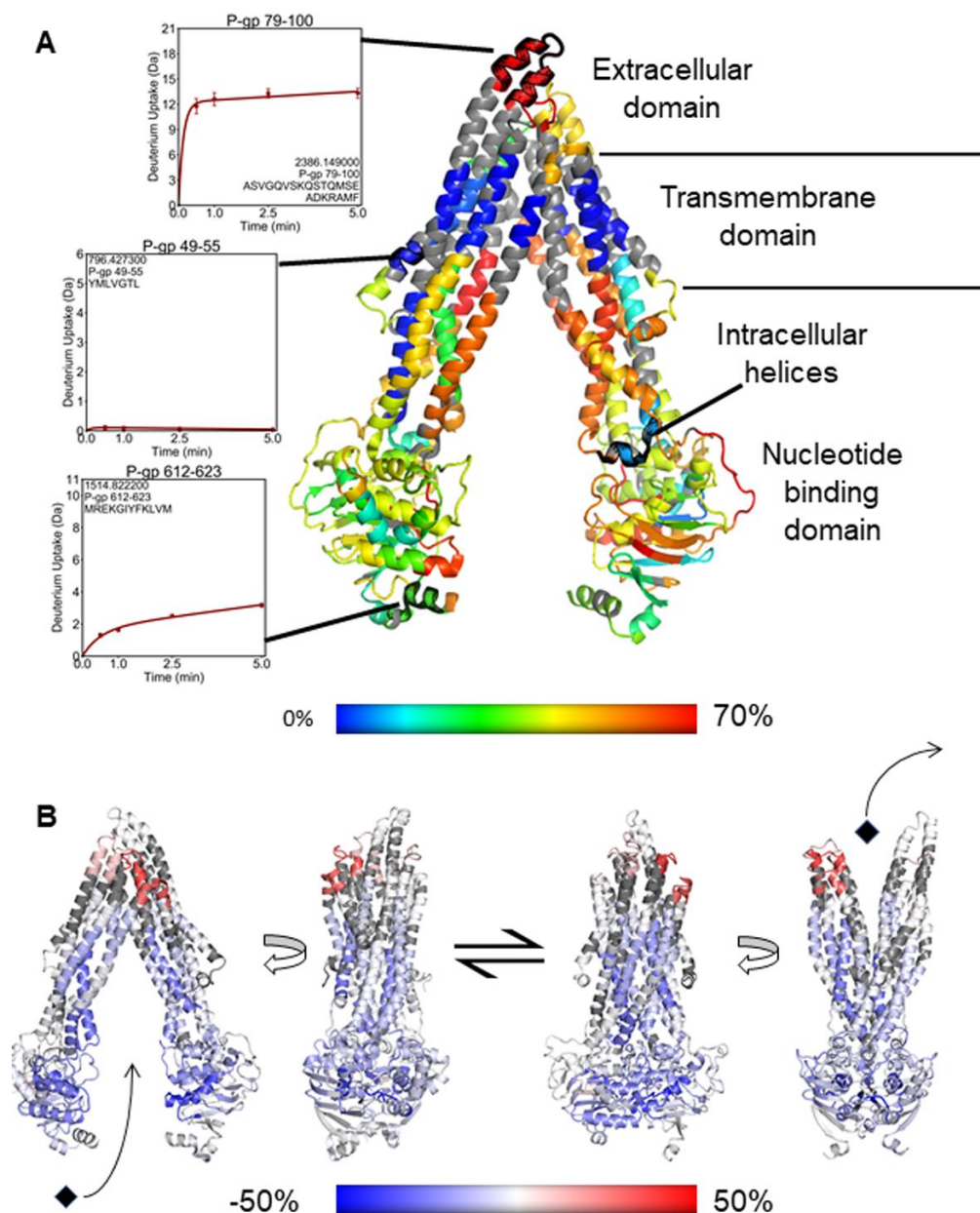
Figure 4.1. Domain architecture of inward and outward-facing P-gp. (**A**) Domain organization of P-gp. HDX-MS data have been mapped on the inward-facing crystal structure of P-gp (8). The model is colored on a rainbow scale from lowest (blue) to highest (red) by relative deuterium uptake of apo P-gp after 5 mins of exchange. Solvent occlusion by the detergent micelle is indicated by low exchange along the transmembrane domain. (**B**) Diagram of the conformational transition between inward and outward-facing states. A homology model based on outward-facing MsbA was used to represent outward-facing P-gp (11). Structures are colored by difference in relative uptake between inward and outward-facing P-gp after 5 mins of exchange. Regions with decreased exchange in the outward-facing state appear blue, while regions with greater exchange are colored red.

66

and result in a conformation with reduced substrate affinity, enabling substrate translocation across the plasma membrane (9). The outward-facing conformation has been observed crystallographically in the homologous bacterial ABC transporters Sav1866 (10) and MsbA (11). Conformational changes associated with NBD dimerization in P-gp have been validated *in vitro* using cysteine cross-linking (12) and fluorescence resonance energy transfer (FRET) (13) experiments. Electron paramagnetic resonance (14) measurements with MsbA and double electron-electron resonance (15) experiments have demonstrated increased dynamics throughout the P-gp EC domain in the outward-facing conformation.

An intermediate conformation between the inward and outward-facing states has also been observed in some transporters. Often referred to as the occluded conformation, this state represents the point at which NBDs have dimerized yet the EC domain opening has not yet occurred (16). The existence of this conformation has been supported by experimental evidence utilizing FRET, cysteine cross-linking and cysteine accessibility to demonstrate a conformation in which NBDs were dimerized while the EC domain remained closed in MsbA (17). The occluded conformation was later observed via crystal structures of the bacterial homologs McjD (18) and PglK (19), and in a cryo-EM structure of MsbA (20).

The transport cycle of P-gp has typically been studied through the use of site-directed mutagenesis and specific ligands which arrest the molecule in various intermediate conformations. The pre-hydrolytic ATP bound state has been stabilized through the addition of non-hydrolyzable ATP analogues (21) and mutations which inhibit ATPase activity (22). The mutation of key catalytic residues within the NBDs (E552Q/E1197Q) was found to stabilize the ATP-bound pre-hydrolytic state by dramatically slowing P-gp catalyzed ATP hydrolysis (23), and these combined mutations were recently used to generate a cryo-EM structure of P-gp bound

to ATP (24). When P-gp carries out ATP hydrolysis in the presence of the orthovanadate ion (VO_4^{-3}), the P-gp molecule becomes trapped in the outward-facing Mg^{+2}-ADP-VO_4^{-3}-bound post-hydrolytic state (25). Orthovanadate trapping stabilizes the hydrolytic transition state by mimicking the γ-phosphate of ATP, and has been used previously to form stable transition state complexes with ATPase enzymes (26).

We have utilized hydrogen-deuterium exchange mass spectrometry (HDX-MS) to interrogate the dynamics of P-gp in three distinct states: apo P-gp (inward-facing), Mg^{+2}-ATP bound to (E552Q/E1197Q) P-gp (pre-hydrolytic), and P-gp bound to Mg^{+2}-ADP-VO_4^{-3} (post-hydrolytic, outward-facing).

B. Materials and Methods

1. P-gp expression and purification

Codon-optimized murine P-gp (Genbank: JF834158) was expressed in *Pichia pastoris* and purified as previously described . Size-exclusion chromatography (Superdex 200 16/60, GE Healthcare) was performed with buffer containing 20 mM HEPES pH 7.5, 100 mM NaCl, 0.035% β-DDM, 0.01% sodium cholate, and 0.2 mM TCEP. Fractions were pooled and stored at 80 °C for HDX-MS analysis.

2. HDX-MS analysis of P-gp

HDX-MS measurements were made using a Synapt G2Si system (Waters Corporation). Deuterium exchange reactions were carried out by a Leap HDX PAL autosampler (Leap Technologies, Carrboro, NC). Deuterated buffer was prepared by lyophilizing 10 mL of 20 mM HEPES pH 7.5, 100 mM NaCl. Lyophilized buffer was resuspended in 10 mL 99.96% D_2O immediately before use, to which was added powdered β-DDM to a final concentration of 0.01%. For measurements of the outward-facing state, the following reagents were added to P-gp

68

samples and D_2O buffer at final concentrations: 5 mM $MgSO_4$, 2 mM sodium orthovanadate and

2 mM ATP. For measurements of the pre-hydrolytic state, 5 mM $MgSO_4$ and 10 mM ATP were

added to (E552Q/E1197Q) P-gp samples and D_2O buffer, as these conditions were found to

induce a NBD-dimerized conformation in a majority of particles observed by cryo-EM (24). In

the apo, pre-hydrolytic, and outward-facing states, control solutions were added to protein

samples and D_2O buffer in order to account for buffer dilution and the addition of H_2O.

Each deuterium exchange time point (0 min, 30 sec, 1 min, 2.5 min, 5 min) was

measured in triplicate. For each measurement, 4 μL of protein was mixed with 36 μL of D_2O

buffer at 25 °C. Deuterium exchange was quenched by combining 35 μL of the deuterated

sample with 65 μL of 0.1% formic acid and 3 M guanidinium-HCl for 1 min at 1 °C. The

quenched sample was then injected in a 50 μL sample loop and digested by an inline pepsin

column (Pierce, Inc.) at 15 °C. Optimization revealed that ideal sequence coverage was obtained

by using a flow rate of 400 μL/sec to capture the resulting peptides on a BEH C4 Vanguard

precolumn. Peptides were then separated by analytical chromatography (Acquity UPLC BEH

C4, 1.7 uM, 1.0 × 50 mm, Waters Corporation) using 7−85% acetonitrile in 0.1% formic acid

over 7.5 min, and then analyzed on a Waters Synapt G2Si quadrupole time-of-flight mass

spectrometer following electrospray injection.

Data were collected in Mobility, ESI + mode, mass acquisition range of 200−2000

(m/z), scan time 0.4 s. Continuous lock mass correction was performed using infusion of leu-

enkephalin (m/z = 556.277) every 30 seconds (mass accuracy of 1 ppm for calibration standard).

For peptide identification, data were instead collected in MS^E (mobility ESI+) mode. Peptide

masses were identified following triplicate analysis of 10 μM P-gp, and the data were analyzed

using PLGS 2.5 (Waters Corporation). Peptides masses were identified using a minimum number

of 250 ion counts for low energy peptides and 50 ion counts for their fragment ions. The following parameters were used to filter peptide sequence matches: minimum products per amino acid of 0.2, minimum score of 7, maximum MH+ error of 5 ppm, and a retention time RSD of 5%, and the peptides had to be present in two of the three ID runs collected. After identification in PLGS, peptides were analyzed in DynamX 3.0 (Waters Corporation). Deuterium uptake for each peptide was calculated by comparing the centroids of the mass envelopes of the deuterated samples with the undeuterated controls. Back-exchange correction factors were applied as previously reported (27). The Y-axis limit for each plot reflects the total number of amides within the peptide that could have possibly exchanged. Each plot includes the peptide MH+ value, sequence, and sequential residue numbering.

3. Binding kinetics

Analysis of binding kinetics were carried out using a ForteBio K2 at 30 °C in P-gp storage buffer. Wild-type and (E552Q/E1197Q) P-gp were biotinylated using EZ-Link NHS-PEG4-Biotin (Thermo Scientific) at a ratio of 1:1. Streptavidin coated biosensors were pre-hydrated in P-gp storage buffer for 15 min and then transferred to microplate wells containing biotinylated P-gp at a concentration of 6 μg/mL for immobilization. Unbound streptavidin molecules were blocked by incubation in 10 μg/mL biocytin for 60 sec, and biosensors were then washed an additional 60 sec in storage buffer. Baseline biolayer interferometry (BLI) measurements were carried out for 90 sec in storage buffer. Association rates were measured by transferring the biosensors to wells supplemented with Mg^{+2} (or Mg^{+2} and Na_3VO_4) and nucleotide for 60 sec. Dissociation was then measured for 180 sec by transferring the biosensors back to the wells used for baseline recording. In the wells used for association measurements, concentrations of Mg^{+2} (or Mg^{+2} and VO_4^{-3}) and nucleotide were maintained at a 1:1 ratio.

Signal due to changing Mg^{+2} and VO_4^{-3} concentrations was subtracted by referencing against buffer supplemented with only Mg^{+2} and VO_4^{-3} without nucleotide. Non-specific binding of ATP to the biosensor surface was subtracted by referencing against biosensors with no P-gp immobilized. Because high concentrations of nucleotide were necessary to obtain a signal, a control experiment was carried out using biotinylated bovine serum albumin to ensure there was no non-specific binding of nucleotide to the immobilized protein. Kinetics data were fitted to a two binding-site model using ForteBio Data Analysis 11.0 and were plotted with Kaleidagraph.

4. ATPase assay

P-gp samples were diluted to give 1 μg per 30 μL in P-gp storage buffer supplemented with 5 mM $MgSO_4$ and 0.1 mg/mL *e. coli*. polar lipids. Verapamil-HCl stock solution was made using the same buffer, and P-gp was incubated with verapamil-HCl or buffer for 15 min on ice. Protein samples (30 μL) and reaction buffer containing 50 mM ATP (1.6 μL) were then transferred to separate wells on a 96-well plate held at 4 °C on a thermocycler. The P-gp samples were added to wells containing ATP using a multichannel pipette and the plate was cycled to 30 °C for 3 min of hydrolysis, then brought to 80 °C for 15 sec to inactivate P-gp and held at 4 °C. Inorganic phosphate liberated by hydrolysis was measured by adding 30 μL of the samples to 150 μL of developing solution prepared by mixing 0.525 g ammonium molybdate in 12.5 mL of 4 M HCl with 17 mg malachite green in 37.5 mL of deionized H_2O and adding 0.1% (v/v) Triton-x 100 to activate. Absorbance was measured at 595 nM on a PerkinElmer 2030 plate reader after 5 min.

C. Results

We carried out HDX-MS on apo P-gp, which has been shown to predominantly occupy the inward-facing conformation (15, 28), pre-hydrolytic (E552Q/E1197Q) P-gp bound to Mg^{+2}-

ATP (23, 24) and outward-facing P-gp stabilized by complexation with Mg^{+2}-ADP-VO_4^{-3} (25). To verify nucleotide binding affinities of both P-gp constructs, binding of Mg^{+2}-ATP and Mg^{+2}-AMPPNP were measured using BLI (Fig. 4.2). In each case, the best fit to the data was obtained by using a two binding-site model, which revealed one site having low micromolar affinity and another in the hundreds of micromolar range, indicating a strong asymmetry in nucleotide binding to each NBD (Table 4.1). Affinity of wild-type P-gp for Mg^{+2}-ADP-VO_4^{-3} also fit to a two binding-site model, though it could not be determined whether the VO_4^{-3} ion was present at both sites. The measured affinities in this case were approximately 10-fold tighter than when measured in the absence of VO_4^{-3}, also in agreement with previous findings (29). Despite similar binding kinetics, the mutant (E552Q/E1197Q) P-gp was verified as showing no verapamil-stimulated ATPase activity (Fig. 4.3) (23).

Our HDX-MS data covered 85.8% of the P-gp sequence in 86 different peptides. Deuterium uptake was measured at time intervals up to 5 min of incubation in deuterated buffer at 25 °C, as these conditions were recently shown to reveal native state protein dynamics that occur in the μs-ms range (30). Fractional deuterium uptake into apo P-gp was mapped onto the crystal structure of mouse P-gp (8) providing a measure of dynamics occurring throughout the transporter (Fig. 4.1A). In order to contextualize differences in conformational dynamics between the inward and outward-facing states, we compared deuterium uptake between apo P-gp and outward-facing P-gp. Differences of more than 0.5 Da were interpreted as significant. The difference in uptake between the inward-facing, pre-hydrolytic and outward-facing states were mapped on models which yielded the best structural fit to our data.

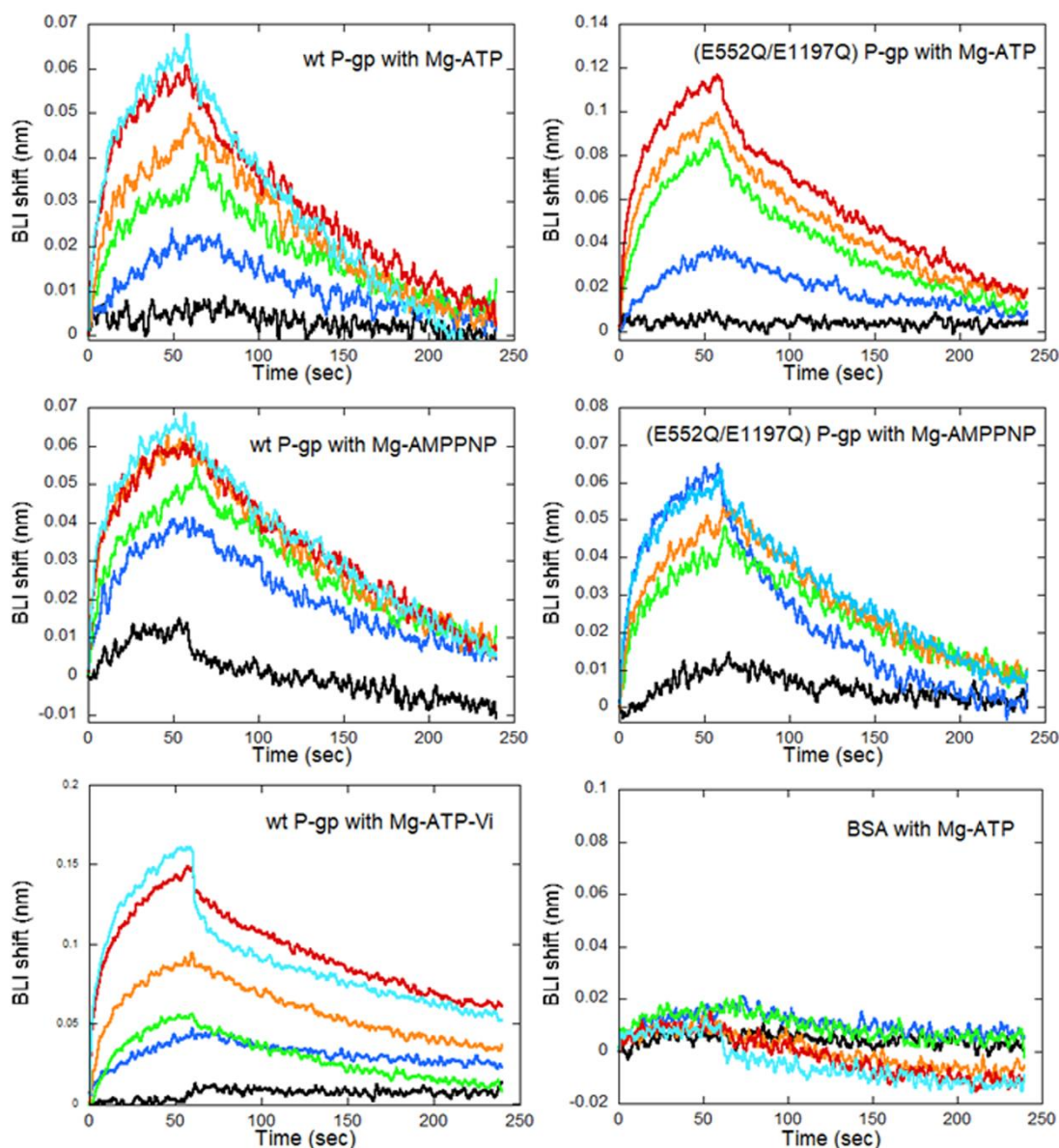**Figure 4.2. Nucleotide binding kinetics.** Binding kinetics resulting from BLI experiments are summarized. Both mutant and wild-type P-gp displayed similar affinities for ATP and AMPPNP. Wild-type P-gp binding to Mg^{+2}-ATP in the presence of VO_4^{-3} was approximately 10-fold tighter. Concentrations are 1.6 (black), 8 (blue), 40 (green), 200 (orange), 1000 (red) and 5000 (cyan) μM.

73

Table 4.1. Binding kinetics between P-gp and nucleotide molecules.

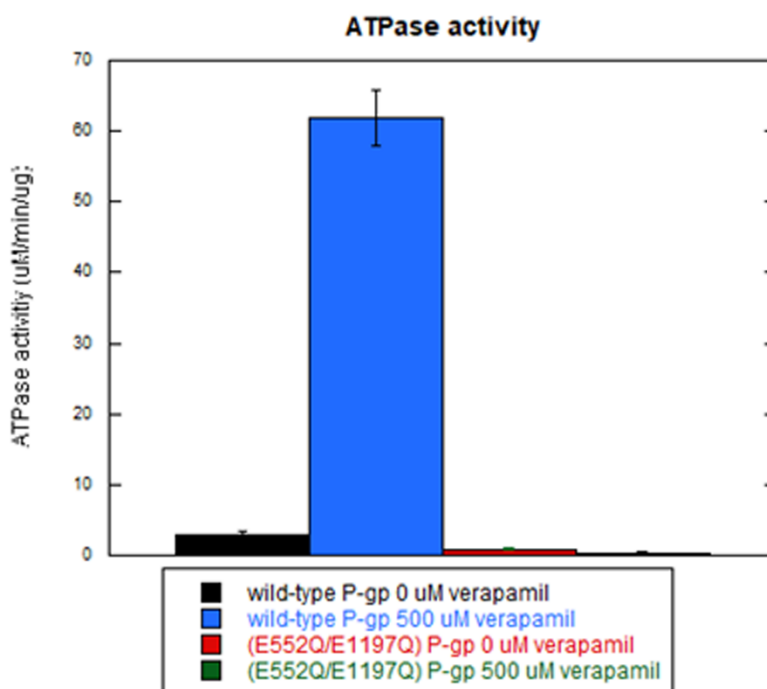|	K_{D1} ($\times 10^{-6}$ M)	K_{D2} ($\times 10^{-6}$ M)	K_{on1} ($\times 10^{3}*1/$Ms)	K_{on2} ($\times 10*1/$Ms)	K_{off1} ($\times 10^{-3}*1/$s)	K_{off2} ($\times 10^{-3}*1/$s)	Full R^2
P-gp with Mg^{+2}-ATP	3.2 ± 0.3	210 ± 20	3.0 ± 0.2	6.5 ± 0.7	9.4 ± 0.3	13.5 ± 0.8	0.92
(E552Q/E1197) P-gp with Mg^{+2}-ATP	2.2 ± 0.2	220 ± 20	4.7 ± 0.3	4.4 ± 0.4	10.3 ± 0.3	9.7 ± 0.6	0.91
P-gp with Mg^{+2}-AMPPNP	2.5 ± 0.1	550 ± 20	3.4 ± 0.1	1.7 ± 0.4	8.6 ± 0.2	9.5 ± 1.6	0.90
(E552Q/E1197) P-gp with Mg^{+2}-ATP	2.9 ± 0.3	190 ± 40	2.7 ± 0.2	5.9 ± 1.1	7.6 ± 0.3	11.2 ± 1.3	0.91
P-gp with Mg^{+2}-ADP-VO_4^{-3}	0.9 ± 0.1	70 ± 3	5.8 ± 0.4	7.3 ± 0.2	5.5 ± 0.2	5.2 ± 0.2	0.95

Figure 4.3. Verapamil-stimulated ATPase assay. ATPase activity of wild-type P-gp was enhanced by the substrate transport verapamil, while (E552Q/E1197Q) P-gp was insensitive to verapamil.

1. Transmembrane domain

The linker connecting both halves of P-gp has not been observed in three-dimensional structures. Contrary to the fast exchange expected for an unstructured region, deuterium uptake into the linker sequence (covered by peptides corresponding to residues 619–630, 631–658 and 659–684) was not complete even after 5 min of exchange. These results suggest that the linker may either possess some degree of secondary structure, as hypothesized previously (31), or that it contacts other surfaces of the transporter. The linker showed no measurable differences between the three experimental states of P-gp.

In all three experimental states, a band of non-exchanging amides was observed around the transmembrane helices (TMHs) which most likely marks the region of the TMHs covered by the detergent micelle (Fig. 4.1A). The only TM regions which showed little deuterium incorporation outside of the detergent band were found in TM2 (residues 132–152) and TM8 (residues 767–780 and 790–799), which run along the outer sides of the transporter (Fig. 4.4).
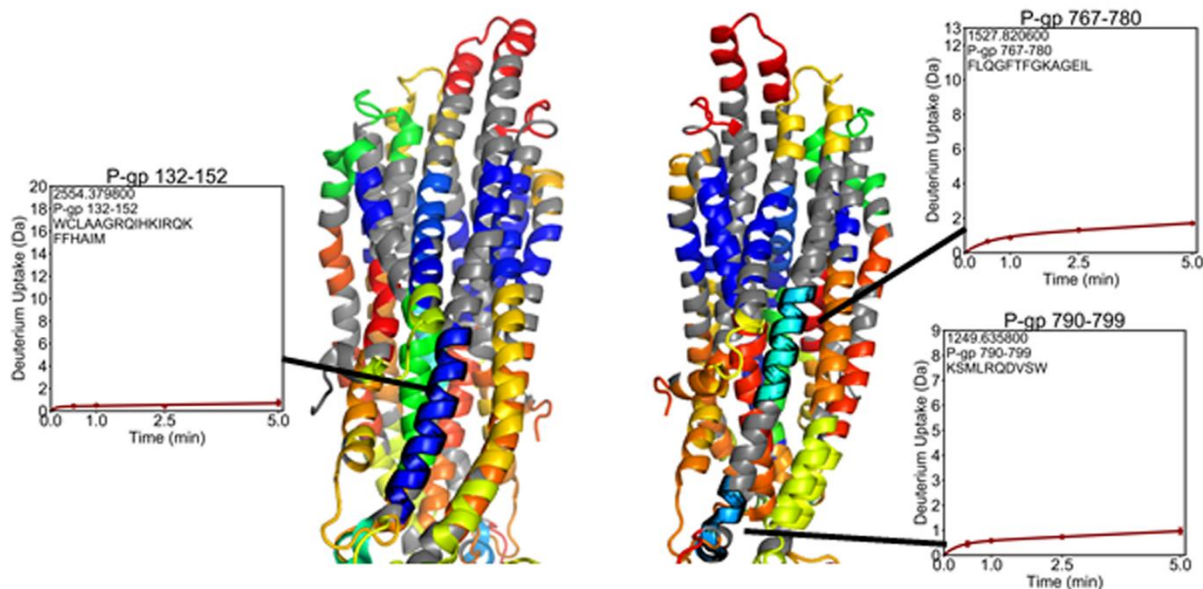
Figure 4.4. Non-exchanging transmembrane helices. Deuterium uptake plots for regions of TM2 and TM8. These helices are centered along the sides of the transporter, and are the only TMHs which displayed low uptake outside the detergent band.

One peptide from TM4 (residues 216–223) incorporated deuterium despite being located along the non-exchanging band (Fig. 4.5). This dynamic segment of TM4 had lower exchange in the (E552Q/E1197Q) mutant than in wild-type P-gp, and both the pre-hydrolytic and outward-facing states showed lower exchange compared to the apo states. On the opposite side of the transporter, TM10 (residues 858–865) is in an analogous position but exhibited the same complete protection observed for the rest of the non-exchanging band. Regions of TMHs which comprise the substrate-binding cavity (residues 56–68, 168–188, 216–223, 280–299, 340–350, 811–829, 916–937, and 991–1016) showed increasing deuterium incorporation over time, indicative of slow dynamic processes. Portions of TMHs on the intracellular side of the transporter showed decreased exchange in both the pre-hydrolytic and outward-facing states, consistent with TMH bundling that accompanies NBD dimerization (Fig. 4.6).

76
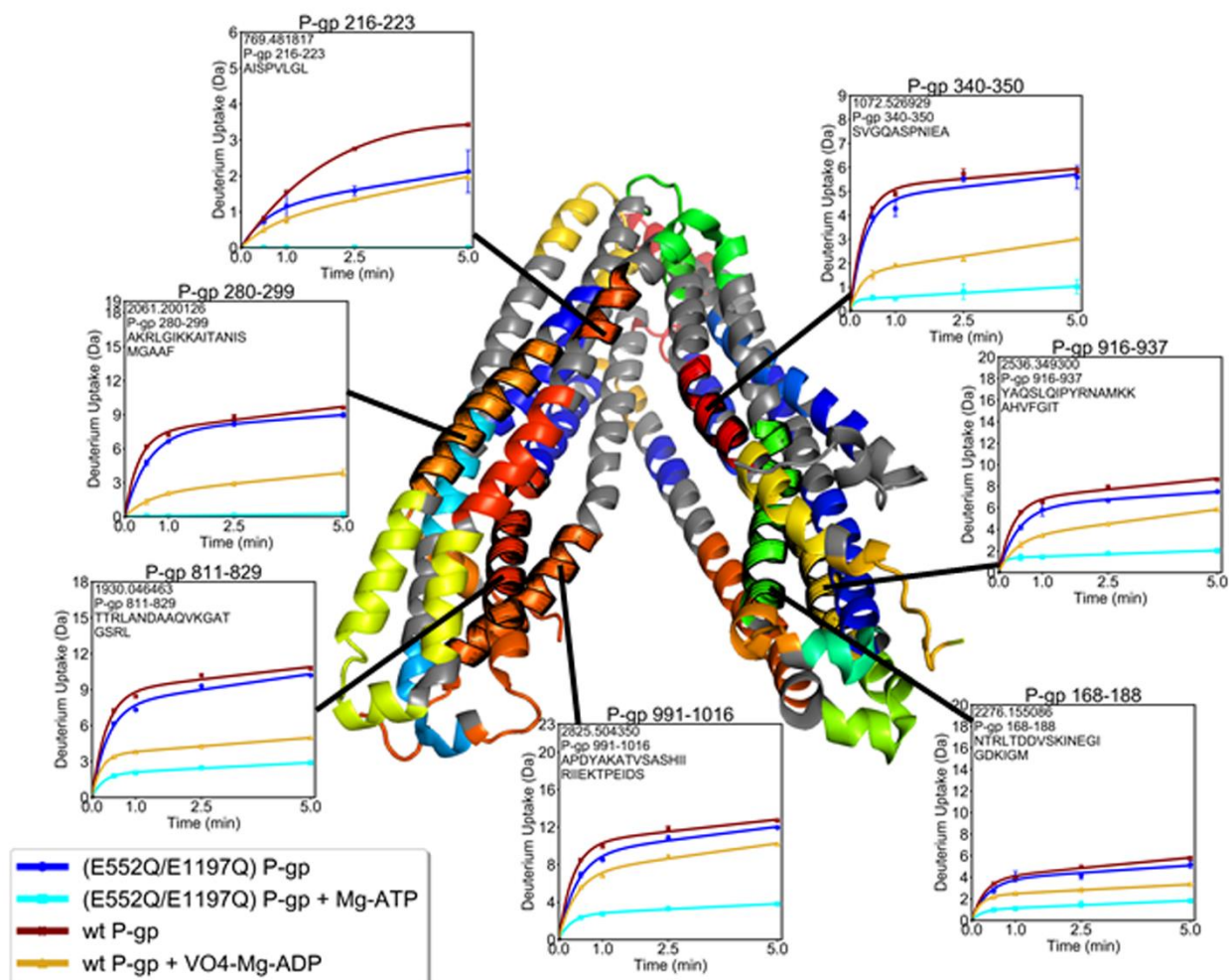
Figure 4.5. Slowly exchanging substrate binding pocket. Deuterium uptake plots for the TMHs comprising the polyspecific binding pocket. All regions display increasing uptake over time, indicative of ongoing dynamic processes throughout this region. TM4 (residues 216–223) is the only region within the detergent band that exchanged with deuterium.

Figure 4.6. Decreased exchange throughout the transmembrane domain. Inner TM helices which group together following NBD dimerization all decreased exchange in both pre-hydrolytic (**A**) and outward-facing (**B**) states.
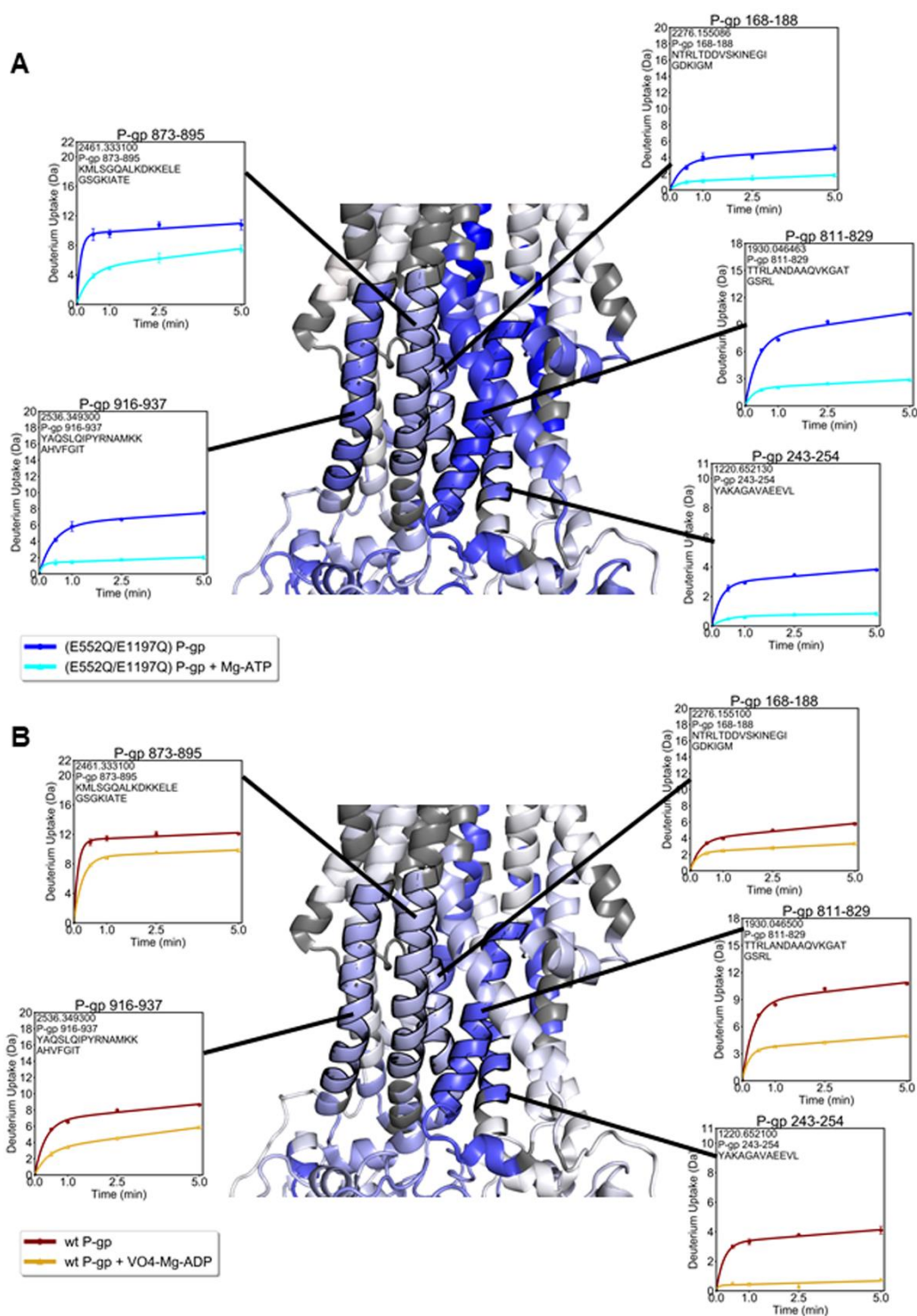
2. Nucleotide binding domains

Within the NBDs, all conserved ATP binding motifs became more protected from exchange in both the pre-hydrolytic and outward-facing states (Fig. 4.7). Although previous HDX-MS studies of P-gp showed some evidence of EX1 kinetics within the NBDs, the phenomenon was mainly present in nanodisc-embedded P-gp and hardly observable in detergent-solublized preparations (32). Our results are consistent with this previous work.
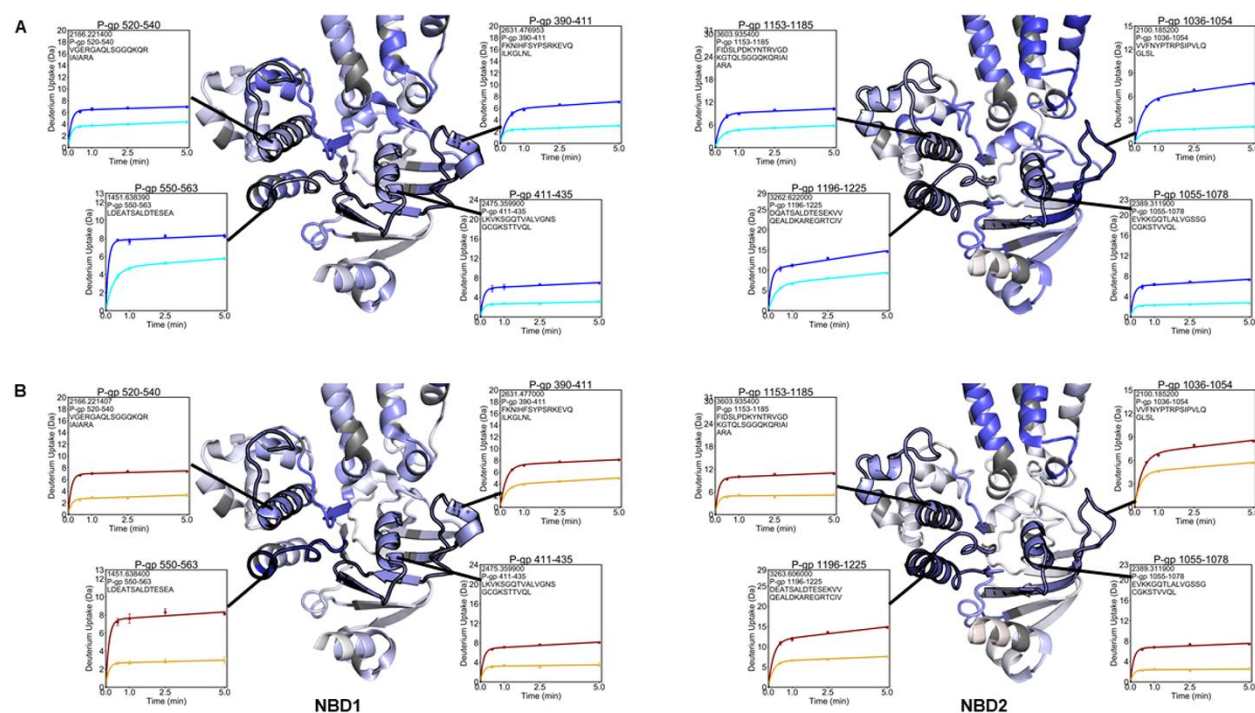
Figure 4.7. Decreased exchange in both nucleotide binding domains.
Conserved ABC transporter motifs and regions which contact nucleotide from both NBDs decreased exchange in the pre-hydrolytic and outward-facing states.

Each NBD contacts one pair of intracellular helices (ICHs). In the pre-hydrolytic state, all surfaces contacting ICHs in NBD1 (residues 363–374, 436–446, 465–475, and 480–493) and NBD2 (residues 1004–1016, 1079–1091, 1092–1105, 1123–1138) had decreased exchange (Fig. 4.8A). In the outward-facing state, all NBD1 regions contacting ICHs showed decreased exchange, while only the peptide corresponding to residues 1123–1138 decreased exchange by more than 0.5 Da in NBD2 (Fig. 4.8B).
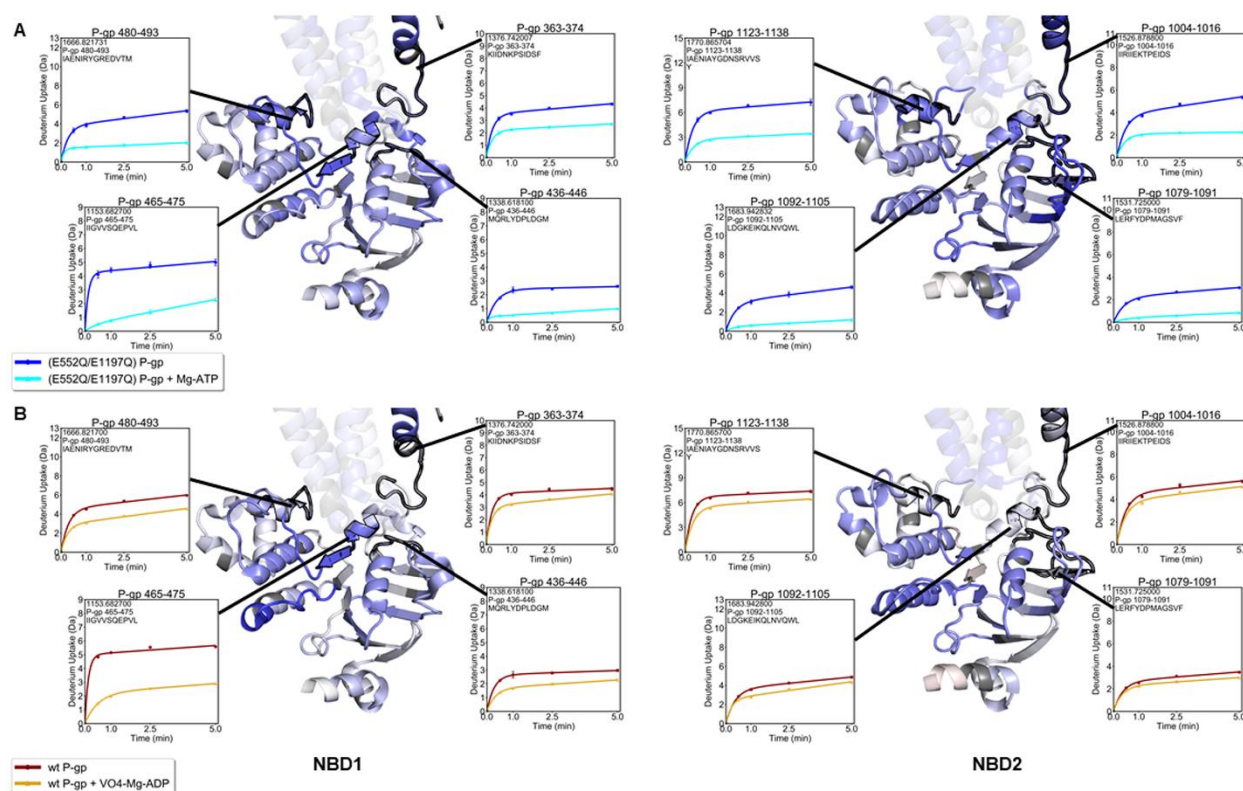
Figure 4.8. Decreases in exchange among nucleotide binding domain regions contacting intracellular helices. (**A**) All regions contacting ICHs from both NBDs decreased exchange in the pre-gydrolytic state. (**B**) In the outward-facing state, every region contacting ICHs on NBD1 decreased exchange by more than 0.5 Da. Only the peptide containing residues 1123–1138 showed decreased exchange in NBD2.
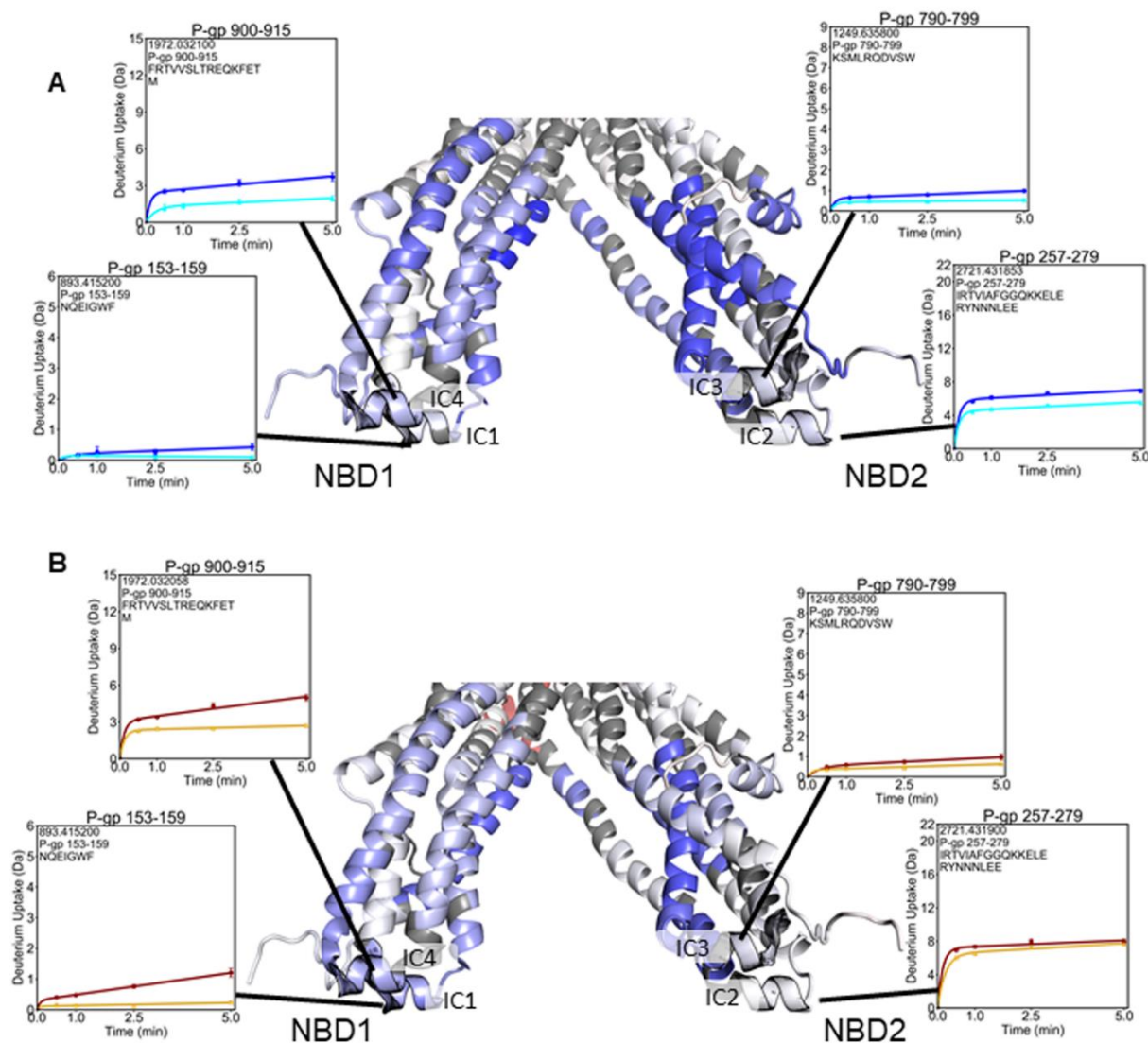
Figure 4.9. Decreases in exchange among intracellular helices. (**A**) In the pre-hydrolytic state, ICH4 contacting NBD1 and ICH2 contacting NBD2 showed decreased exchange. (**B**) In the outward-facing state, both ICHs contacting NBD1 showed reduced exchange, while the ICHs at the NBD2 interface did not.

Among the ICHs, one ICH contacting NBD1 (IC4: residues 900–915) and one ICH

contacting NBD2 (IC2: residues 257–279) showed reduced exchange in the pre-hydrolytic state

(Fig. 4.9A). In the outward-facing state, both ICHs contacting NBD1 (IC1: residues 153–159,

and IC4) showed reduced exchange whereas deuterium incorporation into the ICH pair that interfaces with NBD2 (IC2, and IC3: residues 790–799), was unchanged (Fig. 4.9B).

3. Extracellular domain

The EC domain is comprised of six loops between TMH pairs, and it showed dramatically different changes in the pre-hydrolytic and outward-facing conformations. In the pre-hydrolytic state, EC1 (residues 79–100), EC5 (residues 848–855), and EC6 (residues 959–966) showed reduced uptake (Fig. 4.10A) While in the outward-facing state, EC2 (residues 201–212), EC3 (residues 316–328), EC4 (residues 729–850) and EC6 incorporated deuterium more rapidly (Fig. 4.10B).
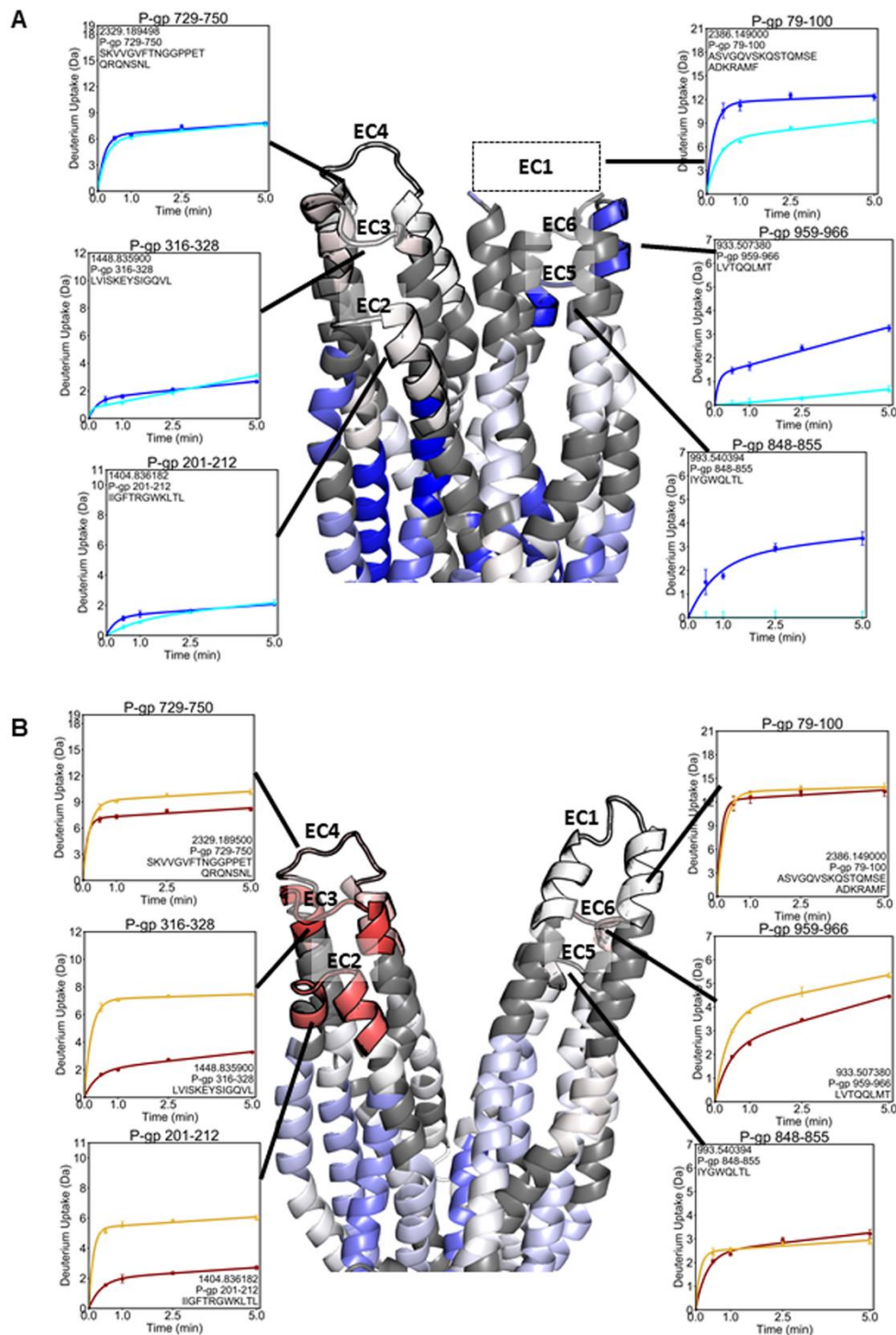
Figure 4.10. Perturbations to exchange throughout the extracellular domain.
Deuterium uptake plots reveal the dynamics of the EC domain. (**A**) A cryo-EM
structure of (E552Q/E1197Q) P-gp obtained under similar experimental
conditions provided the best fit to our HDX-MS data (24). Decreased exchange
was evident among ECL1, 5 and 6 in the pre-hydrolytic state. (**B**) In outward-
facing P-gp, increased exchange was found among ECL 2, 3, 4 and 6.

D. Discussion

The high sequence coverage we obtained provided a comprehensive picture of P-gp dynamics in the apo, pre-hydrolytic and outward-facing states. A substantial reduction in deuterium exchange was observed within the NBDs in the pre-hydrolytic and outward-facing states compared to the inward-facing apo state, implying that the two binding sites were occupied by nucleotide in both states (Fig. 4.7). These results agree with previous findings that two molecules of ATP were observed bound to P-gp in a cryo-EM structure (24). In addition, our BLI measurements revealed two binding affinities as did previous studies of Chinese hamster P-gp binding to the non-hydrolyzable ATP analogue ATP-γ-S, which revealed that when one NBD occludes nucleotide with relatively tight affinity (KD: 4 μM), the other NBD also remains associated with nucleotide, albeit more weakly (KD: 740 μM) (Fig 4.2, Table 4.1) (33).

Consistent with expectations, a region of low exchange due to solvent exclusion by the detergent micelle was represented by a band of complete protection found along the TMHs (Fig. 4.1A). This region corresponds to the location of the membrane as determined computationally and by atomic force microscopy of P-gp reconstituted in a phospholipid bilayer (34). Cryo-EM structures generated using P-gp solubilized with the same detergent employed here also showed the presence of a detergent corona around this region (28, 35).

Two helices (TM2 and TM8), located on opposite sides of the transporter and sandwiched between surrounding TMHs, were the only regions that were protected from exchange outside of the detergent band (Fig. 4.4). The most likely reason for their low exchange is tight packing with neighboring TMHs, which may restrain dynamic motions necessary for deuterium exchange to occur. These TMHs also did not show any difference in uptake between

the three experimental states, suggesting that the dynamics of TM2 and TM8 remain unchanged as P-gp alternates between inward and outward-facing conformations.

Surprisingly, one segment of TM4 (residues 216–223), despite being located along the detergent band, showed relatively high deuterium exchange (Fig. 4.5). In addition, the (E552Q/E1197Q) mutations in the NBDs were sufficient to reduce deuterium incorporation into this segment, which is over 80 Å away. Exchange within this region was also reduced in the pre-hydrolytic and outward-facing states. These results suggest that this portion of TM4 responds to changes in the NBDs and plays a key role in conformational transitions. Furthermore, it appears that the ATPase inhibitory (E552Q/E1197Q) mutation induces long-distance stabilizing effects even in the absence of ligands. Conformational heterogeneity has previously been noted within this region, where a study of P-gp crystal structures bound to various ligands noted different conformations of this region with the finding that ATPase-stimulating ligands induced a structural change in TM4 between residues 219–243, while binding of ATPase inhibitors resulted in a more rigid structural reorganization (7).

The polyspecific substrate binding pocket located within the TM domain showed increasing exchange over time (Fig. 4.5), indicating mobility throughout the TMHs that comprise this pocket. These exchange profiles resulted from amides that were gradually exposed as the transporter sampled a range of conformations over a range of time scales. It is likely that these dynamics contribute to the substrate promiscuity that is a hallmark characteristic of P-gp (36). These results confirm predictions that the polyspecific binding pocket is highly dynamic, underscoring the mobility of the P-gp molecular machine.

Two ICHs nestle into hydrophobic clefts in each NBD, forming highly conserved interfaces that have been shown to be crucial for P-gp ATPase activity (37, 38). Unlike the

similar reductions in exchange observed at the nucleotide binding sites, the two ICH-NBD interfaces displayed asymmetric changes in dynamics. In the pre-hydrolytic state, all NBD regions contacting ICHs decreased exchange (Fig.4.8A). In the outward-facing state, every region in NBD1 contacting ICHs decreased exchange while only one portion of NBD2 contacting ICHs decreased exchange (Fig. 4.8B). At the opposite side of this interface, one ICH contacting each NBD showed lower deuterium exchange in the pre-hydrolytic state (Fig. 4.9A). All ICH regions that contact NBD1 showed reduced exchange in the outward-facing state, while none of the ICHs contacting NBD2 decreased exchange (Fig. 4.9B). Similar results demonstrating reduced uptake at the ICH-NBD1 interface in the outward-facing conformation and no change at the ICH-NBD2 site were obtained in another HDX-MS study of P-gp (32), although coverage of this region was incomplete in the previous work. These results suggest coordinated conformational motions that occur sequentially to move P-gp through a range of conformations.

The EC domain, composed of six loops between TMHs, underwent remarkably different changes in dynamics in the pre-hydrolytic and outward-facing states. We observed that three of the ECLs along the face of the molecule defined by TM10 decreased exchange in the pre-hydrolytic state (Fig. 4.10A). In contrast, in the outward-facing conformation, three of the ECLs along the side defined by TM4 and one ECL on the TM10 side had increased exchange (Fig. 4.10B). It is interesting to note that the decrease in exchange in the TMHs following NBD dimerization is similar to the decrease in exchange in the EC domain in the pre-hydrolytic state strongly suggesting the entire molecule is occluded in the pre-hydrolytic state (Fig. 4.6). In contrast, our results clearly show that the outward-facing state has increased ECL dynamics. EC domain opening has been observed structurally (10, 11) and EC domain flexibility was suggested

by the observed heterogeneity of the EC region in cryo-EM (24) and by intramolecular distances determined from spin-labeling (15). Our HDX-MS results imply that the intermediate pre-hydrolytic state is occluded from both the IC and EC environments simultaneously, and they suggest a mechanism by which both substrate entry and exit points are occluded, preventing temporary channel formation during transport.

Our results provided unprecedented HDX-MS coverage of P-gp, enabling a comprehensive view of dynamics in three distinct conformational states. Decreased exchange in the NBDs reflects the NBD dimerization that occurs following nucleotide binding. The asymmetric perturbations at the two ICH-NBD interfaces suggest that the two pseudosymmetric halves of the molecule function differently from one another with regard to dynamics. However, similar nucleotide binding kinetics measured for wild-type and (E552Q/E1197Q) P-gp indicate that these perturbations do not impact overall nucleotide affinity. High dynamics of the substrate-binding pocket in the TM domain implies conformational flexibility that likely promotes substrate promiscuity, while lower than expected dynamics of the linker indicate that the linker may possess some secondary structure.

The most striking observation, however, was the difference in deuterium uptake of the ECLs between the apo, pre-hydrolytic, and outward-facing states. In the pre-hydrolytic state, the dynamics in this region decreased while the same region increased dynamics in the outward-facing state when compared to apo P-gp. These findings indicate a mechanism which prevents the transporter from behaving as a channel during the intermediate transition between the inward-facing and outward-facing states. Our findings suggest that this occluded conformation occurs at the ATP bound pre-hydrolytic stage of transport, and they characterize P-gp as a highly

dynamic machine undergoing multiple correlated motions to drive substrate translocation while avoiding leakage.

Chapter IV, in part, is a reprint of which the dissertation author was the principal researcher and author. The material appears in *Nature Scientific Reports*. (**Kopcho, N.**, Chang, G., Komives, E.A. (2019) "Dynamics of ABC transporter P-glycoprotein in three conformational states" *Sci. Rep.* **9**: 10592.)

E. References

1. Juliano RL & Ling V (1976) A Surface Glycoprotein Modulating Drug Permeability in Chinese Hamster Ovary Cell Mutants. *Biochim. Biophys. Acta* 455:152-162.

2. Riordan JR, Deuchars K, Kartner N, Alon N, Trent J, & Ling V (1985) Amplification of P-glycoprotein genes in multidrug-resistant mammalian cell lines. *Nature* 316:817-819.

3. van Assema DME & van Berckel BNM (2016) Blood-Brain Barrier ABC-transporter P-glycoprotein in Alzheimer's Disease: Still a Suspect? *Curr. Pharm. Des.* 22:5808-5816.

4. Wilkens S (2015) Structure and mechanism of ABC transporters. *F1000 Prime Rep.* 7:14.

5. Aller SG, Yu J, Ward A, Weng Y, Chittaboina S, Zhuo R, Harrell P, Trinh YT, Zhang Q, Urbatsch IL, & Chang G (2009) Structure of P-Glycoprotein Reveals a Molecular Basis for Poly-Specific Drug Binding. *Science* 323:1718-1722.

6. Ward AB, Szewczyk P, Grimard V, Lee CW, Martinez L, Doshi R, Caya A, Villaluz M, Pardon E, Cregger C, Swartz DJ, Falson PG, Urbatsch IL, Govaerts C, Steyaert J, & Chang G (2013) Structures of P-glycoprotein reveal its conformational flexibility and an epitope on the nucleotide-binding domain. *PNAS* 2013:13386-13391.

7. Szewczyk P, Tao H, McGrath AP, Villaluz M, Rees SD, Lee SC, Doshi R, Urbatsch IL, Zhang Q, & Chang G (2015) Snapshots of ligand entry, malleable binding and induced helical movement in P-glycoprotein. *Acta Cryst. D* D71:732-741.

8. Nicklisch SCT, Rees SD, McGrath AP, Gokirmak T, Bonito LT, Vermeer LM, Cregger C, Loewen G, Sandin S, Chang G, & Hamodun A (2016) Global marine pollutants inhibit

P-glycoprotein: Environmental levels, inhibitory effects, and cocrystal structure. *Sci. Adv.* 2:e1600001.

9.   Seeger MA & van Veen HW (2009) Molecular basis of multidrug transport by ABC transporters. *Biochim. Biophys. Acta* 1794:725-737.

10.   Dawson RJP & Locher KP (2006) Structure of a bacterial multidrug ABC transporter. *Nature* 443:180-185.

11.   Ward A, Reyes CL, Yu J, Roth CB, & Chang G (2007) Flexibility in the ABC transporter MsbA: Alternating access with a twist. *PNAS* 104:19005-19010.

12.   Loo TW, Bartlett MC, & Clarke DM (2003) Drug Binding in Human P-glycoprotein Causes Conformational Changes in Both Nucleotide-binding Domains. *J. Biol. chem.* 278:1575-1578.

13.   Verhalen B, Ernst S, Borsch M, & Wilkens S (2012) Dynamic Ligand-induced Conformational Rearrangements in P-glycoprotein as Probed by Fluorescence Resonance Energy Transfer Spectroscopy. *J. Biol. chem.* 287:1112-1127.

14.   Dong J, Yang G, & Mchaourab HS (2005) Structural Basis of Energy Transduction in the Transport Cycle of MsbA. *Science* 308:1023-1028.

15.   Verhalen B, Dastvan R, Thangapandian S, Peskova T, Koteiche HA, Nakamoto RK, Tajkhorshid E, & Mchaourab HS (2017) Energy transduction and alternating access of the mammalian ABC transporter P-glycoprotein. *Nature* 543:738-742.

16.   Subramaniam N, K. C-J, & O'mara ML (2016) Structural and Dynamic perspectives on the promiscuous transport activity of P-glycoprotein. *Neurochem. Int.* 98:146-152.

17.   Doshi R & Van Veen HW (2013) Substrate Binding Stabilizes a Pre-translocation Intermediate in the ATP-binding Cassette Transport Protein MsbA. *J. Biol. chem.* 288:21638-21647.

18.   Chowdhury HG, Tong Z, Mathavan I, Li M, Itawa S, Zirah S, Rebuffat S, Van Veen HW, & Beis K (2014) Structure of an antibacterial peptide ATP-binding cassette transporter in a novel outward occluded state. *PNAS* 111:9145-9150.

19.   Perez C, Gerber S, Boilevin J, Bucher M, Darbre t, Aebi M, Reymond JL, & Locher KP (2015) Structure and mechanism of an active lipid-linked oligosaccharide flippase. *Nature* 524:433-438.

20.   Mi W, Li Y, Yoon SH, Ernst RK, Walz T, & Liao M (2017) Structural basis of MsbA-mediated lipopolysaccharide transport. *Nature* 549:233-237.

21. Senior AE, Al-Shawi MK, & Urbatsch IL (1995) The catalytic cycle of P-glycoprotein. *FEBS Lett* 377:285-289.

22. Sauna ZE, Muller M, Peng XH, & Ambudkar SV (2002) Importance of the Conserved Walker B Glutamate Residues, 556 and 1201, for the Completion of the Catalytic Cycle of ATP Hydrolysis by Human P-glycoprotein (ABCB1). *Biochemistry* 41:13989-14000.

23. Tombline G, Bartholomew LA, Urbatsch IL, & Senior AE (2004) Combined Mutation of Catalytic Glutamate Residues in the Two Nucleotide Binding Domains of P-glycoprotein Generates a Conformation That Binds ATP and ADP Tightly. *J. Biol. chem.* 279:31212-31220.

24. Kim Y. & J. C (2018) Molecular structure of human P-glycoprotein in the ATP-bound, outward-facing conformation. *Science* 10.1126/science.aar7389.

25. Urbatsch IL, Al-Shawi MK, & Senior AE (1994) Characterization of the ATPase Activity of Purified Chinese Hamster P-glycoprotein. *Biochemistry* 33:7069-7076.

26. Smith CA & Rayment I (1996) X-ray Structure of the Magnesium(II) -ADP-Vanadate Complex of the Dictyostelium discoideum Myosin Motor Domain to 1.9 Å Resolution. *Biochemistry* 35:5404-5417.

27. Narang D, Chen W, Ricci CG, & Komives EA (2018) RelA-Containing NFkB Dimers Have Strikingly Different DNA-Binding Cavities in the Absence of DNA. *J. Mol. Biol.* 430:1510-1520.

28. Frank GA, Shukla S, Rao P, Borgnia MJ, Bartesaghi A, Merk A, Mobin A, Esser L, Earl LA, Gottesman MM, Xia D, Ambudkar SV, & Subramaniam S (2016) Cryo-EM Analysis of the Conformational Landscape of Human P-glycoprotein (ABCB1) During its Catalytic Cycle. *Mol. Pharmacol.* 90:35-41.

29. Li MJ, Nath A, & Atkins WM (2017) Differential Coupling of Binding, ATP Hydrolysis, and Transport of Fluorescent Probes with P-glycoprotein in Lipid Nanodiscs. *Biochemistry* 56:2506-2517.

30. Markwick PRL, Peacock RB, & Komives EA (2018) Accurate Prediction of Amide Exchange in the Fast Limit Reveals Thrombin Allostery. *Biophys. J.* 116:49-56.

31. Hrycyna CA, Airan LE, Germann UA, Ambudkar SV, Pastan I, & Gottesman MM (1998) Structural Flexibility of the Linker Region of Human P-Glycoprotein Permits ATP Hydrolysis and Drug Transport. *Biochemistry* 37:13660-13673.

32. Li MJ, Guttman M, & Atkins WM (2018) Conformational dynamics of P-glycoprotein in lipid nanodiscs and detergent micelles reveal complex motions on a wide time scale. *J. Biol. chem.*:6297-6307.

33.   Mehmood S, Doumene C, Forest E, & Jault JM (2012) Dynamics of a bacterial multidrug ABC transporter in the inward- and outward-facing conformations. *PNAS* 109:10832-10836.

34.   Sigdel KP, Wilt LA, Marsh BP, Roberts AG, & King GM (2018) The conformation and dynamics of P-glycoprotein in a lipid bilayer investigated by atomic force microscopy. *Biochem. Pharmacol.* 156:302-311.

35.   Thonghin N, Collins RF, Barbieri A, Shafi T, Siebert A, & Ford RC (2018) Novel features in the structure of P-glycoprotein (ABCB1) in the posthydrolytic state as determined at 7.9Å resolution. *bioRxiv* Apr. 25, 2018.

36.   Gutmann DAP, Ward A, Urbatsch IL, Chang G, & van Veen HW (2009) Understanding polyspecificity of multidrug ABC transporters: closing in on the gaps in ABCB1. *Trends Biochem. Sci.* 35:36-42.

37.   Jin MS, Oldham ML, Zhang Q, & Chen J (2012) Crystal structure of the multidrug transporter P-glycoprotein from Caenorhabditis elegans. *Nature* 490:566-570.

38.   Loo TW & Clarke DM (2015) The Transmission Interfaces Contribute Asymmetrically to the Assembly and Activity of Human P-glycoprotein. *J. Biol. Chem.* 290:16954-16963.

Chapter V:

In vitro Discovery of Camelid Antibody

Fragments

A. Introduction

Antibodies (Abs) are widely used in the biosciences for many purposes from imaging to therapeutics. Currently, the global Ab market value is projected to approach $9.5 billion by the year 2024 (1). Yet despite their prolific usage, Abs possess several undesirable characteristics. Foremost, ~90% of the mass of an Ab molecule is composed of a large immunoglobulin domain which does not contribute toward antigen binding and inhibits tissue penetration (2). Due to this, high concentrations of Abs are generally required for therapeutic efficacy. This is especially problematic because Abs are poorly expressed in prokaryotic systems, and production of adequate amounts of therapeutic Abs remains an expensive and laborious process (3).

The tetrameric architecture of Abs may often lead to a range of stability issues (4). The interface between variable domains of heavy (V_H) and light (V_L) monomeric chains comprises the antigen-binding region, with three loops from each chain contributing to the binding interface. This complexity may pose difficulties for Ab engineering or generation of synthetic libraries. One alternative is a fusion of V_H and V_L domains, termed the single-chain variable fragment (scFv). While scFvs have led to some clinical successes, they require synthetic linker regions and are prone to misfolding (5). Further, scFvs possess the same complex binding domain as full-length Abs and all the difficulties associated therewith.

Camelid ab fragments have recently emerged as a promising alternative to classical Abs (6). Camelids and some cartilaginous fish Abs share a unique single-chain domain architecture with compact antigen-binding variable (V_{HH}) domains. The isolated V_{HH} domain expresses very well in prokaryotic systems and is highly stable in comparison to full-length Abs and scFcvs. Due to its ~2 nm oblong shape, the V_{HH} domain is commonly referred to as a nanobody (Nb). Nbs possess a three-loop antigen-binding region that is conducive to library generation. The Nb

antigen-binding region also forms a unique convex architecture, which facilitates binding to active sites and provides Nbs with excellent utility as enzymatic modulators (7, 8).

One drawback both systems share is that discovery of new Abs and Nbs typically requires live animal immunization. This is an expensive and time-consuming process, and antigen toxicity severely limits the range of molecules that may be targeted. To circumvent these problems, we have leveraged the prokaryotic genetic encodability of Nbs to develop an *in vitro* discovery platform which allows discovery of novel Nbs in a matter of days using only benchtop equipment. Our platform utilizes the rapid growth of *e. coli* and the high-throughput screening power of fluorescence activated cell sorting (FACS) to screen a diverse ($>10^9$) synthetic Nb library for binders against specific antigens. As a proof of concept, we generated a low nM affinity (28 nM) Nb against the multidrug efflux transporter P-glycoprotein (P-gp) within a matter of days.

B. Materials and Methods

1. Protein production

P-gp was prepared as described previously (9) and stored in buffer containing 20mM HEPES pH 7.5, 100 mM NaCl, 0.035% β-DDM, 0.01% sodium cholate, and 0.2 mM TCEP.

Nb protein was purified directly from the cell surface display system. Cultures were grown in 1 L flasks containing lysogeny broth (LB) media supplemented with 50 µg/mL kanamycin at 37˚C. Cell surface displayed Nb expression was induced with addition of arabinose to a final concentration of 0.2% when optical density at 600 nm reached ~0.5. Cells were harvested by centrifugation at 5000 xg after 3 hrs of induction at 37˚C. Cell pellets were resuspended in 100 mL Nb purification buffer containing 25 mM HEPES pH 7.5 and 125 mM

NaCl. Nbs were then cleaved from the cell surface by overnight digestion with (tobacco etch virus) TEV protease at 4 ˚C under gentle stirring.

The TEV digested solution was centrifuged at 38,000 xg for 1 hr and the supernatant was loaded on Strep-Tactin resin pre-equilibrated with Nb purification buffer using gravity flow. Resin was washed with 10x column volume of purification buffer and eluted with 2.5 mM desthiobiotin. Eluted protein was concentrated to ~500 µL and further purified by size exclusion on an Akta fast protein liquid chromatography system using superdex 200 resin.

2. Nanobody selection

A culture of cells displaying the Nb library was grown in LB media supplemented with 50 µg/mL kanamycin at 37 ˚C and induced with 0.2% arabinose 0.2% when optical density reached ~0.5. After 3 hours of induction at 37 ˚C, library expressing cells were added to solution composed of P-gp storage buffer and containing 0.5 nM his-tagged P-gp, 1 nM anti-his Alexa Fluor-488 (Invitrogen). To account for cell permeability induced by detergent in the buffer, propidium iodide (PI) was added to a final concentration of 0.01%.

The solution containing P-gp and library expressing cells was allowed to incubate for 30 min at 4 ˚C and cells which bound to P-gp were isolated using a Bio-Rad S3e cell sorter. A population of *e.coli* was first identified by forward and side scattering, and cells within this population exhibiting fluorescence at 488 nm were collected in LB media. However, any cells displaying PI fluorescence (647 nm) were shunted into a waste container. In total, 4,060,973 events were sorted, with 15,676 sent to waste for PI incorporation and 1,145 collected. Collected cells were immediately plated on LB agar supplemented with 50 ug/mL kanamycin and incubated overnight at 37 ˚C.

3. Flow cytometric validation

Colonies from FACS collected events were picked and grown in 96-well blocks overnight at 37 °C in LB supplemented with 50 ug/mL kanamycin. Arabinose was then added to a final concentration of 0.2% (m/v) and induction proceeded for 3 hours at 37 °C. In a separate 96-well block, P-gp storage buffer containing 0.5 nM P-gp and 1 nM anti-his Alexa Fluor-488 (BioLegend) was added to each well. Concentrations of P-gp and antibody were kept at least 10-fold below concentrations at which non-specific binding to uninduced library cells was observed. Induced cells were then transferred to the block containing P-gp and analyzed on a Novocyte flow cytometer (Acea Biosciences) using the NovoExpress 1.2.5 software package. Cell populations with the highest fluorescence emission intensity at 530 nm were selected as candidates for kinetics analysis.

4. Kinetics analysis

Nb-A7 was purified and biotinylated using a 1:1 molar ratio of EZ-Link NHS-biotin (Thermo Fisher). Analysis was then carried out using an Octet K2 (Molecular Devices) at 30 °C. Streptavidin coated biosensors were hydrated in P-gp storage buffer and then transferred to wells containing 1 µg/mL Nb-A7. Immobilization was monitored and allowed to proceed until the BLI signal reached ~0.8 nM. Biosensors were then quenched with 10 µg/mL biocytin and washed in buffer for 1 min. Kinetics analysis was carried out by allowing biosensors to equilibrate in P-gp storage buffer for baseline measurements, transferring biosensors into wells containing P-gp or BSA to measure on rates, and transferring them back into the baseline wells to measure off rates. For each measurement, reference sensors without Nb immobilized were included to correct for analyte protein binding to the sensors.

5. Epitope mapping with HDX-MS

HDX-MS measurements were made using a Synapt G2Si system (Waters Corporation) as described previously (9). Deuterated buffer was prepared by lyophilizing 10 mL of 20 mM HEPES pH 7.5 and 100 mM NaCl. Lyophilized buffer was resuspended in 10 mL 99.96% D_2O immediately before use, to which was added powdered β-DDM to a final concentration of 0.01%. Sample containing 6 µM P-gp was analyzed after 0, 0.5, 1 and 5 mins of exchange at 25 °C to provide a measure of apo state dynamics. A separate sample containing 6 µM P-gp and 10 µM Nb-A7 was analyzed at the same time points to interrogate solvent protection due to Nb binding. Nb-A7 (10 µM) was added to D_2O buffer to maintain equilibrium following dilution into deuterated buffer. H_2O was added to deuterated buffer used for measurement of the apo state to normalize back-exchange and buffer dilution between the two states.

C. Results

1. Nanobody selection

E. coli cultures displaying our Nb library were incubated with 0.5 nM P-gp, and cells displaying Nb bound to P-gp were isolated using FACS (Fig. 5.2A). The sorting procedure was completed in one afternoon with 4,060,973 events sorted and 1,415 collected for further interrogation. Collected events were grown overnight on LB agar and the resulting colonies were picked to produce monoclonal populations of Nb-displaying cells. These monoclonal populations were then validated for P-gp binding with flow cytometry. Nb clone A7 (Nb-A7) was selected for further analysis (Fig. 5.2B).
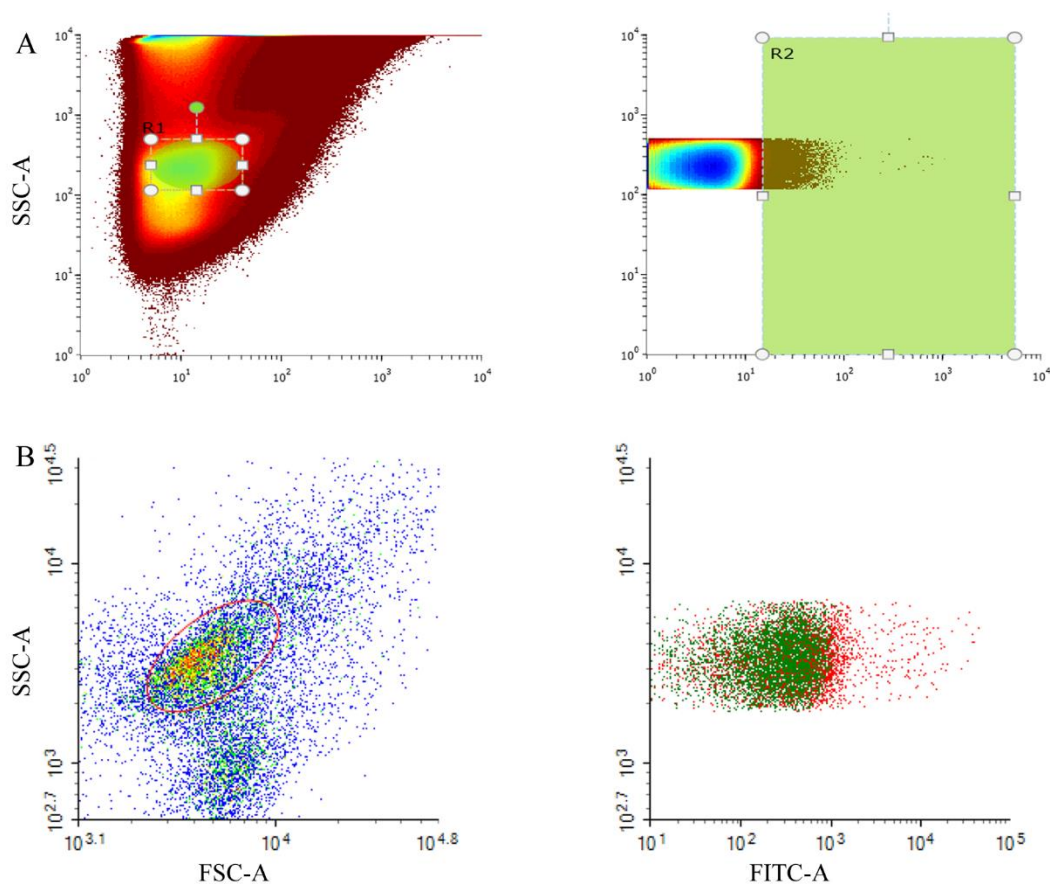
Figure 5.1. Cell sorting. (**A**) FACS plots of library-expressing cells in solution with 0.5 nM P-gp. Light scattering was used to identify a population of *e. coli* cells (left), and antigen binding was indicated by fluorescence emission intensity at 530 nM. (**B**) Monoclonal flow cytometry validation of Nb-A7.

2. Kinetics analysis

Nb-A7 was purified and further validated for P-gp binding using a ForteBio Octet K2. The Octet K2 detects interferometric signals occurring at the surface of sensors loaded with immobilized protein to quantify association and dissociation rates of biomolecular interactions (10). Screening of individual Nb clones can be completed within minutes, and thorough kinetics

analysis may be carried out within 1-2 hours. The device is thus ideal for rapid orthogonal

validation, high throughput screening and lead ranking (11).

Biotinylated Nb-A7 was immobilized on Octet sensors and screened for binding to 50

nM P-gp (Fig. 5.2A). Further testing confirmed no non-specific binding to 50 nM bovine serum

albumin (BSA). After confirming Nb-A7 as a valid P-gp binder, a dose-dependent kinetics assay

was carried out (Fig. 5.2B). Association and dissociation rates fit a 1:1 binding model with K_D =

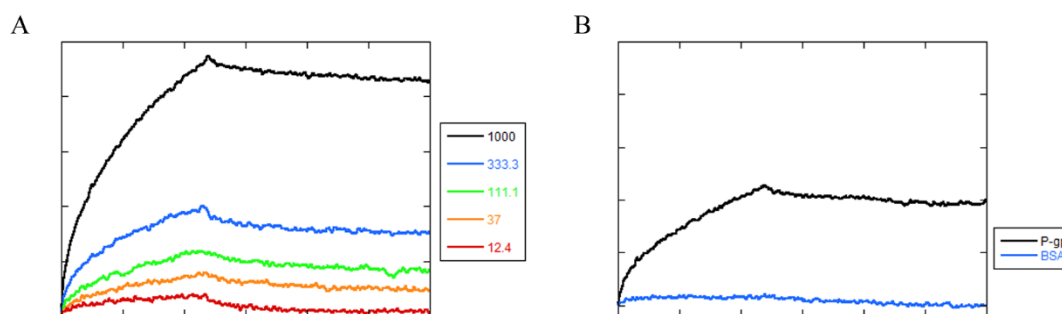28 ± 0.1 nM (Table 5.1).

Figure 5.2. Nanobody binding kinetics. (A) Following
orthogonal validation of antigen binding, affinity was
determined by measuring binding to 1000 (black), 333
(blue), 111 (green), 37 (orange), and 12 (red) nM P-gp.
(B) Nb-A7 was immobilized and screened for binding
against 50 nM P-gp (black) and 50 nM BSA (blue).

Table 5.1. Nb-A7 and P-gp binding kinetics.

K_D (nM)	k_{on} (1/Ms)	k_{off} (1/s)	R^2
28 ± 0.1	3.9 ± 0.1 E04	1.0 ± 0.05 E-03	0.97

3. Epitope mapping

Hydrogen deuterium exchange mass spectrometry (HDX-MS) was used to determine the binding interface between Nb-A7 and P-gp. This technique is convenient for epitope mapping, provided the binding interaction being studied is expansive enough to occlude peptide amides and persistent enough to occlude solvent over timescales relevant to deuterium exchange (12-14).

Our experimentally determined affinity of 28 nM was deemed sufficient for HDX-MS and measurements were carried out on both the apo state of P-gp, and on P-gp in complex with Nb-A7. We obtained 79.8% P-gp sequence coverage in 79 different peptides, and differences between states greater than 1 Da were interpreted as significant. When comparing the two measured states, only 4 regions of P-gp appeared to decrease in exchange by more than 1 Da (Fig. 5.3). These regions corresponded to residues 6-25 along the N-terminus, residues 121-144 on transmembrane helix 2 (TM2), residues 339-350, 340-350 on TM6 and residues 916-937, 918-940 on TM11. Overlaying the difference in relative uptake between the two experimental states revealed that all 4 of these regions are in spatial proximity.
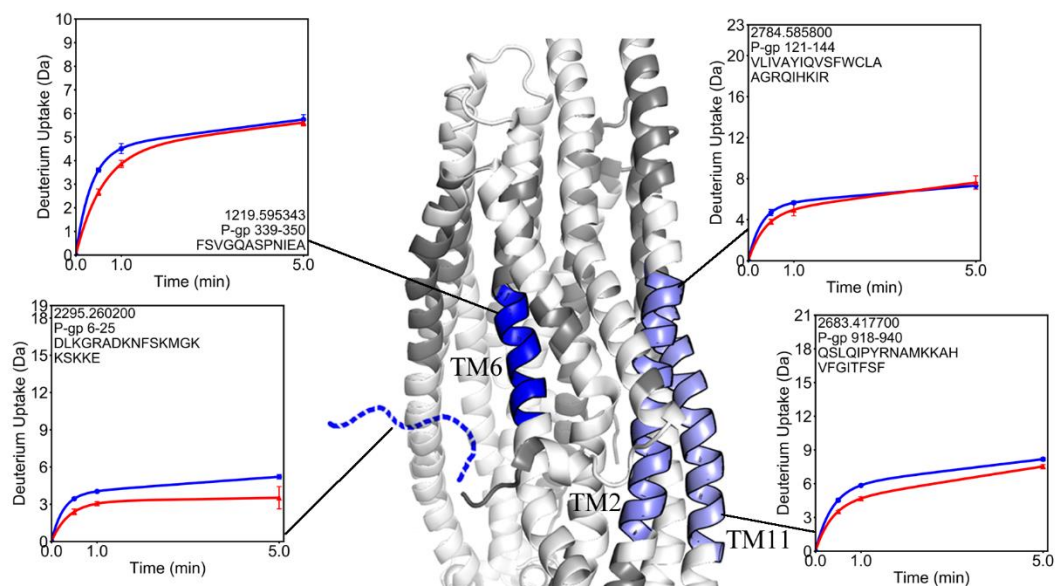
Figure 5.3. Nanobody epitope mapping. P-gp structure is colored by the difference in relative exchange between apo P-gp (blue) and P-gp bound to Nb-A7 (red). Regions not covered are colored grey, and regions with uptake difference less than 1 Da are colored white. The unstructured N-terminus is shown as a dotted line.

D. Discussion

Our rapid *in vitro* system facilitated discovery of P-gp binding Nb within a matter of days. Further, the affinity of Nb-A7 obtained directly from our naïve library (K_D: 28 nM) was similar to affinities reported Nbs obtained from animal immunization (K_D: 7 nM) (15). Our measured affinity also explains the relatively minor population shift observed during flow cytometry analysis (Fig. 5.1). Due to experimental constraints, flow cytometry analysis was carried out using 0.5 nM P-gp. Only a fraction of the monoclonal population was observed bound to P-gp as this concentration fell below the measured K_D for this interaction.

As Nb interactions consist of small binding epitopes mediated primarily by side-chain interactions (16), we were unsurprised by relatively small reductions in uptake (1-2 Da) in the

Nb-A7-bound state following HDX-MS. Interestingly, the 4 regions with reduced deuterium uptake in the presence of Nb-A7 are located along the outer sides of the transporter molecule (Fig. 5.3). This behavior indicates that binding to one side of the TM region slows nearby dynamic processes through allostery, although which side Nb-A7 bound to cannot be inferred from this dataset. Ongoing structural determination efforts will further assist in the characterization of this interaction.

Nb-A7 demonstrates the utility of our platform. After a single FACS selection we obtained Nb specific for the antigen P-gp with low nM binding affinity suitable for epitope mapping using HDX-MS. Our *in vitro* platform allows for selection against toxic antigen targets that are difficult to obtain through conventional *in vivo*, and the selection process is limited only by the replication speed of *e. coli*. Nbs selected in this way can be readily produced by overexpression in prokaryotic systems and may be used for facilitating structure determination (17), interrogating conformational dynamics (18), targeted therapeutics (19), or any other application requiring specific molecular probes.

Chapter V, in full, is material in preparation for journal submission to which the dissertation author was the principle researcher and author. The material will be submitted for publication. (**Kopcho, N.**, Lee, C.W., Chang, G. (2020).)

E. References

1.   Anonymous (2019) Global antibody market growth 2019-2024. pp 1-164.

2.   Thurber GM, Schmidt MM, & Wittrup KD (2008) Antibody tumor penetration: transport opposed by systemic and antigen-mediated clearance. *Adv. Drug Deliv. Rev.* 60:1421-1434.

3.   Werner RG (2004) Economic aspects of commercial manufacture of biopharmaceuticals. *J. Biotechnol.* 113:171-182.

4.   Wang W, Singh S, Zeng DL, King K, & Nema S (2007) Antibody structure, instability, and formulation. *J. Pharm. Sci.* 96:1-26.

5.   Ahmad ZA, Yeap SK, Ali AM, Ho WY, Alitheen NBM, & Hamid M (2012) scFv antibody: principles and clinical application. *Clin. Dev. Immunol.*:1-15.

6.   Muyldermans S, Baral TN, Retamozzo VC, De Baetselier P, De Genst E, Kinne J, Leonhardt H, Magez S, Nguyen VK, Revets H, Rothbauer U, Stiljemans B, Tillib S, Wernery U, Wyns L, Hassanzadeh-Ghassabeh G, & Saerens D (2009) Camelid immunoglobulins and nanobody technology. *Vet. Immunol. Immunopathol.* 128:178-183.

7.   Buelens K, Hassanzadeh-Ghassabeh G, Muyldermans S, Gils A, & Declerck PJ (2010) Generation and characterization of inhibitory nanobodies towards thrombin activatable fibrinolysis inhibitor. *J. Thromb. Haemost.* 8:1302-1312.

8.   Ardekani LS, Gargari SLM, Rasooli I, Bazl MR, Mohammadi M, Ebrahimizadeh W, Bakherad H, & Zare H (2013) A novel nanobody against urease activity of helicobacter pylori. *Int. J. Infect. Dis.* 17:e723-e728.

9.   Kopcho NJ, Chang G, & Komives EA (2019) Dynamics of ABC transporter P-glycoprotein in three conformational states. *Sci. Rep.* 9:10592.

10.   Kamat V & Rafique A (2017) Designing binding kinetic assay on the bio-layer interferometry (BLI) biosensor to characterize antibody-antigen interactions. *Anal. Biochem.* 536:16-31.

11.   Lad L, Clancy S, Kovalenko M, Liu C, Hui T, Smith V, & Pagratis N (2015) High-Throughput Kinetic Screening of Hybridomas to Identify High-Affinity Antibodies Using Bio-Layer Interferometry. *J. Biomol. Screen.* 20:498-507.

12.   Baerga-Ortiz A, Hughes CA, Mandell JG, & Komives EA (2002) Epitope mapping of a monoclonal antibody against human thrombin by H/D-exchange mass spectrometry reveals selection of a diverse sequence in a highly conserved protein. *Protein Sci.* 11:1300-1308.

13. Zhang Q, Willison LN, Tripathi P, Sathe SK, Roux KH, Emmett MR, Blakney GT, Zhang HM, & Marshall AG (2011) Epitope mapping of a 95 kDa antigen in complex with antibody by solution-phase amide backbone hydrogen/deuterium exchange monitored by fourier transform ion cyclotron resonance mass spectrometry. *Anal. Chem.* 83:7129-7136.

14. Zhu S, Liuni P, Ettorre L, Chen T, Szeto J, Carpick B, James DA, & Wilson DJ (2019) Hydrogen−deuterium exchange epitope mapping reveals distinct neutralizing mechanisms for two monoclonal antibodies against diphtheria toxin. *Biochemistry* 58:646-656.

15. Koromyslova AD & Hansman GS (2015) Nanobody binding to a conserved epitope promotes norovirus particle disassembly. *J. Virol.* 89:2718-2730.

16. Kumar H, Finer-Moore JS, Jiang X, Smirnova I, Kasho V, Pardon E, Steyaert J, Kaback HR, & Stroud RM (2018) Crystal structure of a ligand-boundLacY–nanobody complex. *PNAS* 115:8769-8774.

17. Low C, Yau YH, Pardon E, Jegerschold C, Wahlin L, Quistgaard EM, Moberg P, Geifman-Shochat S, Steyaert J, & Nordlund P (2013) Nanobody mediated crystallization of an archeal mechanosensitive Channel. *PLoS One* 8:e77984.

18. Dmitriev OY, Lutsenko S, & Muyldermans S (2016) Nanobodies as probes for protein dynamics in vitro and in cells. *J. Biol. chem.* 8:3767-3775.

19. Chowdhury HG, Tong Z, Mathavan I, Li M, Itawa S, Zirah S, Rebuffat S, Van Veen HW, & Beis K (2014) Structure of an antibacterial peptide ATP-binding cassette transporter in a novel outward occluded state. *PNAS* 111:9145-9150.